ATLAS NOTE

ATLAS-CONF-2015-018

19th May 2015

Constraints on promptly decaying supersymmetric particles with lepton-number- and *R*-parity-violating interactions using Run-1 ATLAS data

The ATLAS Collaboration

Abstract

In this document, a selection of ATLAS searches for supersymmetry (SUSY), mostly optimised for *R*-parity-conserving SUSY, are reinterpreted in new *R*-parity-violating SUSY models where an unstable neutralino decays promptly to leptons and/or jets. All forms of renormalisable *R*-parity-violating interactions with lepton-number violation are considered. The production of squarks and gluinos is constrained for different neutralino masses and decay modes. In most cases lower limits on the squark and gluino masses of $m \gtrsim 1$ TeV are obtained; exceptions to this rule are located and discussed. Additionally, bilinear *R*-parity violation is considered in a model with a natural SUSY spectrum with light third-generation squarks and higgsinos. Only a small portion of the explored parameter space remains unexcluded, where $m_{\tilde{q}_{\mathrm{L},3}} > 810$ GeV.

ATLAS-CONF-2015-018
20 May 2015

1. Introduction

The search for new particles and phenomena not described by the Standard Model of particle physics (SM) is one of the primary objectives of the ATLAS experiment [1]. Weak-scale supersymmetry (SUSY) is a well-motivated and well-studied example of a model used to guide many of these searches [2–10]. In this document, new constraints are set on SUSY models in the presence of lepton-number violating interactions ($\not{L}$) that are present in generic SUSY models with minimal particle content. These interactions, together with similar baryon-number-violating interactions ($\not{B}$), are described by the following superpotential terms:

$$W_{\not{L}\mathrm{RPV}} = \frac{1}{2}\lambda_{ijk} L_i L_j \bar{E}_k + \lambda'_{ijk} L_i Q_j \bar{D}_k + \epsilon_i L_i H_2, \tag{1a}$$

$$W_{\not{B}\mathrm{RPV}} = \frac{1}{2}\lambda''_{ijk} \bar{U}_i \bar{D}_j \bar{D}_k. \tag{1b}$$

In this notation, L_i and Q_i indicate the lepton and quark SU(2)-doublet superfields, respectively, while $\bar{E}_i$, $\bar{U}_i$ and $\bar{D}_i$ are the corresponding singlet superfields. The indices i, j and k refer to quark and lepton generations. The Higgs SU(2)-doublet superfield H_2 contains the Higgs field that couples to up-type quarks. The λ_{ijk}, λ'_{ijk} and λ''_{ijk} parameters are new Yukawa couplings, while the ϵ_i parameters have dimensions of mass. The terms in Eq. (1) are forbidden in many models of SUSY by the imposition of R-parity conservation in order to prevent rapid proton decay [11–15]. However, proton decay can also be prevented by suppressing only one of $W_{\not{L}\mathrm{RPV}}$ or $W_{\not{B}\mathrm{RPV}}$, in which case some R-parity-violating (RPV) interactions remain in the theory.

Introducing non-zero RPV couplings into supersymmetric models can significantly weaken mass and cross-section limits from collider experiments and also provide a rich phenomenology, see e.g. Refs. [16–20]. Most relevant is the fact that the lightest supersymmetric particle (the LSP) is unstable and decays to SM particles via the interactions in Eq. (1), rather than escaping unseen as predicted by models that conserve R-parity. The LSP lifetime, τ_{LSP}, is not predicted in general; we focus on prompt decays of a neutralino LSP, meaning that the decay distance is not resolved from the point of production by the considered ATLAS searches. The upper limit of what may be regarded as prompt is analysis-dependent, but as a general guideline, channels requiring the explicit reconstruction of a lepton require $\tau_{\mathrm{LSP}} \lesssim O(1\,\mathrm{ps})$ to satisfy typical requirements on the lepton's impact parameter, while channels with a lepton veto have sensitivity up to lifetimes of approximately 1 ns [21]. A systematic phenomenological overview of possible signatures specific to a particular RPV scenario is given in Ref. [20], which goes through all possible mass orderings and the dominant decay signatures.

Existing searches for supersymmetry with $\not{L}$ RPV are reviewed in Sect. 1.1. These include constraints on decays via the first ($LL\bar{E}$) operator in Eq. (1a), but only in the case where a single RPV coupling is dominant, which limits the possible event signatures. In spite of the rich phenomenology, prompt decays via the second ($LQ\bar{D}$) term of Eq. (1a) have so far been considered by ATLAS only for the specific case of a top-squark LSP [22]. Limits have previously been set on decays via the third, bilinear, term of Eq. (1a), but only in the case of the highly constrained mSUGRA model. In this note, the scope of constraints set by ATLAS on lepton-number-violating SUSY decays is expanded by considering nearly all possible decay patterns of a neutralino LSP allowed by Eq. (1a). The baryon-number-violating interactions of Eq. (1b) are not considered, as they have already been well-addressed by ATLAS searches [23], and are strongly constrained if lepton-number-violating interactions are also allowed.

A total of four models are considered in this note. Three are simplified models, and allow the neutralino LSP to decay via the $LL\bar{E}$ or $LQ\bar{D}$ operators. We focus on the production of squarks and gluinos, which will be produced more abundantly at the LHC than other SUSY particles if they are not too massive. The new results obtained here can inform search strategies for Run-2 and indicate where specific optimisations may be required. In addition, the existing ATLAS constraints on gluino production with $LL\bar{E}$-mediated LSP decays are strengthened by including results from other searches that did not previously consider this scenario. In the case of bilinear R-parity-violation (bRPV), the connection between the bRPV couplings and neutrino masses is used to require that all model parameters are consistent with neutrino data [24]. Generic squark and gluino production is already highly constrained in this case (see Sect. 1.1), therefore a natural SUSY model is considered, with light top squarks and higgsino-like neutralino LSPs, within the framework of the phenomenological minimal supersymmetric Standard Model (pMSSM) [25].

The searches used to constrain these models all use 20.3 fb^{-1} of pp collision data with $\sqrt{s} = 8$ TeV collected in 2012. Many of the searches used were optimised for R-parity-conserving (RPC) SUSY models but nevertheless can tightly constrain RPV scenarios. A short overview of which analyses are used to constrain which models is given in Sect. 2, after the current constraints on RPV SUSY production at the LHC are reviewed. The models are described in more detail in the following sections, together with the exclusion limits obtained from the ATLAS data. The $LL\bar{E}$ and $LQ\bar{D}$ models are covered in Sect. 3, while Sect. 4 concerns the bRPV model. Finally, the conclusions are presented in Sect. 5.

1.1. Existing constraints on L-violating RPV SUSY

In this section, constraints on SUSY production with RPV decays by the ATLAS [1] and CMS [26] collaborations are described, focusing on the lepton-number-violating interactions of Eq. (1a).

The ATLAS search for events with four or more charged leptons [27] has constrained models with $LL\bar{E}$ couplings. Strong constraints were placed when the λ_{121} or λ_{122} terms dominate, while less stringent limits were found for tau-rich events produced by the λ_{133} or λ_{233} terms. Additionally, a search for non-prompt signatures included channels with displaced charged lepton pairs, probing smaller values of λ_{121} and λ_{122} couplings [28]. Multi-lepton searches for $LL\bar{E}$-type scenarios have also been performed by CMS [29, 30], including extensions into non-prompt decays [31]. Stop pair production was probed by CMS using multi-lepton events with jets tagged as originating from b-quark decays (b-jets), constraining signatures based on λ_{122} and λ_{233} decays [32] and also λ_{123}-related models [33]. Searches for $LL\bar{E}$-related signatures were also performed at the Tevatron's D0 and CDF experiments [34, 35] and by the LEP collaborations [36, 37].

Searching for effects from $LQ\bar{D}$ couplings, ATLAS has placed constraints on non-prompt decays leading to a multi-track displaced vertex [28]. A search for $\tilde{t}_1\tilde{t}_1 \to b\ell b\ell$ events also constrained prompt decays of the top squark via $LQ\bar{D}$ couplings [22]. A similar model with non-prompt decays was investigated by CMS [38]. The CMS search for events with multiple leptons and b-jets [32] has been interpreted to constrain decays mediated by λ'_{233} while Ref. [33] also examined λ'_{231} decays. Furthermore the search in Ref. [39] constrained models with non-zero λ'_{333} and λ'_{3jk} (with $j,k = 1,2$), investigating signatures from τ-leptons and b-jets.

Assuming a bRPV extension of the mSUGRA model, limits on the underlying mSUGRA mass parameters m_0 and $m_{1/2}$ were obtained in several ATLAS analyses. The most sensitive channels required jets in addition to one or more charged leptons, where the charged leptons may be electrons and muons [40, 41], or hadronically decaying taus [42].

Distinct signatures from resonant sparticle production with subsequent decay are possible for a combination of non-zero $LQ\bar{D}$ and $LL\bar{E}$ couplings. The ATLAS collaboration performed a dedicated search [43] for a heavy narrow resonance decaying to $e\mu$, $e\tau$, or $\mu\tau$ assuming non-zero λ'_{311} in combination with non-zero λ_{132}, λ_{133}, or λ_{233}, respectively. The $e\mu$ case was also considered by CMS [44], and both searches significantly improve previous constraints from CDF [45] and D0 [46]. Using the search channel for same-sign muons and at least two jets as motivated by resonant smuon production, the CMS collaboration obtained limits on the coupling λ'_{211} in the mSUGRA framework [47].

2. Overview of reinterpreted analyses

This section summarises the most relevant aspects of the different analyses used for constraining the R-parity violating models considered in this note. Since all the selection criteria used have been defined in detail in the original analysis papers, only the most relevant selections are outlined in what follows. The analyses make use of three types of event selection:

Signal regions (SRs) are used to search for signs of a SUSY signal.

Control regions (CRs) are used to determine the rate of SM background processes in the SRs.

Validation regions (VRs) are used to check the predictions made using the CRs.

When each analysis was designed, it was checked that the CRs and VRs were free of SUSY signal events, for the particular models under consideration at the time. This may not be true when new models are considered, so the CR and VR contamination must be checked anew. Increased contamination has different potential consequences, depending on where it occurs. VR contamination will not directly affect a reinterpretation of a search, but it potentially invalidates the original SM background prediction, and should therefore be no larger than the associated uncertainty. As the CRs are used to estimate the rate of SM processes, the estimated SR background will change if a significant fraction of CR events can be attributed to signal. For this reason, the contribution of signal is accounted for in each CR and the SM background recalculated when setting new limits. Relevant CRs and VRs are also listed in the analysis descriptions below.

It has been found that many of the considered searches are sensitive to more than one model, and that most models can be constrained by more than one search. To help guide the reader, Table 1 briefly summarises which analyses are used to constrain which RPV SUSY models. The precise descriptions of the models considered, and specific details of the associated CR and VR contamination, can be found in Sects. 3 and 4.

In the earlier descriptions of the analyses that are considered herein, the term "lepton" has several different meanings depending on the nature of the paper. Here and in the following, it refers to any charged or neutral lepton of any generation. The corresponding definitions of charged or neutral leptons also refer to leptons of any generation. The term "light lepton" is used to indicate only electrons and muons.

2.1. Four-lepton analysis

The four-lepton (4L) analysis [27] was designed to be sensitive to SUSY models with non-zero $LL\bar{E}$ RPV couplings, as well as RPC SUSY models that predict events with high numbers of charged leptons in the

		Simplified models			pMSSM
		$LL\bar{E}$	$LQ\bar{D}$	$LQ\bar{D}$	bRPV
		$\tilde{g}\tilde{g}$	$\tilde{g}\tilde{g}$	$\tilde{q}\tilde{q}$	
Short name	Ref.	$4q, 4\ell, 2\nu$	$8q, 2(\ell/\nu)$	$6q, 2(\ell/\nu)$	
4L	[27]	✓			
SS/3L	[40]	✓	◊		✓
1L	[41]		✓	✓	◊
0L 2–6 jets	[48]		✓	✓	
0L 7–10 jets	[49]		✓		

Table 1: Overview of analyses used to constrain the RPV models in this note. The signature descriptions are indicative only, and the reader is referred to the analysis documentation for further details in each case. Filled cells indicate where limits have been obtained by a particular analysis for a particular model. In cells with a lozenge (◊), the resulting limits are surpassed by other channels and there is no contribution to the final results from that analysis. For the simplified models, an indication is given of the nominal event signature, where q, ℓ and ν refer to quarks, charged leptons and neutrinos, respectively, of any generation.

SR name	$N(e/\mu)$	$N(\tau)$	$E_{\mathrm{T}}^{\mathrm{miss}}$ [GeV]	or	m_{eff} [GeV]
SR0noZb	≥ 4	≥ 0	≥ 75	or	≥ 600
SR1noZb	$= 3$	≥ 1	≥ 100	or	≥ 400
SR2noZb	$= 2$	≥ 2	≥ 100	or	≥ 600

Table 2: Definitions of the most relevant signal regions from the 4L analysis [27].

final-state. It requires at least four charged leptons in every signal event, at least two of which must be light leptons. The events are separated into signal regions based on the number of light leptons observed, and the presence or absence of a Z boson candidate among the pairs of light leptons. Final suppression of the SM background is made using the missing transverse momentum (the magnitude of which is denoted $E_{\mathrm{T}}^{\mathrm{miss}}$) and the effective mass (m_{eff}), defined in this case as the scalar sum of the $E_{\mathrm{T}}^{\mathrm{miss}}$, the p_{T} of all selected charged leptons and the p_{T} of reconstructed jets with $p_{\mathrm{T}} > 40$ GeV.[1] No explicit requirement is made on reconstructed jets, ensuring that the search is sensitive to both strong and electroweak SUSY production processes.

Of the nine SRs used in the 4L analysis, only the three described in Table 2 are relevant to this note. In all cases, events with a pair of light leptons forming a Z boson candidate are vetoed, and possible $Z \to \ell^+\ell^-\gamma$ and $Z \to \ell^+\ell^-\ell^+\ell^-$ candidates are also rejected. Additionally, either high $E_{\mathrm{T}}^{\mathrm{miss}}$ or high m_{eff} is required – thus, a selected event may have one quantity below the threshold, but never both. The resulting SM background is very low, between about 1.4 and 3 events for the SRs considered here. As the three SRs used here have mutually exclusive selection criteria, they are statistically combined when setting constraints on the specific SUSY models.

In the 4L analysis, CRs are used to estimate the background contribution from non-prompt and fake

[1] ATLAS uses a right-handed coordinate system with its origin at the nominal interaction point (IP) in the centre of the detector and the z-axis along the beam pipe. The x-axis points from the IP to the centre of the LHC ring, and the y-axis points upward. Cylindrical coordinates (r, ϕ) are used in the transverse plane, ϕ being the azimuthal angle around the beam pipe. The pseudorapidity is defined in terms of the polar angle θ as $\eta = -\ln\tan(\theta/2)$. The transverse momentum of a particle is denoted $p_{\mathrm{T}} = \sqrt{p_x^2 + p_y^2}$.

SR	Leptons	$N_{b-\text{jets}}$	Other variables	m_{eff}
SR3b	SS or 3L	≥ 3	$N_{\text{jets}} \geq 5$	$m_{\text{eff}} > 350$ GeV
SR1b	SS	≥ 1	$N_{\text{jets}} \geq 3$, $E_{\text{T}}^{\text{miss}} > 150$ GeV, $m_{\text{T}} > 100$ GeV, SR3b veto	$m_{\text{eff}} > 700$ GeV
SR3Lhigh	3L	-	$N_{\text{jets}} \geq 4$, $E_{\text{T}}^{\text{miss}} > 150$ GeV, SR3b veto	$m_{\text{eff}} > 400$ GeV

Table 3: Definitions of the most relevant signal regions from the SS/3L analysis [40].

leptons. They have the same kinematic requirements as the corresponding signal regions, but one or two of the four charged leptons must fail the standard isolation or other identification criteria normally used. Also, VRs are used to check the background estimates. In events with a Z boson veto, the VR events must satisfy $E_{\text{T}}^{\text{miss}} < 50$ GeV and $m_{\text{eff}} < 400$ GeV. The possible contamination of these control and validation regions by the $LL\bar{E}$ model considered in this note was already investigated in Ref. [27], and found to be negligible.

2.2. SS/3L analysis

The SS/3L search [40] requires two light leptons with the same electric charge or three light leptons in conjunction with requirements on the number of jets. It is aimed at SUSY models where pair-produced Majorana particles (e.g. gluinos) can decay semileptonically with a large branching ratio. The effective mass, m_{eff}, is a key discriminating variable, defined in the SS/3L analysis as the sum of $E_{\text{T}}^{\text{miss}}$ and the p_{T} values of the leptons and jets (with $p_{\text{T}} > 40$ GeV). The two leading light leptons have to fulfil $p_{\text{T}} > 20$ GeV and $p_{\text{T}} > 15$ GeV, respectively. If the lepton contains a third light lepton with $p_{\text{T}} > 15$ GeV the event is regarded as three-lepton event, otherwise it is a two-lepton event.

Five different signal regions are defined, where all details are described in the corresponding paper. The most relevant SRs for the results in this analysis are summarised in Table 3. SR3b and SR1b use leptons, the presence of b-jets and large m_{eff} to suppress the SM background. There is no explicit $E_{\text{T}}^{\text{miss}}$ requirement in SR3b, which means it does not depend on the assumption of a stable LSP escaping the detector unseen. SR1b additionally uses the transverse mass, m_{T}, to reject background events with W bosons, defined as

$$m_{\text{T}} = \sqrt{2p_{\text{T}}^{\ell} E_{\text{T}}^{\text{miss}} (1 - \cos[\Delta\phi(\vec{\ell}, \mathbf{p}_{\text{T}}^{\text{miss}})])}, \tag{2}$$

where p_{T}^{ℓ} is the larger of the p_{T} values of the two charged leptons, and $\mathbf{p}_{\text{T}}^{\text{miss}}$ is the missing transverse momentum vector. The SR3Lhigh selection requires a third light lepton for additional background rejection, in addition to requiring at least four high-p_{T} jets. All SRs for the SS/3L search have been designed to be statistically independent, and are combined to improve the overall sensitivity.

Several VRs are used to check the quality of the background estimates used in the SS/3L search. Of particular interest are those regions dedicated to rare processes, which have a relatively low number of events and are potentially susceptible to contamination from a SUSY signal. Events with same-sign muons and two b-jets are used to check the $t\bar{t}W$ background, while events with three light leptons (including a Z candidate) and at least one b-jet are used to validate the $t\bar{t}Z$ background component. Finally, events with same-sign muons and no b-jets are used to check the WZ background.

	3-jet	5-jet	6-jet
N_{lep}	= 1	= 1	= 1
$p_{\text{T}}^{\text{lep1}}$ [GeV]	> 25	> 25	> 25
$p_{\text{T}}^{\text{lep2}}$ [GeV]	< 10	< 10	< 10
N_{jet}	≥ 3	≥ 5	≥ 6
$p_{\text{T}}^{\text{jet}}$ [GeV]	> 80, 80, 30 p_{T} 5th jet < 40 GeV	> 80, 50, 40, 40 ,40 p_{T} 6th jet < 40 GeV	> 80, 50, 40, 40, 40 ,40
$E_{\text{T}}^{\text{miss}}$ [GeV]	> 300	> 300	> 250
m_{T} [GeV]	> 150	> 150	> 150
$E_{\text{T}}^{\text{miss}}/m_{\text{eff}}^{\text{excl}}$	> 0.3	–	–
$m_{\text{eff}}^{\text{incl}}$ [GeV]	> 800	> 800	> 600
shape fit variable	$m_{\text{eff}}^{\text{incl}}$	$m_{\text{eff}}^{\text{incl}}$	$E_{\text{T}}^{\text{miss}}$
binning: bin size	4 bins: 200 GeV	4 bins: 200 GeV	3 bins: 100 GeV

Table 4: Definitions of the most relevant signal regions from the 1L analysis [41].

2.3. Strong production with leptons analysis

The analysis in Ref. [41] is designed to be sensitive to a wide variety of SUSY models where light leptons may be produced, for example via $W \to \ell\nu$ decays. It considers a variety of selections, requiring one or two light leptons with opposite charge. In the context of the models considered in this note, only the regions requiring one high-p_{T} (> 25 GeV) lepton are considered, and for this reason it is referred to here as the 1L analysis. A summary of the SR selection criteria can be found in Table 4. The transverse mass m_{T} is defined using Eq. (2) applied to the lepton to reject events containing a W boson. The inclusive effective mass ($m_{\text{eff}}^{\text{incl}}$) is the scalar sum of the p_{T} of the lepton, the jets (with $p_{\text{T}} > 25$ GeV) and the $E_{\text{T}}^{\text{miss}}$:

$$m_{\text{eff}}^{\text{incl}} = p_{\text{T}}^{\ell} + \sum_{j=1}^{N_{\text{jet}}} p_{\text{T}}^{\text{jet}\,j} + E_{\text{T}}^{\text{miss}}. \tag{3}$$

Furthermore the ratio $E_{\text{T}}^{\text{miss}}/m_{\text{eff}}^{\text{excl}}$ is computed, where the exclusive effective mass, $m_{\text{eff}}^{\text{excl}}$, is defined in a similar way to $m_{\text{eff}}^{\text{incl}}$ but using only the three leading jets. The SRs are each binned in one variable and are statistically independent. They are statistically combined to give improved sensitivity when excluding a particular SUSY model.

Control regions are used in the 1L analysis to constrain the dominant background processes, such as $t\bar{t}$, using events with lower values of $E_{\text{T}}^{\text{miss}}$ and m_{T}. In order to test the extrapolation from the CRs to the SRs, which is based on simulated events, two validation regions are also defined for each signal region. One VR extends to high $E_{\text{T}}^{\text{miss}}$, while the other reaches towards higher m_{T}, starting from the $t\bar{t}$ and W+jets control regions. The same m_{eff} selections as in the SRs are applied in every case.

2.4. Zero-lepton, 7–10 jets analysis

The 0L 7–10 jets analysis [49] was designed to be sensitive to SUSY events with high jet multiplicities and no isolated light leptons. Compared to many SUSY searches, only a relatively loose requirement is

	j50			j80	
	8j50	**9j50**	**≥ 10j50**	**7j80**	**≥ 8j80**
Jet $\|\eta\|$	< 2.0			< 2.0	
Jet p_{T}	> 50 GeV			> 80 GeV	
N_{jet}	$= 8$	$= 9$	≥ 10	$= 7$	≥ 8
b-jets	$0, 1, \geq 2$	$0, 1, \geq 2$	—	$0, 1, \geq 2$	$0, 1, \geq 2$
$E_{\mathrm{T}}^{\mathrm{miss}}/\sqrt{H_{\mathrm{T}}}$	≥ 4 GeV$^{1/2}$			≥ 4 GeV$^{1/2}$	

Table 5: Definitions of the 13 signal regions of the multi-jet + flavour stream of the 0L 7–10 jet analysis [49]. The signal regions are separated into two groups, labeled j50 and j80. Signal regions within each group are statistically combined, and the most sensitive SR group is used to set model-dependent limits.

Requirement	**5j**	**6jl**	**6jm**	**6jt+**
$N_{\mathrm{jet}} \geq$	5	6	6	6
$E_{\mathrm{T}}^{\mathrm{miss}}/m_{\mathrm{eff}}(N_{\mathrm{jet}}) >$	0.2	0.2	0.2	0.15
m_{eff}(incl.) [GeV] $>$	1200	900	1200	1700

Table 6: Final kinematic selections for the most relevant signal regions from the 0L 2–6 jets analysis [48]. Selection criteria common to these four signal regions are described in the text.

made on the $E_{\mathrm{T}}^{\mathrm{miss}}$. Example SUSY models targeted by this analysis include gluino pair production where each gluino decays to $t\bar{t}\tilde{\chi}_1^0$, and RPV SUSY with decays via the baryon-number-violating operator in Eq. (1b).

The signal regions of this analysis are split into two streams, denoted "multi-jet + flavour" and "multi-jet + M_J^{Σ}". The multi-jet + M_J^{Σ} stream makes use of large-radius ($R = 1$) jets reclustered from smaller $R = 0.4$ anti-k_t jets. It is not used in this note because preliminary studies indicated that the multi-jet + flavour stream is expected to be at least as powerful in all of the models considered. The signal regions of the multi-jet + flavour stream are listed in Table 5. There are two groups of disjoint selections, which differ in the minimum jet p_{T} requirement, either $p_{\mathrm{T}} > 50$ or 80 GeV. To constrain a specific model, all SRs within each group are statistically combined, and the group with the best expected limit is used.

As with the other analyses, control regions are used to estimate the main background sources. In particular, events with five or six jets are used to estimate the multi-jet background by extrapolating from low to high values of $E_{\mathrm{T}}^{\mathrm{miss}}/\sqrt{H_{\mathrm{T}}}$, where H_{T} is the scalar sum of the p_{T} of all jets with $p_{\mathrm{T}} > 40$ GeV and $|\eta| < 2.8$. Validation regions with one isolated light lepton are also defined to check the accuracy of the background estimates for $t\bar{t}$, W+jets and Z+jets events.

2.5. Zero-lepton, 2–6 jets analysis

The last analysis used in this note is a generic search for squark and gluino production in events with large $E_{\mathrm{T}}^{\mathrm{miss}}$, no isolated electrons or muons and at least 2–6 jets [48]. It is designed primarily to be sensitive to the RPC decays of squarks and gluinos, in cases where isolated light leptons are not produced, e.g. $\tilde{g}\tilde{g} \to q\bar{q}q\bar{q}\tilde{\chi}_1^0\tilde{\chi}_1^0$. A total of fifteen signal regions are defined, which vary in the minimum jet multiplicity requirement and other kinematic criteria. Of these SRs, only four are relevant for the signals considered here. These four all require at least five jets with $p_{\mathrm{T}} > 60$ GeV (all but one require at least six jets), and

at least one jet with $p_{\mathrm{T}} > 130$ GeV. Additionally, the magnitude of the missing transverse momentum must be greater than 160 GeV, and it must not be aligned in the transverse plane with any jet that has $p_{\mathrm{T}} > 40$ GeV to reduce the effect of mismeasured jet momenta. Further selections applied to individual SRs are listed in Table 6, which include two variations on the effective mass:

$$m_{\mathrm{eff}}(N_{\mathrm{jet}}) = E_{\mathrm{T}}^{\mathrm{miss}} + \sum_{j=1}^{N_{\mathrm{jet}}} p_{\mathrm{T}\ j}^{\mathrm{jet}}, \tag{4}$$

$$\text{and } m_{\mathrm{eff}}(\mathrm{incl.}) = E_{\mathrm{T}}^{\mathrm{miss}} + \sum_{p_{\mathrm{T}}>40\ \mathrm{GeV}} p_{\mathrm{T}}^{\mathrm{jet}}, \tag{5}$$

where N_{jet} refers to the number of jets required by the region, i.e. in this case five or six. The SRs are not statistically independent, and so constraints on any given SUSY model are obtained only with the region that has the best expected sensitivity.

For each SR, four control regions are used to estimate the contributions from different SM background processes. The multi-jet contribution is estimated using events where the $E_{\mathrm{T}}^{\mathrm{miss}}$ vector is aligned with one of the jets, and also the $E_{\mathrm{T}}^{\mathrm{miss}}/m_{\mathrm{eff}}(N_{\mathrm{jet}})$ selection is inverted (the control region with this selection is called CRQ in Ref. [48]). The contributions of events with W and $t\bar{t}$ production are estimated in events with one isolated light lepton and a b-jet veto or tag, respectively (CRW and CRT). Finally, $Z(\rightarrow \nu\nu)$+jets events are estimated using events with a single isolated photon (CRγ).

3. $LL\bar{E}$ and $LQ\bar{D}$ simplified models

3.1. Introduction

The simplified models with R-parity-violating SUSY decays are based on those used in the 4L SUSY search described in Sect. 2.1 [27]. Equivalently, they are similar to the simplified models with RPC squark and gluino production with a neutralino LSP used in, for example, the 0L 2–6 jets search [48], except that the addition of the RPV couplings now allow the LSP to decay. The models are classified by their SUSY production mechanisms and the decay modes of the $\tilde{\chi}_1^0$ LSP. The key difference with respect to the models used by the 4L search is that a far wider range of RPV decays is considered, including prompt $LQ\bar{D}$ decays that have never before been considered by ATLAS searches.

Gluino and squark production modes are considered, with direct decays to the neutralino LSP via $\tilde{g} \rightarrow q\bar{q}\tilde{\chi}_1^0$ and $\tilde{q} \rightarrow q\tilde{\chi}_1^0$, respectively. Squark production yields fewer jets than gluino production, which has important consequences for sensitivity in the $LQ\bar{D}$ models. Only (s)quarks of the first two generations are considered, both for simplicity and because the introduction of top quarks into the decay chains would further increase the jet and lepton multiplicities and improve sensitivity in most cases. The masses of the LSP and next-to-lightest supersymmetric particle (NLSP, i.e. either $\tilde{q}$ or $\tilde{g}$) are free parameters; all other SUSY particles are decoupled with masses set to 4.5 TeV.

The samples are generated using Herwig++ [50], using the CTEQ6L1 PDF set [51] and the UEEE3 tune of the underlying event [52]. The detector simulation uses a parametrisation of the calorimeter response [53], together with a detailed description based on Geant4 for the other detector components [54, 55]. Additional corrections are applied to the energy and momentum scales, resolutions and efficiencies of reconstructed charged leptons, jets and the $E_{\mathrm{T}}^{\mathrm{miss}}$, based on detailed comparisons between simulated

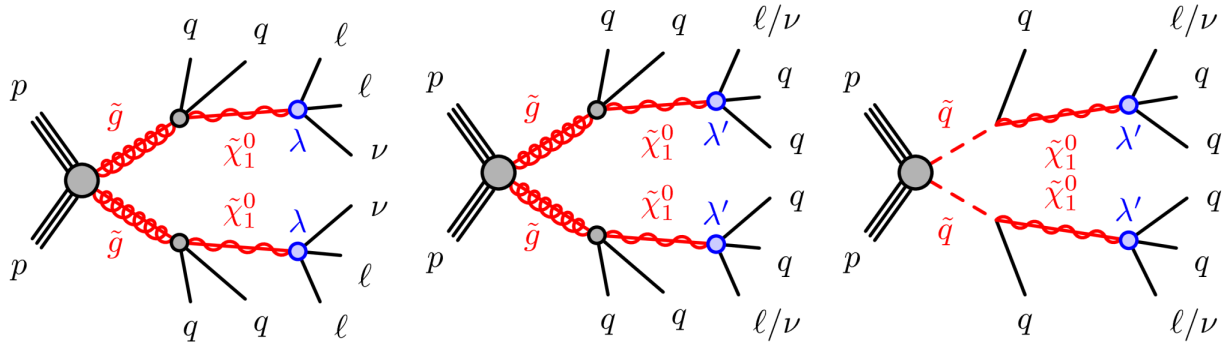

(a) $LL\bar{E}$. (b) $LQ\bar{D}$ gluino. (c) $LQ\bar{D}$ squark.

Figure 1: Diagrams illustrating the $LL\bar{E}$ and $LQ\bar{D}$ simplified models.

events and the ATLAS data. Signal cross-sections are calculated to next-to-leading order in the strong coupling constant, adding the resummation of soft gluon emission at next-to-leading-logarithmic accuracy (NLO+NLL) [56–60]. Both right- and left-handed squarks are taken into account in the squark production cross-section calculation. The nominal cross-section and the uncertainty are taken from an envelope of cross-section predictions using different PDF sets and factorisation and renormalisation scales, as described in Ref. [61].

The production and decay processes for the three simplified models are illustrated in Fig. 1, which also introduces the names used for the three models: "$LL\bar{E}$", "$LQ\bar{D}$ gluino" and "$LQ\bar{D}$ squark". These models are described further in the following.

3.1.1. $LL\bar{E}$ model

In the $LL\bar{E}$ model, the $\tilde{\chi}_1^0$ LSP decays into two charged leptons and a neutrino. All possible combinations of charged leptons, including taus, are simulated in each sample; arbitrary branching fractions are tested by reweighting the events in each sample to match the desired hypothesis. The weight applied to each LSP decay is the ratio of the desired branching fraction and the simulated branching fraction for the appropriate decay mode, and the event weight is the product of the weights from both LSPs. To reduce the number of final states to a manageable number, no distinction is made between electrons and muons when this reweighting is performed – it has already been seen that the 4L search sensitivity is comparable in the two cases [27]. Thus, there are effectively three LSP decay modes: $\ell\ell\nu$, $\ell\tau\nu$ and $\tau\tau\nu$, where ℓ (without a subscript) refers to a light lepton. If a single $LL\bar{E}$ coupling dominates, the allowed decay modes are fixed as follows ($i, j, k \in \{1, 2\}$ in the following):

$$\begin{aligned} \lambda_{ijk}: &\quad 100\%\ \ell\ell\nu; \\ \lambda_{i3k} = -\lambda_{3ik}: &\quad 50\%\ \ell\ell\nu \text{ and } 50\%\ \ell\tau\nu; \\ \lambda_{ij3}: &\quad 100\%\ \ell\tau\nu; \\ \lambda_{i33} = -\lambda_{3i3}: &\quad 50\%\ \ell\tau\nu \text{ and } 50\%\ \tau\tau\nu. \end{aligned}$$

The interpretations in this document span the LSP decay space between these extremes, using two axes to differentiate between left-handed ($L_{i/j}$) and right-handed ($\bar{E}_k$) superfields, as shown in Fig. 2a. At the

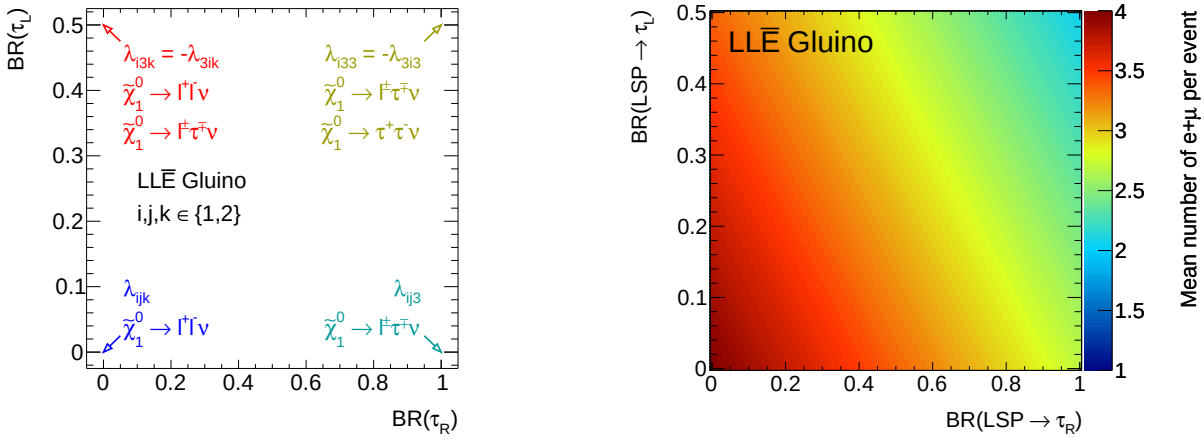

(a) (b)

Figure 2: (a) Sketch of the $LL\bar{E}$ coupling plane, showing the limiting cases of "pure" $\tilde{\chi}_1^0$ decays at the corners. (b) Mean number of light leptons per event, including those from τ decays (35.2% leptonic branching fraction assumed).

origin, the LSP decays only to light leptons, $\tilde{\chi}_1^0 \to \ell\ell\nu$. Along the x axis, the branching fraction to taus increases linearly until the LSP decays entirely to $\ell\tau\nu$. This corresponds to a transition from a regime where $LL\bar{E}$ couplings with first- and second-generation right-handed superfields dominate to one where the third generation dominates. The associated axis is marked $\mathrm{BR}(\tau_\mathrm{R})$. Along the y axis an analogous transition is made, this time involving the left-handed superfields, marked $\mathrm{BR}(\tau_\mathrm{L})$. As noted above, a maximum branching fraction of 50% to $\ell\tau\nu$ is assumed in this case (for $\mathrm{BR}(\tau_\mathrm{R}) = 0$), corresponding to a pure λ_{i3k} coupling with $i, k \neq 3$. Away from the x and y axes, a mixture of all nine possible $LL\bar{E}$ couplings exists, with $\mathrm{BR}(\tau_\mathrm{R})$ and $\mathrm{BR}(\tau_\mathrm{L})$ assumed to be independent of each other. At every point in the plane, the sum $\mathrm{BR}(\tau_\mathrm{L}) + \mathrm{BR}(\tau_\mathrm{R})$ corresponds directly to the mean number of taus produced per LSP decay, which has a maximum value of 1.5 in the upper-right corner of the plane. Figure 2b shows the mean number of light leptons per event, assuming two $\tilde{\chi}_1^0$ decays and accounting for fully leptonic tau decays. By construction this is greatest at the origin, where there must be four light leptons per event, but even in the most extreme case there are more than two light leptons per event on average, which helps to provide good signal/background discrimination in this model.

The relative rates of the different LSP decay modes are related to the squares of the appropriate $LL\bar{E}$ couplings, however the correct mapping of the RPV coupling values to the axes of Fig. 2 would need to be evaluated separately for any particular SUSY model. The reason is that the partial widths of each decay mode depend on the masses of virtual SUSY particles (in this case sleptons) that are not specified in the simplified model, and on the composition of the LSP. For the same reason, the lifetime of the LSP depends on the underlying RPV coupling values in a model-dependent way. However, for slepton and squark masses $O(1\ \mathrm{TeV})$, RPV coupling values of $\sqrt{\sum \lambda_{ijk}^2 + \sum {\lambda'_{ijk}}^2} \gtrsim 10^{-4}$ might reasonably be expected to yield a promptly decaying neutralino.

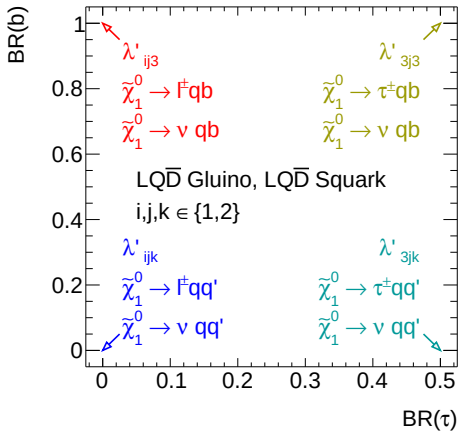

Figure 3: Sketch of the $LQ\bar{D}$ coupling plane, showing the limiting cases of "pure" $\tilde{\chi}_1^0$ decays at the corners.

3.1.2. $LQ\bar{D}$ models

In the two $LQ\bar{D}$ models, the neutralino LSP decays into two quarks and a lepton. As with $LL\bar{E}$ couplings, the precise decay modes depend on which λ'_{ijk} couplings are active. A specific non-zero coupling λ'_{ijk} allows the following decays:

$$\tilde{\chi}_1^0 \to \ell_i u_j d_k \text{ and } \tilde{\chi}_1^0 \to \nu_i d_j d_k, \tag{6}$$

where u and d denote up-type and down-type quarks, respectively. Equal branching fractions for the decay modes in Eq. (6) are assumed throughout.

As for the $LL\bar{E}$ model, no distinction is made in this analysis between fermions of the first and second generations. A neutralino LSP can decay to third-generation fermions via any or all of the superfields involved in the $LQ\bar{D}$ superpotential term. Taus can be produced with λ'_{3jk} couplings, via left-handed slepton fields, with a maximum branching ratio of 50% (the other 50% produce tau neutrinos). Similarly, λ'_{ij3} couplings involve third-generation right-handed down-type squarks and allow decays with b quarks with branching ratios up to unity. Couplings with third-generation left-handed squarks (λ'_{i3k}) are more complicated due to the large top-quark mass affecting the relative rates of ℓtq vs νbq decays, which will not be discussed further here. Only the first two variations described will be considered. Again, a two-dimensional coupling plane is constructed, illustrated in Fig. 3, with the branching ratio to taus and b-quarks as independent free parameters. In the same way as for the $LL\bar{E}$ model, the LSP lifetime and the branching fractions used here relate to the underlying λ'_{ijk} couplings in a model-dependent way.

3.1.3. Sparticle masses and kinematics

Each simulated sample is generated with a fixed ratio R between the LSP and NLSP masses, which take the values

$$R = \frac{m(\tilde{\chi}_1^0)}{m(\text{NLSP})} = 0.1, 0.5 \text{ or } 0.9. \tag{7}$$

The 4L analysis has already demonstrated sensitivity to a wide range of $\tilde{\chi}_1^0$ masses (10 to $m_{\text{NLSP}} - 10$ GeV) in the case of $LL\bar{E}$ decays. The sensitivity to prompt $LQ\bar{D}$ decays has not previously been explored by

NLSP	RPV decays	m(NLSP)	R
$\tilde{g}$	$LL\bar{E}$	800–1600 GeV	0.1
$\tilde{g}$	$LL\bar{E}$	1000–1600 GeV	0.5
$\tilde{g}$	$LL\bar{E}$	1000–1600 GeV	0.9
$\tilde{g}$	$LQ\bar{D}$	600–1400 GeV	0.1
$\tilde{g}$	$LQ\bar{D}$	800–1400 GeV	0.5
$\tilde{g}$	$LQ\bar{D}$	800–1400 GeV	0.9
$\tilde{q}$	$LQ\bar{D}$	600–1000 GeV	0.1
$\tilde{q}$	$LQ\bar{D}$	600–1200 GeV	0.5
$\tilde{q}$	$LQ\bar{D}$	800–1400 GeV	0.9

Table 7: Simulated signal samples for the $LL\bar{E}$ and $LQ\bar{D}$ simplified models. The samples are defined by the choice of NLSP ($\tilde{g}$ or $\tilde{q}$) and its mass, the mass ratio $R = m(\tilde{\chi}_1^0)/m(\text{NLSP})$ and the RPV decay pattern of the $\tilde{\chi}_1^0$. In every case, the NLSP mass is incremented by 200 GeV between samples.

any ATLAS search, except in the case of direct decays of third-generation squarks [22]. More details on the sparticle masses used in each model are given in Table 7.

Fixing R at particular values keeps the speed of the LSP in the rest frame of the NLSP approximately constant as the NLSP mass increases. Some consequences of this are shown in the kinematic distributions of Figs. 4 and 5, which are made for illustration without any detector simulation. The decay products of the LSP become softer and/or more collimated as R decreases, an effect which can be seen in both Figs. 4a and 5, where the relevant particles (charged leptons and neutrinos, respectively) arise only from the LSP decays. In contrast, the particles from the NLSP cascade decays become more energetic and well-separated. This is illustrated for jets in the $LL\bar{E}$ model in Fig. 4b, which arise from the gluino decays and also the underlying event, which is the same in all three cases. Thus, the value of R effectively determines how the available energy is shared between the final-state objects, and may affect the optimal choice of search strategy for a given model. In particular, the case of low values of R is expected to challenge existing analyses due to the reduced $E_{\text{T}}^{\text{miss}}$ from neutralino decays, and ultimately may require special techniques to detect [62].

3.2. Analysis strategy

Recalling Table 1, it is expected that a variety of existing ATLAS analyses have the potential to be sensitive to the $LL\bar{E}$ and $LQ\bar{D}$ simplified models described above. In the case of the $LL\bar{E}$ model, there are four charged leptons in every event, and at least half of these are light leptons (see Fig. 2b). Thus, we consider analyses that require high charged-lepton multiplicities, as the additional background rejection from this requirement allows looser requirements on other criteria such as $E_{\text{T}}^{\text{miss}}$. The 4L analysis was specifically designed with $LL\bar{E}$ RPV decays in mind, and includes selections with hadronically decaying taus as well as light leptons. Here, for the first time, the SS/3L analysis is also considered. The requirement of a high jet multiplicity (see Table 3) is easily fulfilled for the gluino model considered here, while the lower lepton multiplicity requirement leads to gains in the signal efficiency with respect to the 4L analysis.

All of the search channels in Table 1 requiring zero or one light lepton are potentially sensitive to one or more of the $LQ\bar{D}$ models, although the analysis sensitivity is expected to be reduced with respect to RPC SUSY models, as the only source of $E_{\text{T}}^{\text{miss}}$ is from neutrinos produced in decays of the $\tilde{\chi}_1^0$ LSP.

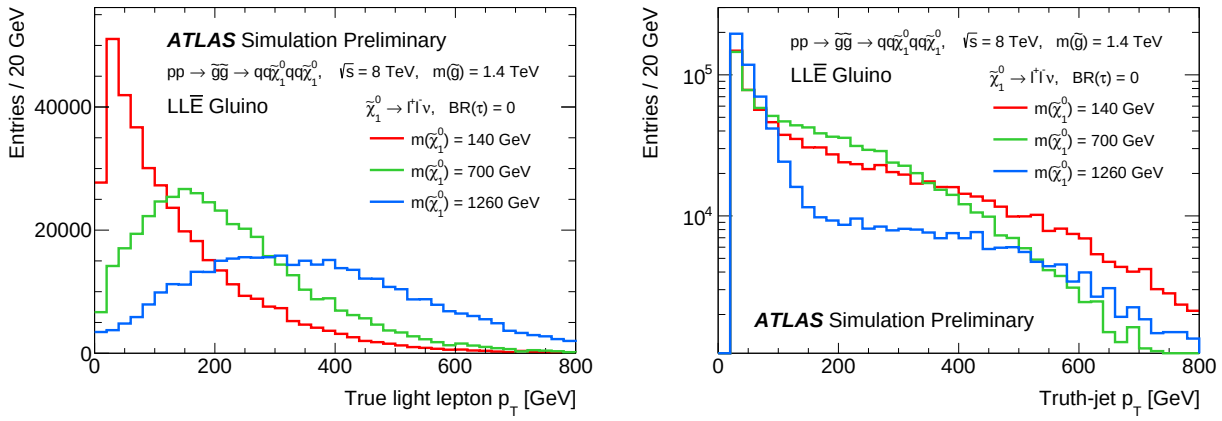

(a) (b)

Figure 4: (a) Light-lepton p_{T} distributions and (b) jet p_{T} distributions for three different $\tilde{\chi}_1^0$ masses in the $LL\bar{E}$ model with $m(\tilde{g}) = 1.4$ TeV. All light leptons with $p_{\mathrm{T}} > 10$ GeV and $|\eta| < 2.5$ are shown, while jets are required to have $p_{\mathrm{T}} > 20$ GeV and $|\eta| < 4.5$.

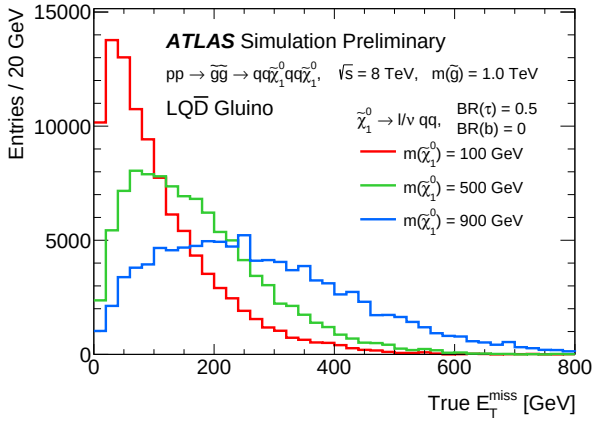

Figure 5: $E_{\mathrm{T}}^{\mathrm{miss}}$ distributions for three different $\tilde{\chi}_1^0$ masses in the $LQ\bar{D}$ gluino model with $m(\tilde{g}) = 1.0$ TeV.

While in principle events with two light leptons are also produced, the SS/3L analysis is found to be insensitive, due to the lack of hard neutrinos from the $\tilde{\chi}_1^0$ decays in this case. The 0L 7–10 jets search is only considered for the model with gluino pair production, as too few jets are produced in the squark model to satisfy the selection criteria.

In all three models, the method for setting the best limit on SUSY production is the same. Each point in the parameter space is fully described by the model type, the LSP/NLSP mass ratio R, the NLSP mass $m_{\tilde{g}/\tilde{q}}$, and the (x, y) position in the coupling plane. At each of these points, each channel uses its own selection and statistical analysis procedure to set a 95% confidence level (CL) exclusion limit on the signal strength, μ_{lim}. By convention, limits are set with respect to the theoretical signal cross-section reduced by one standard deviation, and $\mu_{\text{lim}} = 1$ corresponds exactly to exclusion of this cross-section. The expected μ_{lim} value, assuming no signal in the data, is also calculated at each point by each channel. Channels within a single search are statistically combined where possible, as described in the corresponding analysis papers.[2] Channels from different searches are not combined, and sometimes it is also not possible to combine channels within a single search. Where multiple sensitive channels cannot be combined, the channel with the best expected limit is chosen to constrain each point in the parameter space. The corresponding observed μ_{lim} values are used directly to extract limits on the production cross-section at each point (with results in Apps. A, B and C). Lower bounds on the NLSP mass are obtained by linear interpolation of $\ln(\mu_{\text{lim}})$ between points with different NLSP masses. The limit is placed at the mass where $\mu_{\text{lim}} = 1$.

Experimental systematic uncertainties on the signal modelling are estimated using the procedures described within each analysis paper. Model-dependent theoretical uncertainties on the analysis acceptance are also accounted for. These are calculated by varying the renormalisation and factorisation scales, as well as the amount of initial- and final-state radiation. Events are generated for each variation using MadGraph 5 v1.5.12 [63], with showering performed by Pythia 6.427 [64]. No detector simulation is performed; instead, kinematic selections are applied to the generated particles, as described in Ref. [65]. For the 4L and SS/3L analyses, the corresponding uncertainties are of order a few percent, and small compared to other sources of uncertainty. In the 1L search these uncertainties are neglected as they are estimated to be negligible. For the 0L 2–6 jets and 0L 7–10 jets analyses, these uncertainties can reach as high as $\sim 30\%$ for $R = 0.1$, with a statistical precision of about 5%. Compared to the other searches, these two analyses use higher jet p_{T} thresholds, and are therefore more reliant on QCD radiation in order to satisfy the SR selection criteria. In such cases, this is often the dominant source of systematic uncertainty on the model's acceptance.

As described in Sect. 2, it is important to also consider the potential contamination of signal events in control and validation regions used by these searches. Upon examination, it is found that the contamination is almost always significant only for low squark and gluino masses that are very well excluded (often by more than one search). For example, there is significant contamination in the SS/3L validation regions in the $LL\bar{E}$ model with $m(\tilde{g}) = 800$ GeV and $R = 0.1$, but this scenario has already been conclusively ruled out by the 4L search [27]. Similarly, the contamination of CRW in the 0L 2–6 jets search can reach as high as 55% of the observed events in data for the $LQ\bar{D}$ gluino model with $m(\tilde{g}) = 1.0$ TeV, but when the 1L results are taken into account this too is far from the observed mass limit. The main exception to this trend occurs for CRQ in the 0L 2–6 jets analysis and in the control regions used to control the $t\bar{t}$ and W+jets backgrounds in the 0L 7–10 jets analysis. In both cases, the SUSY signal can saturate the observed data in the control regions. For the 0L 2–6 jets analysis, this is important only when the LSP

[2] For the purposes of this discussion, a "search" corresponds to a single row of Table 1.

is relatively light ($R = 0.1$), while for the 0L 7–10 jets analysis it is important for $m(\tilde{g}) \lesssim 1$ TeV. In both cases, the control region contamination is taken into account when setting limits, which can weaken them relative to hypothetical scenarios where this effect could be neglected. This indicates that to fully optimise these searches for RPV SUSY scenarios, alternative background estimation techniques would need to be explored.

3.3. Results

The lower limits on the gluino mass for the $LL\bar{E}$ simplified models are shown in Figs. 6 and 7, for the three values of R that are considered. The observed and expected limits are evaluated based on the nominal signal cross-section reduced by its 1σ theoretical uncertainty. For $R = 0.1$ and 0.5, the best constraints come from the SS/3L search. The 4L analysis provides weaker constraints, despite targeting RPV SUSY, as it was not optimised explicitly for squark and gluino production. In the SS/3L analysis, different signal regions are statistically combined, however the constraints are driven by the SR3Lhigh signal region defined in Table 3. This region requires at least three light leptons, and as a result the strongest constraints are set when the LSP decays entirely to light leptons in the lower left corner of the plane. Comparing with Fig. 2, it can be seen that the limits weaken as the average number of light leptons per event decreases. In the case of $R = 0.9$, the jets from the gluino decays are less energetic and the 4L analysis can constrain the model more strongly in the region indicated in Fig. 7c, where the average light lepton multiplicity is greater than approximately 3.4. The constraint in this case is dominated by the SR0noZb region, which requires at least four light leptons, and the signal regions with taus do not contribute significantly to the final results. Overall, the strongest constraints are obtained for $R = 0.5$ where the available energy can be distributed more or less evenly between all of the leptons and jets, and the weakest constraints for tau-rich scenarios are obtained for $R = 0.1$ where the light leptons from leptonic tau decays are more likely to be soft or collimated with other leptons.

A selection of upper cross-section limits for the $LL\bar{E}$ model are shown in Fig. 8, corresponding to the pure $LL\bar{E}$ couplings at the four corners of the coupling plane, for which explicit decay patterns were given in Fig. 2a. The observed and expected limits show a strong dependence on the average light lepton multiplicity in the LSP decays. By comparison, the dependence of the limits on the gluino mass is relatively weak. The complete set of upper limits on the production cross-section for this model and more details on which analysis results are used at each point in the parameter space are given in App. A.

Corresponding lower limits on the gluino mass for the $LQ\bar{D}$ gluino model are shown in Figs. 9 and 10. The signal model nominally produces eight jets (in addition to jets from hadronically decaying taus), and for $R = 0.1$ and 0.5 the 0L 7–10 jets analysis produces the strongest constraints. The statistical combination of signal regions requiring a b-jet and those with a b-jet veto (see Table 5) leads to a non-trivial dependence on BR(b), with values of 0 and 1 being preferred. The limits also have a strong dependence on BR(τ), as a veto on light leptons is applied. As for the $LL\bar{E}$ model, the mass limits are weaker for $R = 0.1$ than $R = 0.5$, with the higher p_{T} thresholds for jets compared to leptons significantly amplifying the observed effect. For $R = 0.9$ the SUSY spectrum is compressed and the 0L 7–10 jets analysis no longer produces the best results, as it is highly dependent on reconstructing the jets from the gluino cascade. The 1L and 0L 2–6 jets analyses set powerful constraints in the regions BR(τ) ≤ 0.1 and ≥ 0.3, respectively. The final expected limits depend only weakly upon BR(τ) and BR(b), due to the excellent complementarity between the two searches.

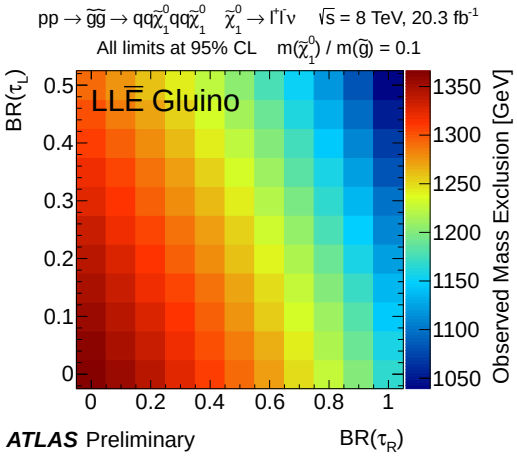

(a) Observed, $R = 0.1$.

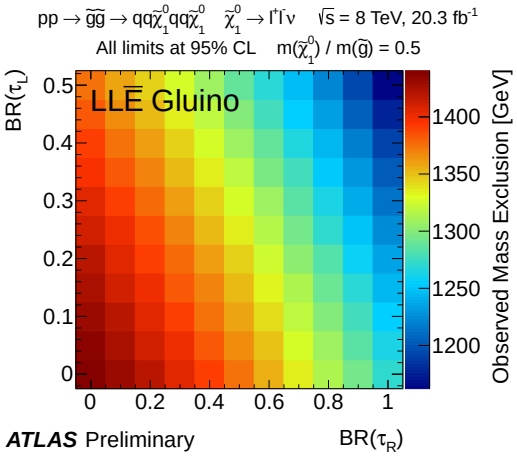

(b) Observed, $R = 0.5$.

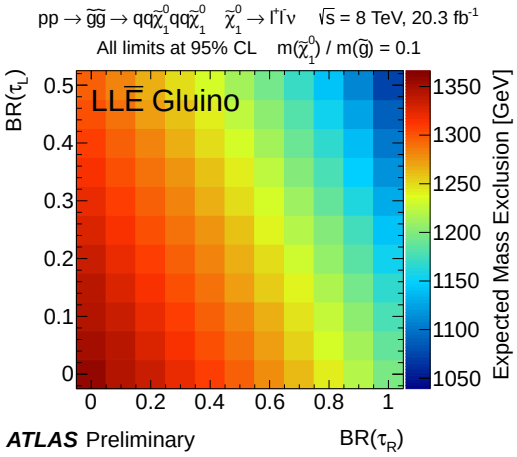

(c) Expected, $R = 0.1$.

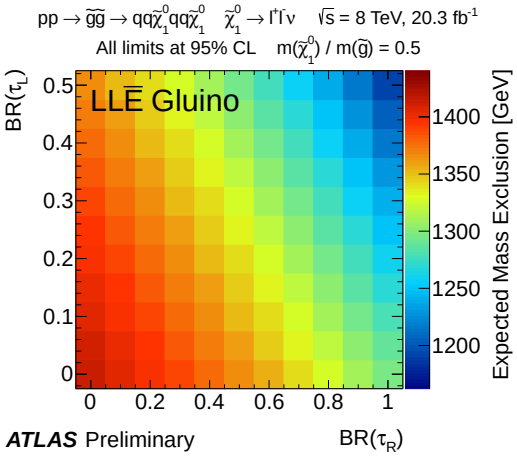

(d) Expected, $R = 0.5$.

Figure 6: Observed and expected 95% lower limits on the gluino mass for the $LL\bar{E}$ simplified model with $R = 0.1$ and 0.5. These limits are obtained using the SS/3L search results.

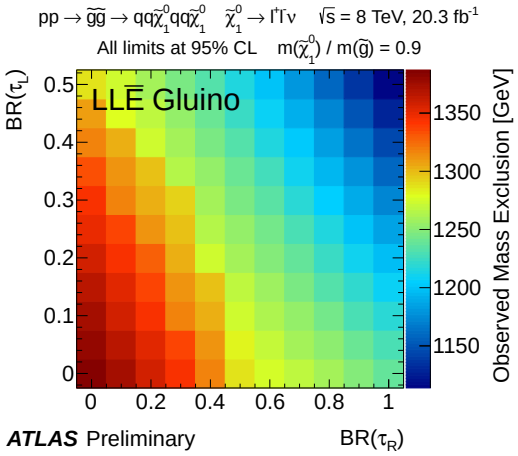

(a) Observed, $R = 0.9$.

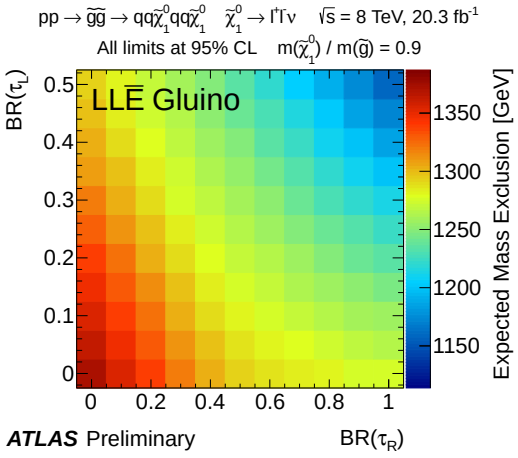

(b) Expected, $R = 0.9$.

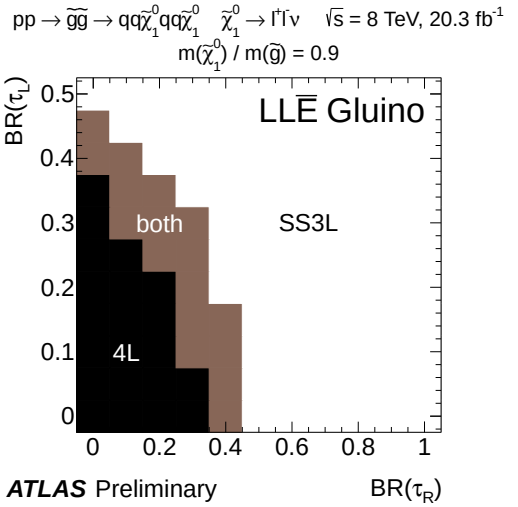

(c) Channel used, $R = 0.9$.

Figure 7: Observed and expected 95% lower limits on the gluino mass for the $LL\bar{E}$ simplified model with $R = 0.9$. Figure (c) indicates which search was used to obtain the observed limits, or where results from two searches were interpolated to produce the final limit. See Figs. 26 and 27 for further details.

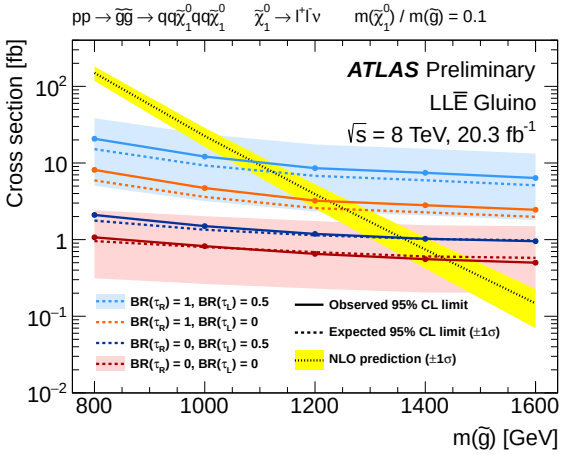

(a) $R = 0.1$.

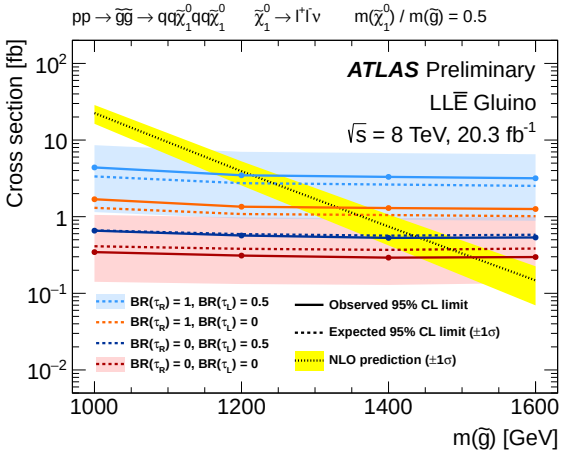

(b) $R = 0.5$.

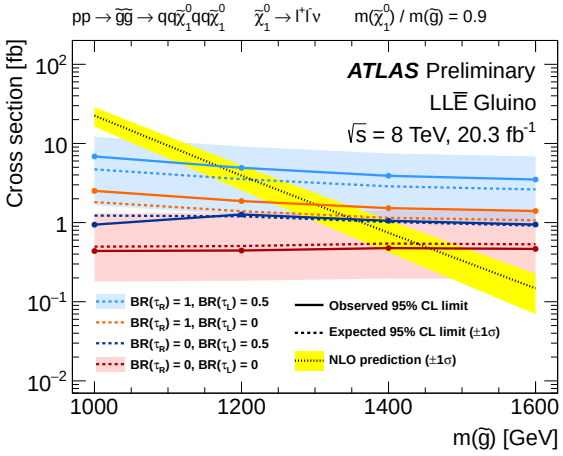

(c) $R = 0.9$.

Figure 8: Observed and expected cross-section limits for the $LL\bar{E}$ simplified model with decays corresponding to the corners of the parameter space in Figs. 6 and 7. The shaded bands show the effect on the expected limits of varying the experimental systematic uncertainties by $\pm 1\sigma$ for two of the four hypotheses, corresponding to the best ($\mathrm{BR}(\tau_R) = \mathrm{BR}(\tau_L) = 0$) and worst ($\mathrm{BR}(\tau_R) = 1$, $\mathrm{BR}(\tau_L) = 0.5$) expected limits. The theoretical cross-section for gluino pair production is also shown, together with its uncertainty. For details of which analyses contribute in each case, see App. A.

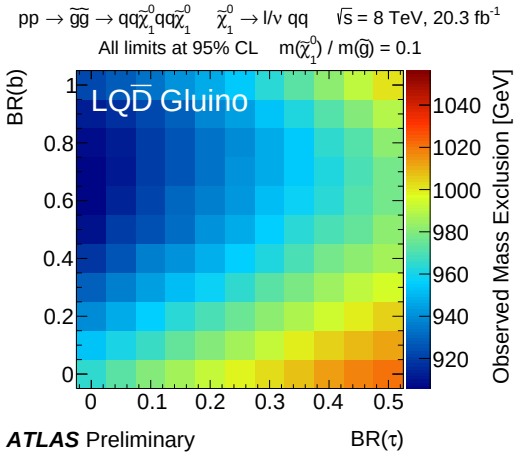

(a) Observed, $R = 0.1$.

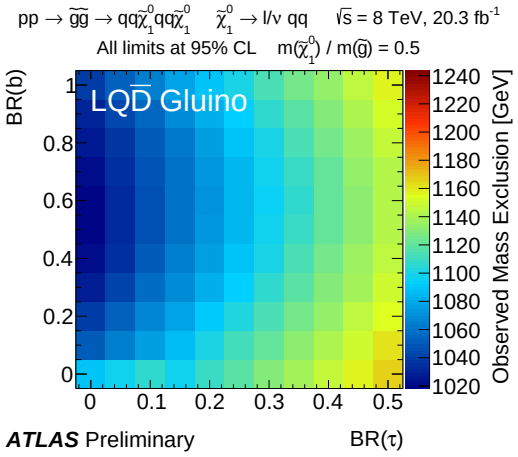

(b) Observed, $R = 0.5$.

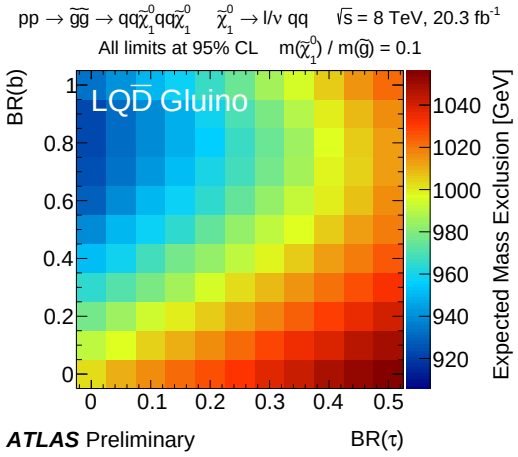

(c) Expected, $R = 0.1$.

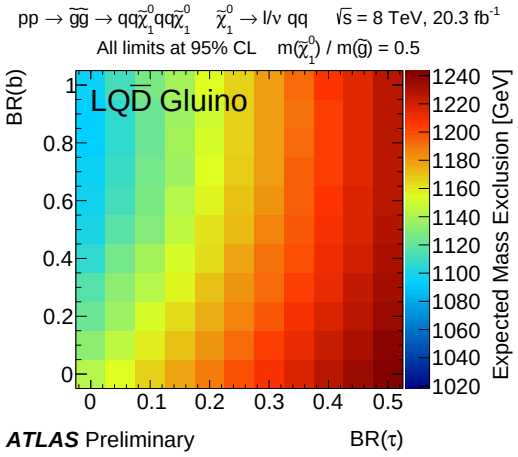

(d) Expected, $R = 0.5$.

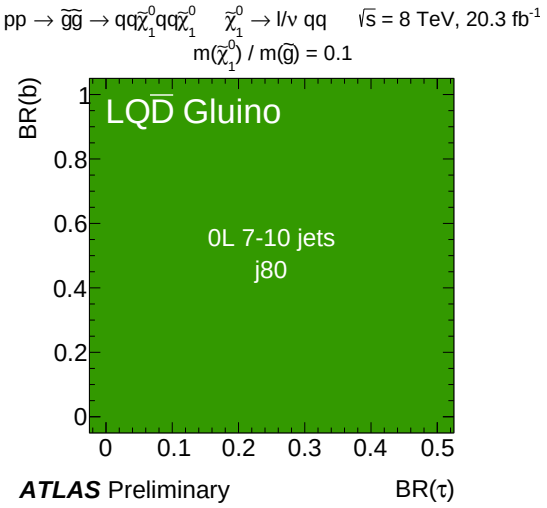

(e) Channel used, $R = 0.1$.

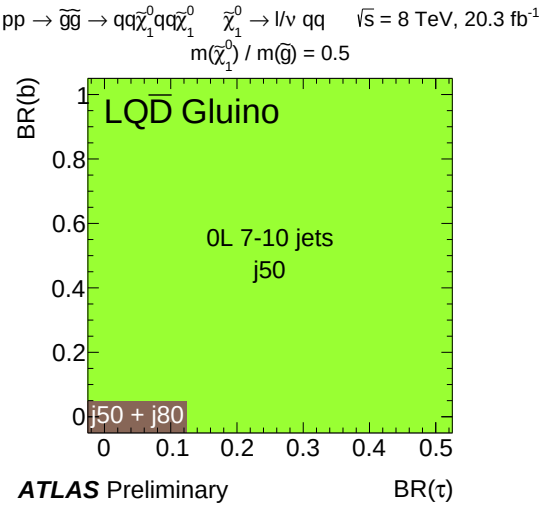

(f) Channel used, $R = 0.5$.

Figure 9: Observed and expected 95% lower limits on the gluino mass for the $LQ\bar{D}$ gluino simplified model with $R = 0.1$ and 0.5. Figures (e) and (f) indicate which search was used to obtain the observed limits, or where results from two searches were interpolated to produce the final limit. See Figs. 28–32 for further details.

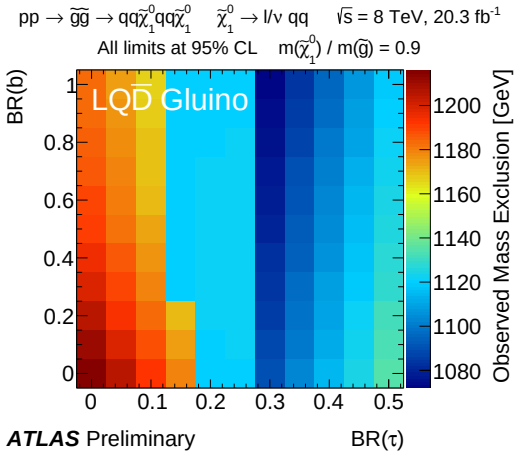

(a) Observed, $R = 0.9$.

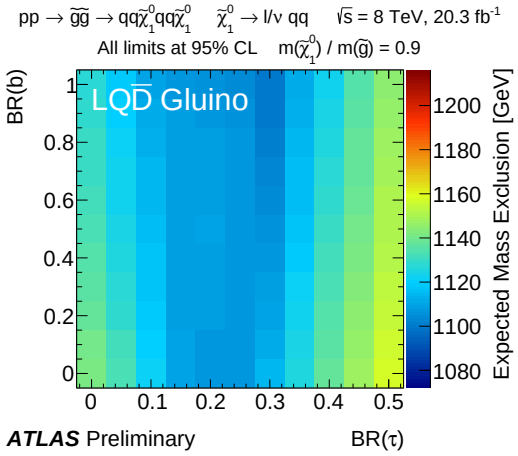

(b) Expected, $R = 0.9$.

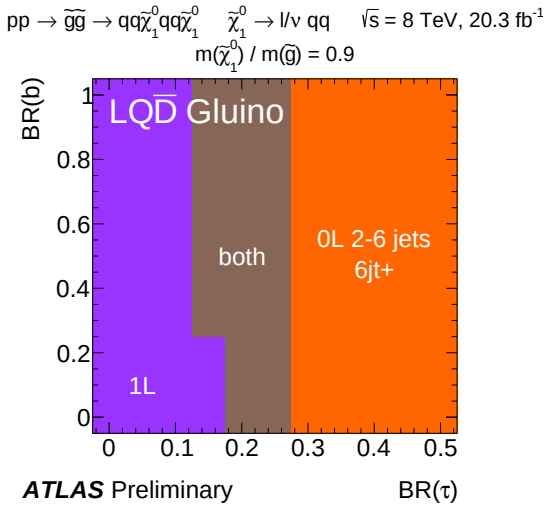

(c) Channel used, $R = 0.9$.

Figure 10: Observed and expected 95% lower limits on the gluino mass for the $LQ\bar{D}$ gluino simplified model with $R = 0.9$. Figure (c) indicates which search was used to obtain the observed limits, or where results from two searches were interpolated to produce the final limit. See Figs. 33 and 34 for further details.

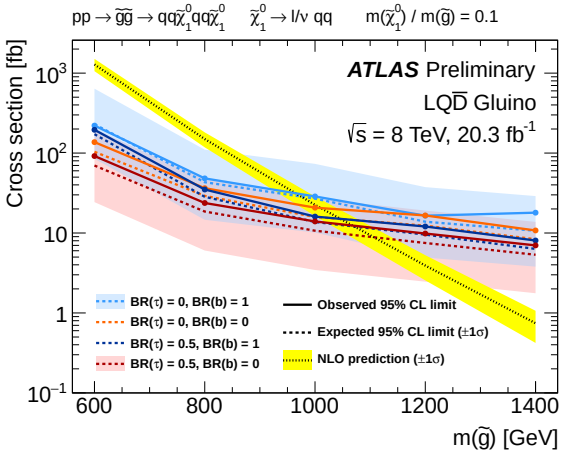

(a) $R = 0.1$.

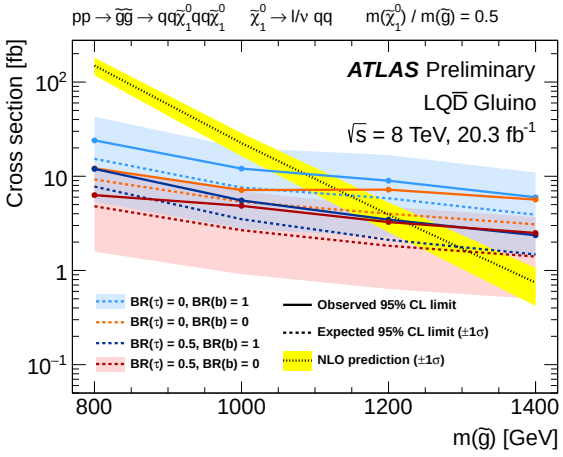

(b) $R = 0.5$.

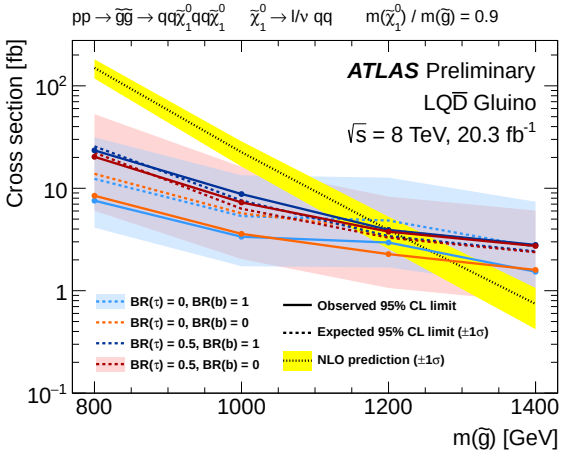

(c) $R = 0.9$.

Figure 11: Observed and expected cross-section limits for the $LQ\bar{D}$ gluino simplified model with decays corresponding to the corners of the parameter space in Figs. 9 and 10. The shaded bands show the effect on the expected limits of varying the experimental systematic uncertainties by $\pm 1\sigma$ for two of the four hypotheses, corresponding to scenarios with few (BR(τ) = 0.5, BR(b) = 0) and many (BR(τ) = 0, BR(b) = 1) light leptons. The theoretical cross-section for gluino pair production is also shown, together with its uncertainty. For details of which analyses contribute in each case, see App. B.

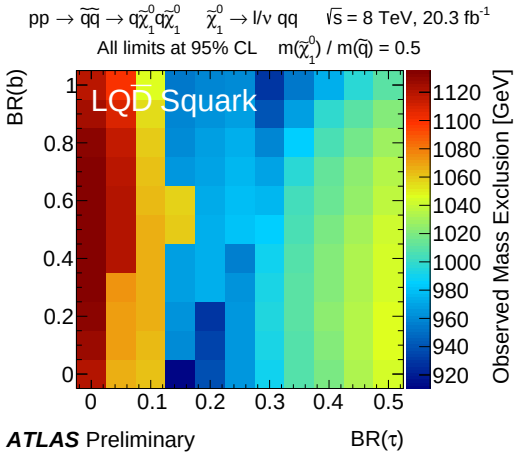

(a) Observed, $R = 0.5$.

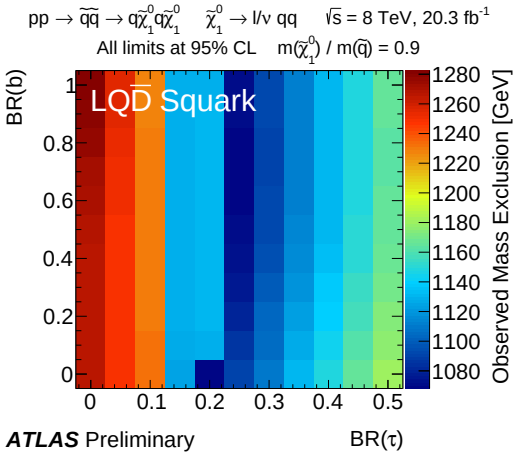

(b) Observed, $R = 0.9$.

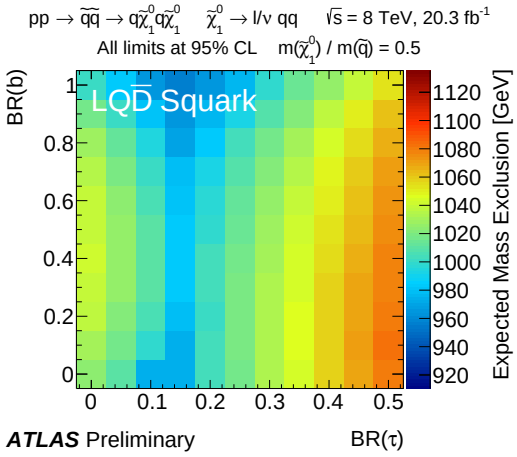

(c) Expected, $R = 0.5$.

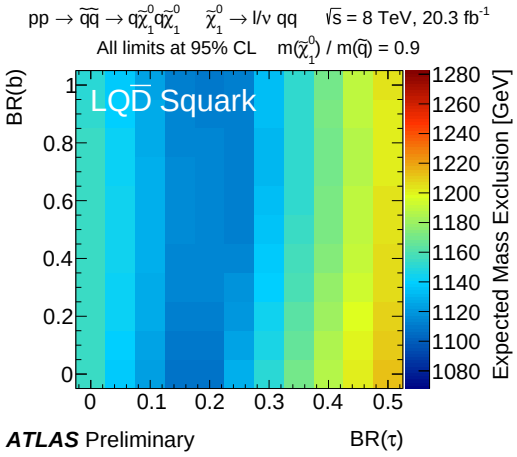

(d) Expected, $R = 0.9$.

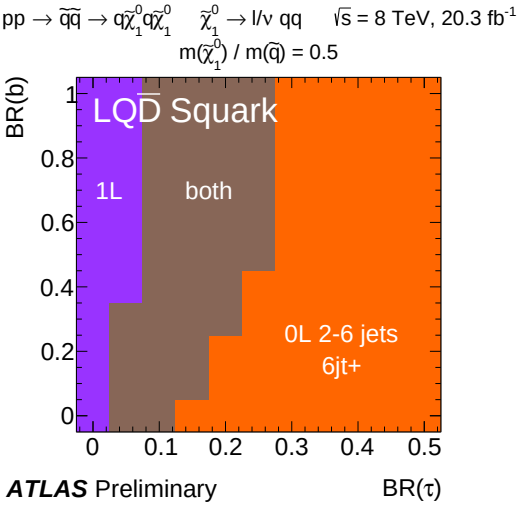

(e) Channel used, $R = 0.5$.

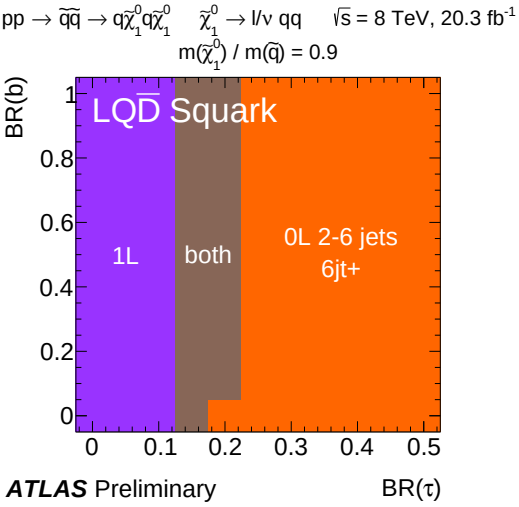

(f) Channel used, $R = 0.9$.

Figure 12: Observed and expected 95% lower limits on the squark mass for the $LQ\bar{D}$ squark simplified model with $R = 0.5$ and 0.9. Figures (e) and (f) indicate which search was used to obtain the observed limits, or where results from two searches were interpolated to produce the final limit. See Figs. 37–40 for further details.

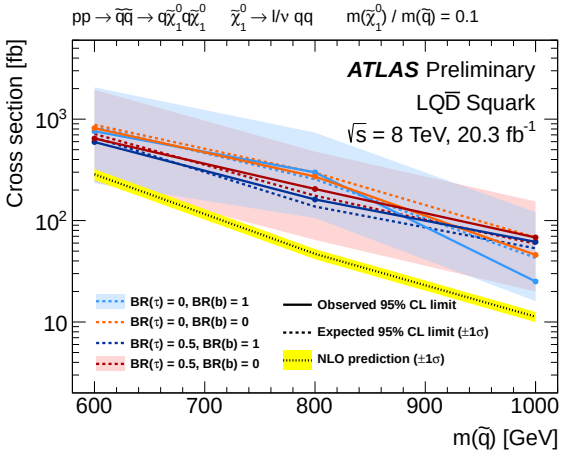

(a) $R = 0.1$.

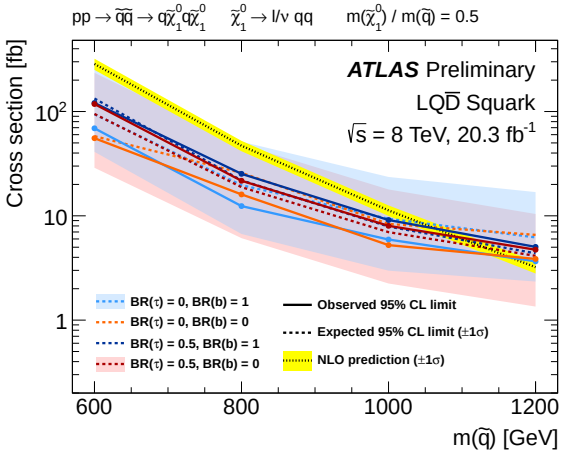

(b) $R = 0.5$.

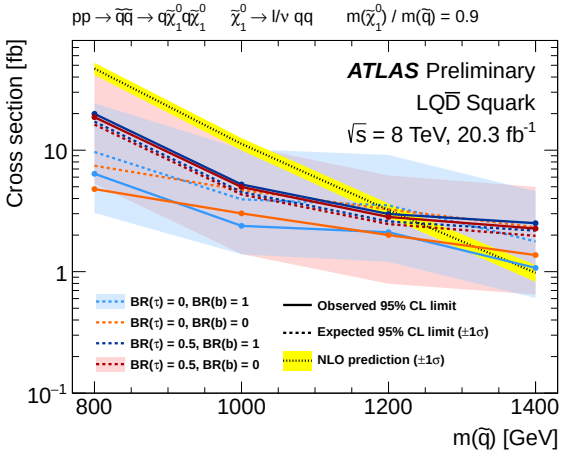

(c) $R = 0.9$.

Figure 13: Observed and expected cross-section limits for the $LQ\bar{D}$ simplified model with squark production in the case of pure couplings, corresponding to the corners of the parameter space in Fig. 12. The lines and bands shown are the same as for Fig. 11. For details of which analyses contribute in each case, see App. C. In (a), the 1L search is not considered for $m(\tilde{q}) = 600$ and 800 GeV, as described in the text.

The upper cross-section limits for the $LQ\bar{D}$ gluino model for the four points on the corners of the coupling space considered are shown in Fig. 11. Both observed and expected limits show a strong dependence on the gluino mass, indicating in each case that the analysis acceptance is greater for more massive SUSY particles. This dependence is less for $R = 0.5$ than for the other values of R, where it is expected that all jets (i.e. from the LSP decay and the cascade) are easier to reconstruct. The complete set of upper limits on the production cross-section for this model and more details on which analysis results are used at each point in the parameter space are given in App. B.

Lower limits on the squark mass for the $LQ\bar{D}$ squark simplified model with $R = 0.5$ and 0.9 are shown in Fig. 12, assuming that the left- and right-handed squarks of the first two generations are degenerate. Due to the lower number of jets from squark decays compared to gluino decays (see Fig. 1), the limits on this model are set only by the 0L 2–6 jets and 1L analyses. The dependence of the expected limits on $\mathrm{BR}(\tau)$ is more marked than in the case of Fig. 10b, which is consistent with a greater reliance on jets from hadronic tau decays due to the reduced number of jets from quarks. As neither analysis specifically requires or rejects b-jets, the dependence of the expected limits on $\mathrm{BR}(b)$ is weak.

The upper cross-section limits for the $LQ\bar{D}$ squark model are shown in Fig. 13. These limits vary strongly as a function of $m(\tilde{q})$, meaning that changes in the model would have a significant impact on the mass limits shown in Fig. 12. In particular, it is assumed here that left- and right-handed squarks of the first two generations are degenerate. Reducing the number of active squarks would significantly reduce the constraints on their masses, or eliminate them altogether. Even with this assumption, the cross-section limits for $R = 0.1$ are mostly a factor of 3–5 worse than the theoretical cross-section, nearly independently of $m(\tilde{q})$, and a lower limit on the squark mass cannot be set.[3] This loss of sensitivity is due to a number of factors, mainly the low acceptance due to the reduced $E_{\mathrm{T}}^{\mathrm{miss}}$ in this scenario (similar to that observed in Fig. 5). The signal contamination in the 0L 2–6 jets multi-jet control region CRQ mentioned in Sect. 3.2 also plays a role in this result. Lowering the $E_{\mathrm{T}}^{\mathrm{miss}}$ requirements of these searches could in principle strengthen this result, although estimation of the multi-jet background would be a significant challenge. The complete set of upper limits on the production cross-section for this model and more details on which analysis results are used at each point in the parameter space are given in App. C.

4. Bilinear R-parity violation

As outlined in Sect. 1.1, ATLAS searches have already placed constraints on bilinear R-parity-violating scenarios with mSUGRA assumptions [40, 41]. Overall, the constraints are equivalent to $m(\tilde{g}) \gtrsim 1.35$ TeV, comparable to or even beyond those obtained for the equivalent mSUGRA model with R-parity conservation. Strong limits on RPC scenarios like mSUGRA have motivated the study of so-called *natural SUSY*, which requires that those SUSY particles most essential for naturalness (top squarks and higgsinos) have masses of less than about 1 TeV, while putting less stringent constraints on the other sparticle masses [66–68]. Here, the phenomenological minimal supersymmetric Standard Model (pMSSM) [25] is used to study a natural SUSY scenario with bilinear R-parity violation for the first time. In the definition of the the pMSSM parameters all model points are, by design, fully compatible with both the observed Higgs boson mass and measurements of neutrino oscillations.

[3] The 1L search is not considered for the points with $m(\tilde{q}) = 600$ and 800 GeV in Fig. 13a, due to statistical fluctuations caused by the very low event acceptance for this model. Uniquely among the considered searches, the 1L analysis uses a fit to the shape of $m_{\mathrm{eff}}^{\mathrm{incl}}$ and $E_{\mathrm{T}}^{\mathrm{miss}}$, which increases its susceptibility to this effect. This choice leads to slightly weaker but more robust limits for $\mathrm{BR}(\tau) \leq 0.2$.

The description of this study is split into five parts. Section 4.1 introduces the conceptual aspects of the model, together with the main constraints placed on the SUSY parameters. The phenomenology of the model is discussed in Sect. 4.2, which informs the choice of analyses used to constrain this model, described in Sect. 4.3. The specific model parameters used to make simulated event samples are described in Sect. 4.4, and finally the results are shown in Sect. 4.5.

4.1. Introduction

The terms in Eq. (1a) with coefficients ϵ_i ($i = 1,2,3$) lead to lepton-number violating mixing between the lepton and Higgs superfields. An additional soft SUSY-breaking term, $-B_i\epsilon_i\tilde{L}_i H_2$, also arises, leading to three extra parameters B_i. In general, there is no basis where both sets of bilinear RPV terms $\epsilon_i L_i H_2$ and $B_i\epsilon_i\tilde{L}_i H_2$ can be eliminated at the same time, although they may be suppressed with respect to other RPV terms as they are constrained by neutrino oscillation data. In *b*RPV SUSY models, it is assumed that the bilinear terms are phenomenologically most relevant and trilinear RPV couplings are set to zero.

The theory of *b*RPV SUSY is predictive, due to its connections to other phenomena. For example, the electroweak symmetry is broken in *b*RPV theories when mixtures of the scalar Higgs and sneutrino fields acquire vacuum expectation values. Also, neutrino masses are generated via neutralino-neutrino mixing [69]. These two connections help to determine the experimental signatures of *b*RPV SUSY, in particular the decay modes of the LSP can be predicted from measurements of neutrino oscillations [70]. These constraints on the *b*RPV couplings, spectra and decays are calculated using the SPheno code [71, 72].

The *b*RPV couplings that are consistent with the above constraints are small enough to not substantially alter most sparticle production and decay processes predicted by equivalent RPC SUSY models. The most important difference in collider phenomenology arises from decays of the LSP. A complete overview of the possible LSP candidates and their corresponding *b*RPV decay modes is given in Ref. [73]. Here, we focus on a neutralino LSP that decays promptly, typically into a gauge boson and a lepton.

In natural SUSY, gluinos and first- and second-generation squarks may be massive enough to have escaped current searches, while simultaneously being consistent with the idea of naturalness and a Higgs boson mass of 125 GeV [66, 74, 75]. The pMSSM is used to explore this scenario. The LSP is assumed to be a higgsino-like neutralino, with associated $\tilde{\chi}_1^{\pm}$ and $\tilde{\chi}_2^0$ states that are nearly degenerate with the LSP. The masses of these particles are controlled by the higgsino mass parameter μ [66]. The third generation squarks, essential for naturalness, are also light ($m < 1$ TeV), while other SUSY particles are assumed to be more massive. Here, $m_{\tilde{q}_{\mathrm{L},3}}$, the mass parameter for left-handed top and bottom squarks, is taken as the free parameter of the third-generation squark sector. The characteristics of this two-dimensional $\mu - m_{\tilde{q}_{\mathrm{L},3}}$ parameter space are discussed in Sect. 4.2, and precise details of the simulated samples are given in Sect. 4.4. The remaining pMSSM and *b*RPV parameters are assigned values as follows:

- The wino and bino mass parameters are assigned values of $M_2 = 3\mu$ and $M_1 = 3000$ GeV, respectively. The relatively low wino mass parameter ensures that the light higgsino states are separated by a few GeV in mass, while the associated wino-like $\tilde{\chi}_2^{\pm}$ and $\tilde{\chi}_3^0$ states are sufficiently decoupled that their direct production is suppressed, leading to a maximum wino production cross-section of order 10^{-3} of the total cross-section.
- The mass parameter for right-handed top squarks $m_{\tilde{u}_3}$ and the trilinear stop mixing parameter A_t are adjusted to give a Higgs boson mass in the range 125 ± 2 GeV assuming maximal stop mixing.

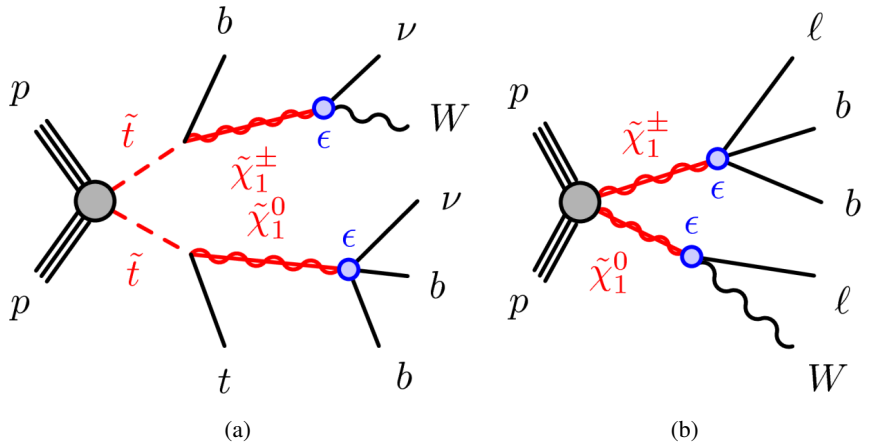

Figure 14: Example diagrams illustrating the natural *b*RPV pMSSM model. They illustrate third generation squark production (a) and electroweak production (b), with subsequent *b*RPV decays in each case.

As discussed e.g. in Refs. [74, 76, 77], this assumption leads to relatively light stop masses. The net effect of this constraint is that $m_{\tilde{u}_3}$ is anti-correlated with $m_{\tilde{q}_{\mathrm{L},3}}$, the effect of which is further explored in Sect. 4.2.

- The gluino mass $m_{\tilde{g}}$ is set to 1700 GeV, sufficiently high that gluino pair production is suppressed by at least a factor of a thousand with respect to third-generation squarks, neutralinos, and charginos. A less massive gluino would increase the total SUSY cross-section and likely strengthen any limits set by this analysis.
- All other SUSY particles are decoupled, having masses of 3 TeV.
- A moderate value of $\tan\beta = 30$ is used, where $\tan\beta$ is the ratio of the expectation values of the two Higgs fields. It is not expected that the results should depend strongly upon this choice. When varying $\tan\beta$ by ± 10, changes in the sparticle masses are negligible, while changes of up to 20% in the branching ratios of the dominant LSP decay modes are observed. This could lead to small changes in the sensitivity as $\tan\beta$ is varied, although the fact that no optimisation for specific *b*RPV decay modes has been performed should mitigate this effect.
- The *b*RPV parameters are determined from fitting to neutrino oscillation data and electroweak symmetry breaking, using SPheno version 3.3.2 [71, 72].

The dominant production processes are based on pair production of the kinematically accessible stops, sbottoms, charginos and neutralinos. Two diagrams illustrating relevant production and decay processes are shown in Fig. 14.

The signal samples are generated using Pythia 6.423 [64] with CTEQ6L1 [51] parton distribution functions. Signal cross-sections for third-generation squark production are calculated to next-to-leading order (NLO) in the strong coupling constant, adding the resummation of soft gluon emission at next-to-leading-logarithmic accuracy (NLO+NLL) [60, 78, 79]. The cross-sections for electroweak production of charginos and neutralinos are calculated to NLO in the strong coupling constant using Prospino2 [56]. They are in agreement with NLO+NLL calculations within $\sim 2\%$ [80, 81]. In all cases, the nominal cross-section and the uncertainty are taken from an envelope of cross-section predictions using different PDF sets and

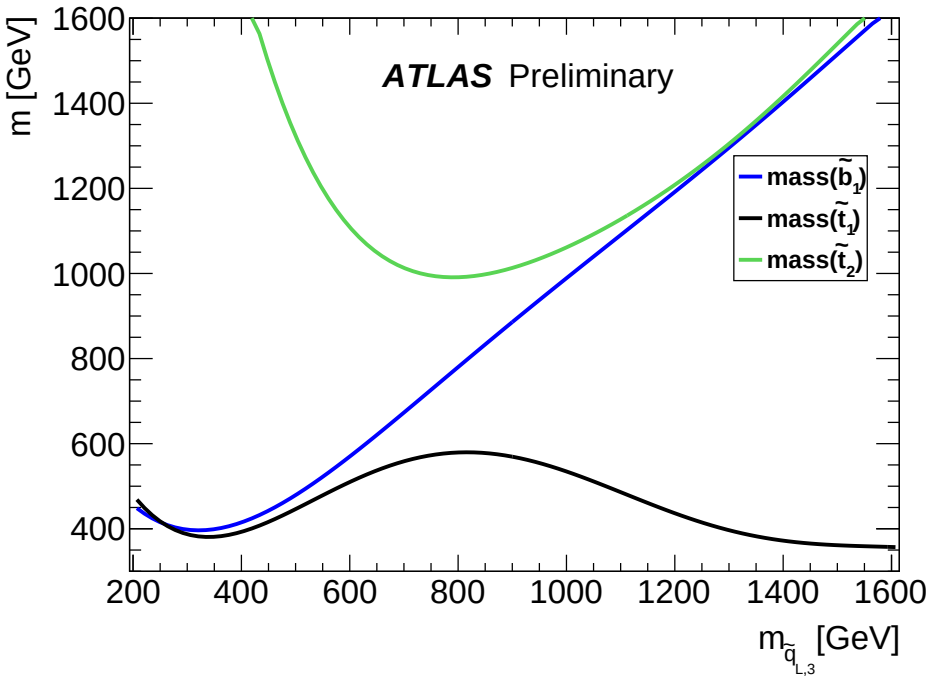

Figure 15: Masses of $\tilde{t}_1$, $\tilde{t}_2$ and $\tilde{b}_1$ as a function of $m_{\tilde{q}_{L,3}}$ in the natural bRPV pMSSM model for a fixed value of $\mu = 560$ GeV.

factorisation and renormalisation scales, as described in Ref. [61]. The detector simulation is the one described in Sect. 3, combining a parametrisation of the calorimeter response [53] and a detailed description based on GEANT4 for the other detector components [54, 55].

4.2. Exploration of the natural pMSSM parameter space

In this section, the characteristics of the two-dimensional $\mu - m_{\tilde{q}_{L,3}}$ parameter space are described in more detail, since this specific model has not been discussed in the literature yet.

The stop and sbottom masses vary as a function of $m_{\tilde{q}_{L,3}}$, and are almost independent of μ. As mentioned above, the right-handed stop mass parameter $m_{\tilde{u}_3}$ is anti-correlated with $m_{\tilde{q}_{L,3}}$. Mixing between the two top squark states means that the mass of the lightest top squarks ($\tilde{t}_1$) never rises above 600 GeV. The mass of the lightest bottom squark ($\tilde{b}_1$) is not limited in this way, because the right-handed sbottom parameter $m_{\tilde{d}_3}$ is set to 3 TeV. This is illustrated in Fig. 15, where the masses of the $\tilde{t}_1$, $\tilde{t}_2$ and $\tilde{b}_1$ particles are shown as a function of $m_{\tilde{q}_{L,3}}$, holding $\mu = 560$ GeV fixed. The upper bound on $m(\tilde{t}_1)$ can be broken by relaxing the assumption of maximal stop mixing, at the cost of additional fine tuning. The masses of the higgsino-like $\tilde{\chi}_1^0$, $\tilde{\chi}_1^\pm$ and $\tilde{\chi}_2^0$ rise monotonically with μ, and for values of μ larger than about 570 GeV the $\tilde{t}_1$ is the LSP. In this case, the phenomenology changes substantially, and the leptoquark-like decay $\tilde{t}_1 \to b\ell$ dominates. This signature is the target of a recent ATLAS search [22], which reports a lower limit on the $\tilde{t}_1$ mass well in excess of 600 GeV for the mixture of decay modes relevant to this model. For this reason, the case of a $\tilde{t}_1$ LSP is not considered further. The parameter space with a neutralino LSP is therefore naturally bounded in μ, and this analysis explores the range $\mu \leq 560$ GeV.

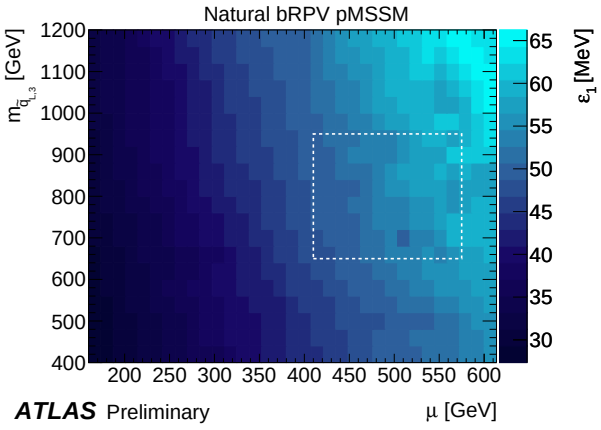

(a) ϵ_1 [MeV]

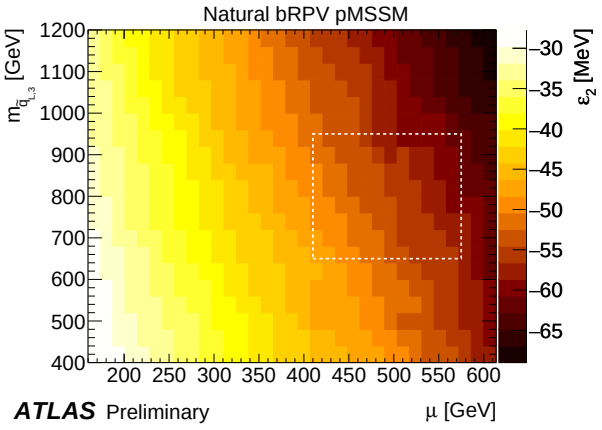

(b) ϵ_2 [MeV]

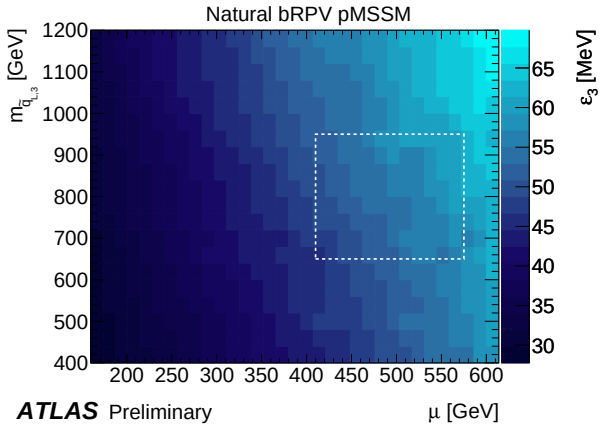

(c) ϵ_3 [MeV]

Figure 16: Bilinear RPV couplings ϵ_i, $i = 1,2,3$, in the natural bRPV pMSSM model. The dashed boxes indicate the primary search region, see Sect. 4.4 for details.

The sparticle decay processes and their relative rates are determined by the bRPV model parameters. The values of the bRPV couplings ϵ_i for the natural bRPV pMSSM model are shown in Fig. 16. They are ultimately determined by mass differences and mixing angles of the neutrino sector and associated relationships between the Higgs field and right-handed sneutrino vacuum expectation values, as investigated in Refs. [24, 70]. The magnitudes of the bRPV couplings under the imposed constraints increase with μ, consistent with the observations of Refs. [69, 70]. They depend relatively weakly on $m_{\tilde{q}_{L,3}}$, which is less closely related to the associated phenomena than μ. The negative sign of ϵ_2 (with respect to ϵ_3) decouples solar and atmospheric neutrino mixing, and allows for a more precise determination of the relationship between the bRPV couplings and the neutrino sector [82]. With this assumption, the values of ϵ_2 and ϵ_3 are related, and forced to take very similar absolute values, by the large value of $\sin^2 2\theta_{23}$, which describes atmospheric neutrino mixing [83]. The size of ϵ_1 is related to ϵ_2, although not in a straightforward manner, by the solar mixing angle θ_{12}.

The branching ratios for the dominant decay modes of the $\tilde{t}_1$ across the $\mu - m_{\tilde{q}_{L,3}}$ plane are shown in Fig. 17. When kinematically accessible, the decay $\tilde{t}_1 \rightarrow t\tilde{\chi}^0_{1,2}$ is typically favoured. At a value of μ

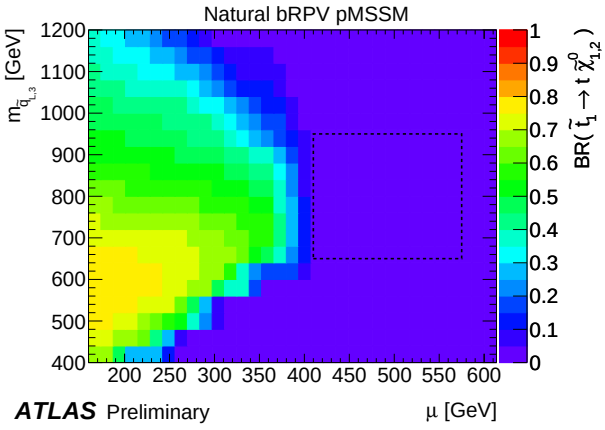

(a) BR($\tilde{t}_1 \to t\tilde{\chi}^0_{1,2}$)

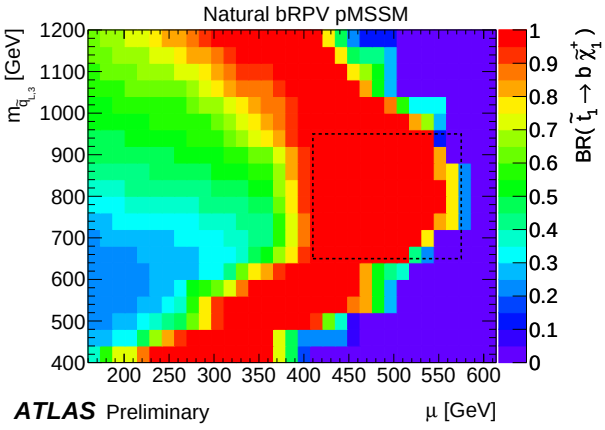

(b) BR($\tilde{t}_1 \to b\tilde{\chi}^+_1$)

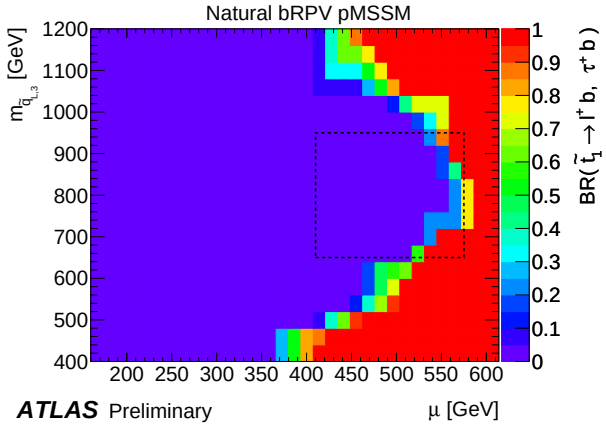

(c) BR($\tilde{t}_1 \to \ell b, \tau b$)

Figure 17: Branching fractions for selected decay modes of $\tilde{t}_1$ in the natural *b*RPV pMSSM model. The dashed boxes indicate the primary search region, see Sect. 4.4 for details.

between above about 200 and 400 GeV (depending on $m_{\tilde{q}_{L,3}}$), this decay channel is no longer kinematically allowed, and the branching ratio for $\tilde{t}_1 \to b\tilde{\chi}^\pm_1$ approaches 100%. Decays to the wino-like $\tilde{\chi}^0_3$ and $\tilde{\chi}^\pm_2$ are negligible, below 2% even for $\mu = 160$ GeV. The boundary at which the $\tilde{t}_1$ becomes the LSP is clearly visible in Fig. 17b, where the branching ratio of $\tilde{t}_1 \to b\tilde{\chi}^\pm_1$ drops abruptly to zero, for μ values between about 400 and 570 GeV (again, depending on $m_{\tilde{q}_{L,3}}$).

Unlike the $\tilde{t}_1$, the $\tilde{b}_1$ mass continues to rise as $m_{\tilde{q}_{L,3}}$ increases. The effect of this can be seen in Fig. 18, which shows branching ratios for the primary decay modes of the $\tilde{b}_1$. Decays to the higgsino-like charginos and neutralinos are favoured for $m_{\tilde{q}_{L,3}} \lesssim 700$ GeV, while decays to the $\tilde{t}_1$ are favoured for larger values of $m_{\tilde{q}_{L,3}}$, although $\tilde{b}_1 \to t\tilde{\chi}^\pm_1$ remains an important decay channel across the entire $m_{\tilde{q}_{L,3}}$ range explored. The decays $\tilde{b}_1 \to b\tilde{\chi}^0_3$ and $\tilde{b}_1 \to t\tilde{\chi}^\pm_2$ (not shown) can have a combined branching ratio of up to $\sim 15\%$ when $\mu = 160$ GeV, but these modes are inaccessible for $\mu \gtrsim 350$ GeV for the range of $m_{\tilde{q}_{L,3}}$ shown in Fig. 18.

The dominant RPV decay modes of the $\tilde{\chi}^0_1$ are shown in Fig. 19. Decays to a charged lepton and a W

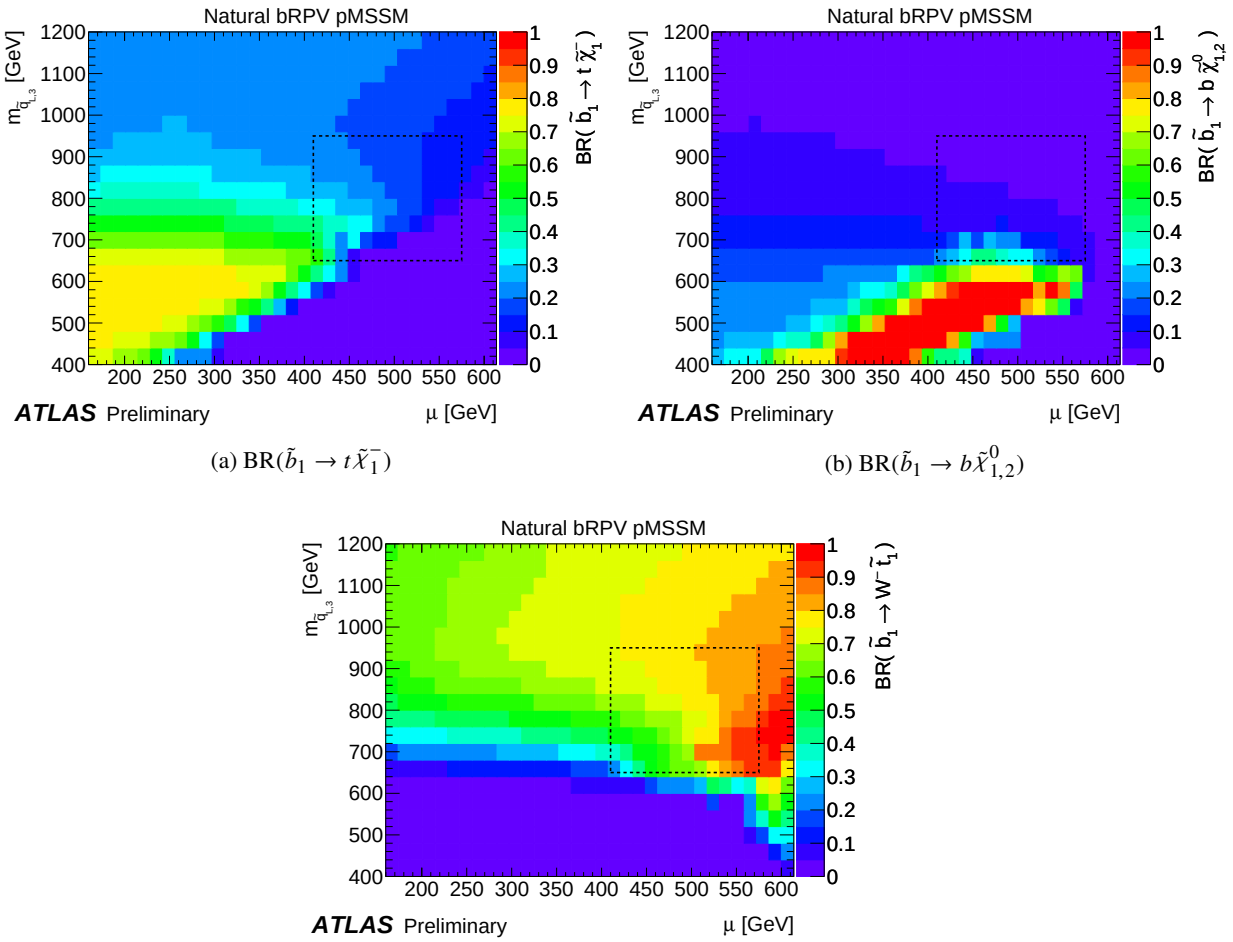

(a) BR($\tilde{b}_1 \to t\tilde{\chi}_1^-$)

(b) BR($\tilde{b}_1 \to b\tilde{\chi}_{1,2}^0$)

(c) BR($\tilde{b}_1 \to W^-\tilde{t}_1$)

Figure 18: Branching fractions for selected decay modes of $\tilde{b}_1$ in the natural *b*RPV pMSSM model. The dashed boxes indicate the primary search region, see Sect. 4.4 for details.

boson dominate across much of the parameter space. At low $m_{\tilde{q}_{L,3}}$ and/or high μ, other decay modes such as ℓtb and $\nu b\bar{b}$ become important as indicated in Figs. 19c and 19d. RPC decay modes of the $\tilde{\chi}_1^0$ dominate at high values of μ where it is no longer the LSP.

As seen above, in many regions of the parameter space, the top and bottom squarks frequently decay to the $\tilde{\chi}_1^\pm$. Branching ratios for the primary decay modes of the $\tilde{\chi}_1^\pm$ are shown in Fig. 20. At very low values of μ, below about 400 GeV, the chargino decays mainly via RPC interactions to the neutralino LSP. For high values of μ, where the $\tilde{t}_1$ is the LSP, the branching ratio for $\tilde{\chi}_1^\pm \to b\tilde{t}_1$ approaches 100%. In between these extremes, the $\tilde{\chi}_1^\pm$ decays via RPV interactions into many different channels.

Of particular interest to this study is the region around $\mu = 550$ GeV and $m_{\tilde{q}_{L,3}} = 800$ GeV, where the $\tilde{t}_1$, $\tilde{\chi}_1^\pm$ and $\tilde{\chi}_1^0$ have similar masses. Here, the $\tilde{t}_1$ decays only to $b\tilde{\chi}_1^\pm$ (see Fig. 17b), and the $\tilde{\chi}_1^\pm$ often produces leptons and *b*-jets but little $E_{\mathrm{T}}^{\mathrm{miss}}$, as BR($\tilde{\chi}_1^\pm \to \ell^\pm b\bar{b}$) reaches as high as 60% (Fig. 20b).

For very small values of μ, the *b*RPV decays of the $\tilde{\chi}_1^0$ may become non-prompt if the decays to W and

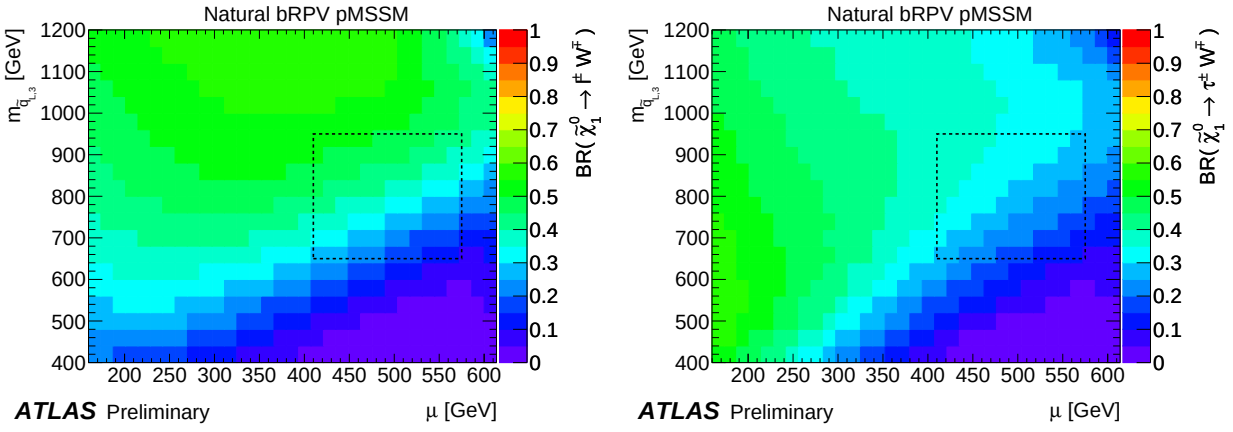

(a) BR($\tilde{\chi}_1^0 \to \ell W$)

(b) BR($\tilde{\chi}_1^0 \to \tau W$)

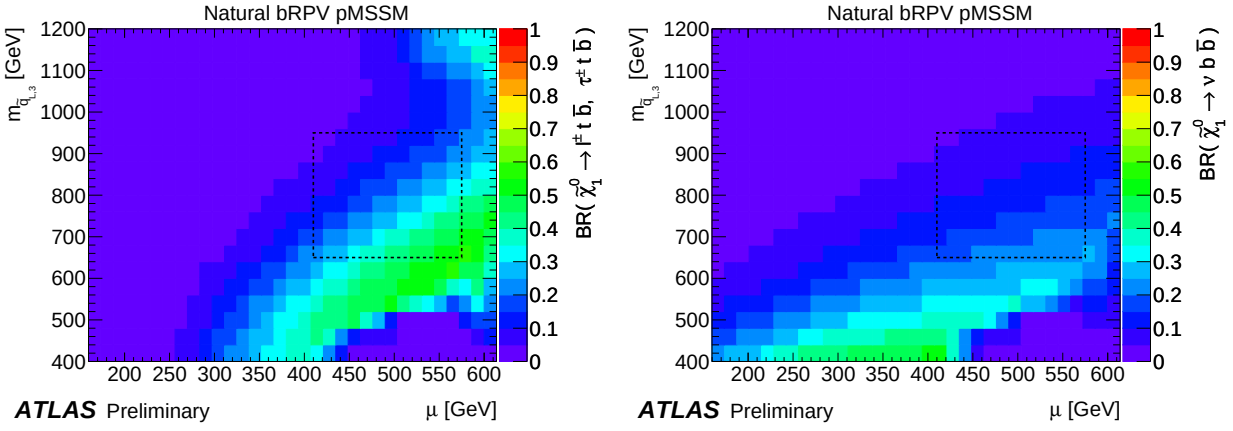

(c) BR($\tilde{\chi}_1^0 \to \ell tb, \tau tb$)

(d) BR($\tilde{\chi}_1^0 \to \nu bb$)

Figure 19: Branching fractions for selected decay modes of $\tilde{\chi}_1^0$ in the natural bRPV pMSSM model. The dashed boxes indicate the primary search region, see Sect. 4.4 for details.

Z bosons become kinematically suppressed. Values of μ as low as $\mu = 160$ GeV have been explored, at which value the proper decay length of the LSP is 0.2–0.4 mm and of the same order as typical impact parameter requirements placed on light leptons reconstructed in ATLAS. The efficiency of such requirements is expected to degrade rapidly for lower values of μ.

4.3. Analysis strategy

Search channels requiring at least one lepton are used to constrain the natural bRPV model just described. The lepton requirement is motivated by the high branching ratios of the $\tilde{\chi}_1^0$ and $\tilde{\chi}_1^\pm$ to leptons, together with the possibility of additional leptons from RPC SUSY cascades.

The ATLAS 1L search of Ref [41], described above in section 2.3, was, however found to be insensitive to this pMSSM model, despite setting strong constraints (equivalent to $m(\tilde{g}) > 1$ TeV) in the mSUGRA

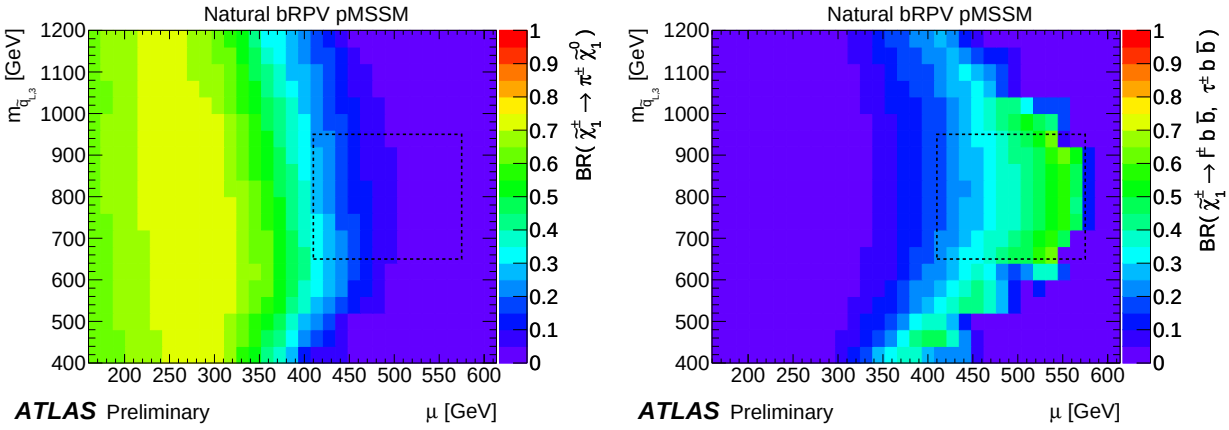

(a) BR($\tilde{\chi}_1^\pm \to \pi^\pm \tilde{\chi}_1^0$)

(b) BR($\tilde{\chi}_1^\pm \to \ell bb, \tau bb$)

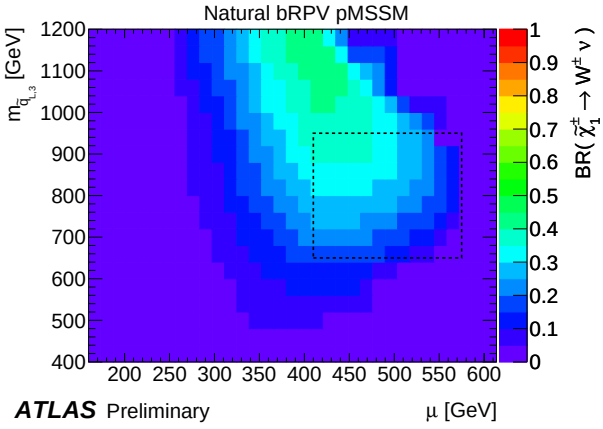

(c) BR($\tilde{\chi}_1^\pm \to \nu W^\pm$)

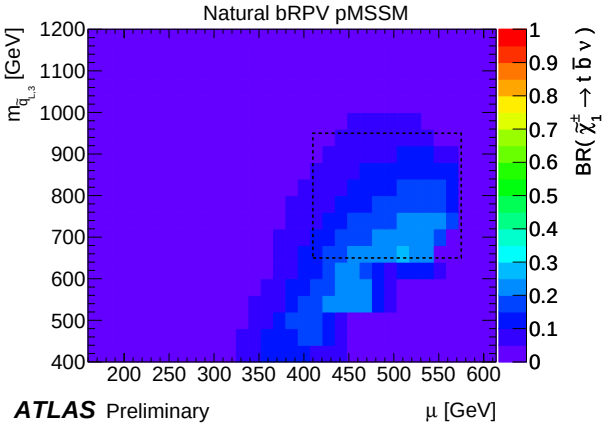

(d) BR($\tilde{\chi}_1^\pm \to tb\nu$)

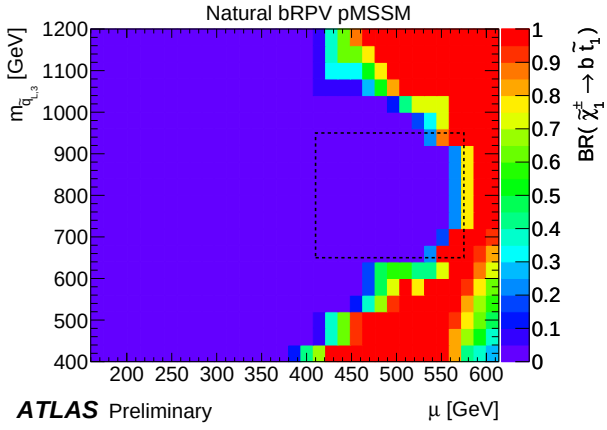

(e) BR($\tilde{\chi}_1^\pm \to b\tilde{l}_1$)

Figure 20: Branching fractions for selected decay modes of $\tilde{\chi}_1^\pm$ in the natural *b*RPV pMSSM model. The dashed boxes indicate the primary search region, see Sect. 4.4 for details.

model space. In the pMSSM case it was found that the production cross-section for higgsinos and third-generation squarks is too small to produce sufficient events above the required $E_{\mathrm{T}}^{\mathrm{miss}}$ thresholds of 250–300 GeV (see Table 4).

The SS/3L search [40] sets limits on the mSUGRA bRPV model comparable to the 1L analysis, excluding gluino masses below 1.2 TeV. This sensitivity is possible because the neutralino LSP is a Majorana particle. The lepton charges are uncorrelated if both LSPs decay leptonically, and therefore events with same-sign leptons are common. SR3b of this analysis was found to be the most sensitive signal region to the mSUGRA bRPV model (see Table 3), as the LSP decays are rich in b-jets.

4.4. Simulated model points

As discussed in section 4.3, this natural pMSSM model with bilinear R-parity violation has a complex phenomenology. For this initial exploration, we focus primarily on the region $650 < m_{\tilde{q}_{\mathrm{L},3}} < 950$ GeV, where the $\tilde{t}_1$ takes the largest mass available within the context of the maximally natural pMSSM scenario ($550 \lesssim m(\tilde{t}_1) \lesssim 580$ GeV, with some dependence on μ). This gives the maximum possible mass difference between the $\tilde{t}_1$ and the LSP, for any given μ. For values of $m_{\tilde{q}_{\mathrm{L},3}}$ outside of this range, the spectrum is more compressed, which reduces the momentum of particles from the $\tilde{t}_1$ and $\tilde{b}_1$ decays and increases the likelihood of signal contaminating the validation regions of the SS/3L analysis, as discussed below. In other words, the search was not designed with these scenarios in mind, and it is likely that a more targeted search would be needed to properly explore the full parameter space. Furthermore, we require that the decay $\tilde{b}_1 \rightarrow t\tilde{\chi}_1^-$ is kinematically accessible. This avoids discontinuities in the sparticle decay patterns over the scanned parameter space (c.f. Fig. 18a), and allows this initial investigation to be performed with a relatively sparse array of model points. The points in the parameter space that were simulated are shown in Table 8 in App. D, which includes a few test points outside the primary $m_{\tilde{q}_{\mathrm{L},3}}$ range.

As with the simplified models, the potential contamination of control and validation regions with the bRPV SUSY signal was investigated. Some contamination in the validation regions of the SS/3L analysis is seen for $\mu \lesssim 310$ GeV, especially when $m_{\tilde{q}_{\mathrm{L},3}} < 650$ GeV. The most significant contamination occurs for the selection designed to test the $t\bar{t}\,W$ background estimate, which has few events and tests a process with similar characteristics to a SUSY signal. For example, with $\mu = 310$ GeV and $m_{\tilde{q}_{\mathrm{L},3}} = 450$ GeV, 6.2 events are expected in the $t\bar{t}\,W$ validation region from signal processes, compared with nine observed in data (the SM background prediction was 5.8 ± 2.5 events). The contamination is smaller within the primary $m_{\tilde{q}_{\mathrm{L},3}}$ range, becoming negligible near the exclusion limit. Theoretical uncertainties on the signal acceptance (described in Sect. 3.2) were also investigated but found to be negligible with respect to other experimental uncertainties. They are not included in the results presented here.

4.5. Results

The 95% CL lower limits obtained on the μ and $m_{\tilde{q}_{\mathrm{L},3}}$ parameters in natural SUSY with bRPV are shown in Fig. 21.

The region below and to the left of the solid line - almost all of the allowed region explored - is excluded, with lower limits of $\mu > 455$ GeV and $m_{\tilde{q}_{\mathrm{L},3}} > 810$ GeV within that region. All model points listed in Table 8 but outside the plotted range of Fig. 21 were also excluded. The SR3b signal region of the SS/3L search dominates over the entire plane, although the expected exclusion reach is slightly extended by the inclusion of SR1b. This result is illustrated in App. D, where limits for individual signal regions of the

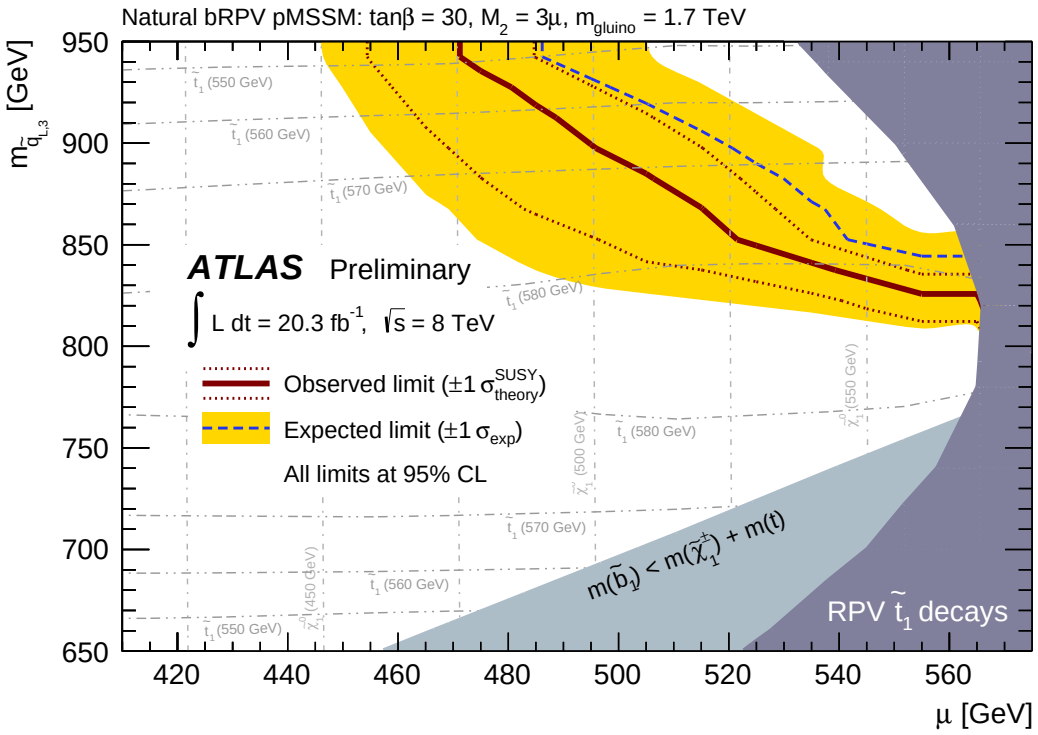

Figure 21: Observed (solid) and expected (dashed) 95% CL exclusion limit contours for the natural *b*RPV model, obtained using the SS/3L analysis [40]. The region below and to the left of the solid line is excluded. The shaded band around the expected limit shows the effect of varying the experimental systematic uncertainties by $\pm 1\sigma$, while the dotted lines either side of the observed limit show the effect of the theoretical cross-section uncertainty. The other shaded areas at high μ are not explored in this analysis, see text for details.

SS/3L analysis are shown. For $m_{\tilde{q}_{\mathrm{L},3}} = 800$ GeV, the entire range of μ is excluded, up to where the $\tilde{t}_1$ becomes the LSP. This limit weakens as $m_{\tilde{q}_{\mathrm{L},3}}$ increases, primarily due to the increasing $\tilde{b}_1$ mass, and the corresponding decrease in the $\tilde{b}_1\tilde{b}_1$ production cross-section. SR1b and, to a lesser extent, SR3b, require events with large m_{eff}, which is difficult to produce from $\tilde{t}_1$ decays when the $\tilde{t}_1$ and $\tilde{\chi}_1^{\pm}$ are nearly degenerate, as they are in this region. Thus, the contribution from $\tilde{b}_1$ pair production is critical to producing a strong limit in this case.

5. Conclusions

Despite a wide and varied collection of searches for weak-scale supersymmetry at the LHC, it is difficult to ensure with complete confidence that all plausible scenarios would be discovered. One possible cause of non-discovery is *R*-parity violation, in which case the LSP, usually assumed to be stable, decays. In this note, a variety of RPV scenarios are systematically explored and tested against previously published searches performed by the ATLAS collaboration. The resulting constraints are generally strong, and the features that make particular search channels successful or unsuccessful in these scenarios are discussed.

In the case of RPV decays mediated by the superpotential terms $\frac{1}{2}\lambda_{ijk}L_iL_j\bar{E}_k$ and $\lambda'_{ijk}L_iQ_j\bar{D}_k$, sim-

plified models of squark and gluino pair production are considered, with a neutralino LSP. Limits on the production cross-section and sparticle masses are obtained for different LSP mass hypotheses as a function of the LSP branching fraction to bottom quarks and tau leptons. This parametrisation is more convenient than using the RPV couplings directly, as the branching fractions are more experimentally accessible and their relationship to the couplings is model-dependent. For simplicity, models with simultaneous $LL\bar{E}$- and $LQ\bar{D}$-mediated decays were not considered, but the approach used could be extended to this case.

In the case of $LL\bar{E}$ RPV, previously published results are strengthened by the inclusion of a search for events with two or three light leptons in association with jets. A lower 95% CL bound is set on the gluino mass of 1040 GeV in the worst case considered, an improvement of about 100 GeV over previous ATLAS results. For $LQ\bar{D}$ RPV with gluino production, analysis channels requiring zero or one light lepton set lower limits on the gluino mass between about 910 and about 1220 GeV. The production of first- and second-generation squarks is also examined, with non-zero $LQ\bar{D}$ RPV couplings. If the LSP is light, with $m(\tilde{\chi}_1^0)/m(\tilde{q}) = 0.1$, no limit can be set by these searches on the squark mass. In cases with larger values of $m(\tilde{\chi}_1^0)/m(\tilde{q})$, squark masses below about 910 GeV are excluded, under the assumption that all first- and second-generation squarks are degenerate.

Bilinear R-parity violation is investigated in the context of a natural pMSSM model, where only third-generation squarks and higgsino-like particles are assumed to be relevant for LHC phenomenology. A restricted region of the available subspace is explored for this initial investigation, where the $\tilde{t}_1$ has a mass of about 550–580 GeV, and the higgsino-like $\tilde{\chi}_1^0$ is the LSP. Within these constraints, values of μ between 160 and 455 GeV are excluded at 95% CL. When $m_{\tilde{q}_{L,3}} = 800$ GeV, the model is excluded up to $\mu = 560$ GeV, where the $\tilde{t}_1$ can no longer decay via RPC interactions. These strong limits in a model of natural supersymmetry with bilinear R-parity violation and maximal stop mixing complement previous studies of an mSUGRA model dominated by squark and gluino production.

Between this study and other published results, the ATLAS collaboration has constrained significant portions of the TeV-scale parameter space of R-parity-violating supersymmetry. The systematic approach to constraining RPV signatures used here can also be used to inform and improve future searches for supersymmetry at the LHC. In particular, it is shown that inclusive searches, mostly optimised for RPC scenarios with squark and gluino production, can also have excellent sensitivity to supersymmetry with R-parity violation. Even with their wide range of applicability, gaps in their coverage have been found. Most notable is the case, mentioned above, of a light LSP decaying via $LQ\bar{D}$ interactions when the gluino is decoupled, where the reduced missing transverse momentum compared to the analogous RPC model makes current searches insensitive. The case of natural supersymmetry with bilinear R-parity violation and a compressed mass spectrum also presents a challenge to existing searches due to the relatively low momenta of the produced Standard Model particles. A broader consideration of R-parity violating models, uncovering challenging scenarios such as these, can help to improve the design of future searches for supersymmetry, and enhance their discovery potential in the upcoming $\sqrt{s} = 13$ TeV run of the LHC.

References

[1] ATLAS Collaboration, *The ATLAS experiment at the CERN Large Hadron Collider*, JINST **3** (2008) S08003.

[2] H. Miyazawa, *Baryon number changing currents*, Prog. Theor. Phys. **36 (6)** (1966) 1266–1276.

[3] P. Ramond, *Dual theory for free fermions*, Phys. Rev. D **3** (1971) 2415–2418.

[4] Y. A. Gol'fand and E. P. Likhtman, *Extension of the algebra of poincare group generators and violation of p invariance*, JETP Lett. **13** (1971) 323–326, [Pisma Zh.Eksp.Teor.Fiz.13:452-455,1971].

[5] A. Neveu and J. H. Schwarz, *Factorizable dual model of pions*, Nucl. Phys. B **31** (1971) 86–112.

[6] A. Neveu and J. H. Schwarz, *Quark model of dual pions*, Phys. Rev. D **4** (1971) 1109–1111.

[7] J. Gervais and B. Sakita, *Field theory interpretation of supergauges in dual models*, Nucl. Phys. B **34** (1971) 632–639.

[8] D. V. Volkov and V. P. Akulov, *Is the neutrino a Goldstone particle?*, Phys. Lett. B **46** (1973) 109–110.

[9] J. Wess and B. Zumino, *A Lagrangian model invariant under supergauge transformations*, Phys. Lett. B **49** (1974) 52–54.

[10] J. Wess and B. Zumino, *Supergauge transformations in four dimensions*, Nucl. Phys. B **70** (1974) 39–50.

[11] P. Fayet, *Supersymmetry and weak, electromagnetic and strong interactions*, Phys. Lett. B **64** (1976) 159–162.

[12] P. Fayet, *Spontaneously broken supersymmetric theories of weak, electromagnetic and strong interactions*, Phys. Lett. B **69** (1977) 489–494.

[13] G. R. Farrar and P. Fayet, *Phenomenology of the production, decay, and detection of new hadronic states associated with supersymmetry*, Phys. Lett. B **76** (1978) 575–579.

[14] P. Fayet, *Relations between the masses of the superpartners of leptons and quarks, the goldstino couplings and the neutral currents*, Phys. Lett. B **84** (1979) 416–420.

[15] S. Dimopoulos and H. Georgi, *Softly broken supersymmetry and SU(5)*, Nucl. Phys. B **193** (1981) 150–162.

[16] R. N. Mohapatra, *Supersymmetry and R-parity: An overview*, 2015, arXiv: 1503.06478 [hep-ph].

[17] B. Allanach and B. Gripaios, *Hide and seek with natural supersymmetry at the LHC*, J. High Energy Phys. **05** (2012) 062, arXiv: 1202.6616 [hep-ph].

[18] M. Asano, K. Rolbiecki and K. Sakurai, *Can R-parity violation hide vanilla supersymmetry at the LHC?*, J. High Energy Phys. **01** (2013) 128, arXiv: 1209.5778 [hep-ph].

[19] H. Dreiner and G. G. Ross, *R-parity violation at hadron colliders*, Nucl. Phys. B **365** (1991) 597–613.

[20] H. Dreiner et al., *General MSSM signatures at the LHC with and without R-parity*, Phys. Rev. D **86** (2012) 035021, arXiv: 1205.0557 [hep-ph].

[21] ATLAS Collaboration, *Limits on metastable gluinos from ATLAS SUSY searches at 8 TeV*, ATL-CONF-2014-037, 2014, URL: http://cds.cern.ch/record/1735199.

[22] ATLAS Collaboration, *A search for $B - L$ R-Parity violating scalar top decays in $\sqrt{s} = 8$ TeV pp collisions with the ATLAS experiment*, ATLAS-CONF-2015-015, 2015, URL: http://cds.cern.ch/record/2002885.

[23] ATLAS Collaboration, *Search for massive supersymmetric particles decaying to many jets using the ATLAS detector in pp collisions at $\sqrt{s} = 8$ TeV*, submitted to Phys. Rev. D (2015), arXiv: 1502.05686 [hep-ex].

[24] J. Romão et al., *A supersymmetric solution to the solar and atmospheric neutrino problems*, Phys. Rev. D **61** (2000) 071703, arXiv: hep-ph/9907499.

[25] A. Djouadi et al., *The minimal supersymmetric standard model: Group summary report* (1998), arXiv: hep-ph/9901246.

[26] CMS Collaboration, *The CMS experiment at the CERN LHC*, JINST **3** (2008) S08004.

[27] ATLAS Collaboration, *Search for supersymmetry in events with four or more leptons in $\sqrt{s} = 8$ TeV pp collisions with the ATLAS detector*, Phys. Rev. D **90**.5 (2014) 052001, arXiv: 1405.5086 [hep-ex].

[28] ATLAS Collaboration, *Search for massive, long-lived particles using multitrack displaced vertices or displaced lepton pairs in pp collisions at $\sqrt{s} = 8$ TeV with the ATLAS detector*, submitted to Phys. Rev. D (2015), arXiv: 1504.05162 [hep-ex].

[29] CMS Collaboration, *Search for anomalous production of multilepton events in pp collisions at $\sqrt{s} = 7$ TeV*, J. High Energy Phys. **06** (2012) 169, arXiv: 1204.5341 [hep-ex].

[30] CMS Collaboration, *Search for RPV SUSY in the four-lepton final state*, CMS-PAS-SUS-13-010, 2013, URL: http://cds.cern.ch/record/1550552.

[31] CMS Collaboration, *Search for long-lived particles that decay into final states containing two electrons or two muons in proton-proton collisions at $\sqrt{s} = 8$ TeV*, Phys. Rev. D **91**.5 (2015) 052012, arXiv: 1411.6977 [hep-ex].

[32] CMS Collaboration, *Search for top squarks in R-parity-violating supersymmetry using three or more leptons and b-tagged jets*, Phys. Rev. Lett. **111** (2013) 221801, arXiv: 1306.6643 [hep-ex].

[33] CMS Collaboration, *Search for RPV supersymmetry with three or more leptons and b-tags*, CMS-PAS-SUS-12-027, 2012, URL: http://cdsweb.cern.ch/record/1494689.

[34] D0 Collaboration, V. Abazov et al., *Search for R-parity violating supersymmetry via the $LL\bar{E}$ couplings λ_{121}, λ_{122} or λ_{133} in $p\bar{p}$ collisions at $\sqrt{s} = 1.96$ TeV*, Phys. Lett. B **638** (2006) 441–449, arXiv: hep-ex/0605005.

[35] CDF Collaboration, A Abulencia et al., *Search for anomalous production of multi-lepton events in $p\bar{p}$ collisions at $\sqrt{s} = 1.96$ TeV*, Phys. Rev. Lett. **98** (2007) 131804, arXiv: 0706.4448 [hep-ex].

[36] DELPHI Collaboration, J. Abdallah et al., *Search for supersymmetric particles assuming R-parity nonconservation in e^+e^- collisions at $\sqrt{s} = 192$ GeV to 208 GeV*, Eur. Phys. J. C **36** (2004) 1–23, arXiv: hep-ex/0406009.

[37] L3 Collaboration, P. Achard et al.,
Search for R parity violating decays of supersymmetric particles in e^+e^- collisions at LEP, Phys. Lett. B **524** (2002) 65–80, arXiv: hep-ex/0110057.

[38] CMS Collaboration, *Search for Displaced Supersymmetry in events with an electron and a muon with large impact parameters*, Phys. Rev. Lett. **114**.6 (2015) 061801, arXiv: 1409.4789 [hep-ex].

[39] CMS Collaboration, *Search for pair production of third-generation scalar leptoquarks and top squarks in proton-proton collisions at $\sqrt{s} = 8$ TeV*, Phys. Lett. B **739** (2014) 229, arXiv: 1408.0806 [hep-ex].

[40] ATLAS Collaboration, *Search for supersymmetry at $\sqrt{s} = 8$ TeV in final states with jets and two same-sign leptons or three leptons with the ATLAS detector*, J. High Energy Phys. **06** (2014) 035, arXiv: 1404.2500 [hep-ex].

[41] ATLAS Collaboration, *Search for squarks and gluinos in events with isolated leptons, jets and missing transverse momentum at $\sqrt{s} = 8$ TeV with the ATLAS detector*, accepted by J. High Energy Phys. (2015), arXiv: 1501.03555 [hep-ex].

[42] ATLAS Collaboration,
Search for supersymmetry in events with large missing transverse momentum, jets, and at least one tau lepton in 20 fb^{-1} of $\sqrt{s} = 8$ TeV proton-proton collision data with the ATLAS detector, J. High Energy Phys. **09** (2014) 103, arXiv: 1407.0603 [hep-ex].

[43] ATLAS Collaboration, *Search for a heavy neutral particle decaying to $e\mu$, $e\tau$, or $\mu\tau$ in pp collisions at $\sqrt{s} = 8$ TeV with the ATLAS detector*, submitted to Phys. Rev. Lett. (2015), arXiv: 1503.04430 [hep-ex].

[44] CMS Collaboration, *Search for lepton flavour violating decays of heavy resonances and quantum black holes to electron/muon pairs in pp collisions at a centre of mass energy of 8 TeV*, CMS-PAS-EXO-13-002, 2015, URL: http://cds.cern.ch/record/2002203.

[45] CDF Collaboration, T. Aaltonen et al., *Search for R-parity violating decays of τ sneutrinos to $e\mu$, $\mu\tau$, and $e\tau$ pairs in $p\bar{p}$ collisions at $\sqrt{s} = 1.96$ TeV*, Phys. Rev. Lett. **105** (2010) 191801, arXiv: 1004.3042 [hep-ex].

[46] D0 Collaboration, V. M. Abazov et al.,
Search for sneutrino production in $e\mu$ final states in 5.3 fb^{-1} of $p\bar{p}$ collisions at $\sqrt{s} = 1.96$ TeV, Phys. Rev. Lett. **105** (2010) 191802, arXiv: 1007.4835 [hep-ex].

[47] CMS Collaboration, *Search for RPV SUSY resonant second generation slepton production in same-sign dimuon events at $\sqrt{s} = 7$ TeV*, CMS-PAS-SUS-13-005, 2013, URL: http://cds.cern.ch/record/1547780.

[48] ATLAS Collaboration, *Search for squarks and gluinos with the ATLAS detector in final states with jets and missing transverse momentum using $\sqrt{s} = 8$ TeV proton–proton collision data*, J. High Energy Phys. **09** (2014) 176, arXiv: 1405.7875 [hep-ex].

[49] ATLAS Collaboration,
Search for new phenomena in final states with large jet multiplicities and missing transverse momentum at $\sqrt{s} = 8$ TeV proton-proton collisions using the ATLAS experiment, J. High Energy Phys. **10** (2013) 130, arXiv: 1308.1841 [hep-ex].

[50] M. Bähr et al., *Herwig++ physics and manual*, Eur. Phys. J. C **58** (2008) 639–707, arXiv: 0803.0883 [hep-ph].

[51] J. Pumplin et al.,
New generation of parton distributions with uncertainties from global QCD analysis,
J. High Energy Phys. **07** (2002) 012, arXiv: hep-ph/0201195.

[52] S. Gieseke and A. Rohr, *Colour reconnections in Herwig++*, Eur. Phys. J. C **72** (2012) 2225,
arXiv: 1206.0041 [hep-ph].

[53] ATLAS Collaboration,
The simulation principle and performance of the ATLAS fast calorimeter simulation FastCaloSim,
ATL-PHYS-PUB-2010-013, 2010, URL: http://cds.cern.ch/record/1300517.

[54] GEANT4 Collaboration, S. Agostinelli et al., *GEANT4: A simulation toolkit*,
Nucl. Instrum. Meth. **506** (2003) 250–303.

[55] ATLAS Collaboration, *The ATLAS Simulation Infrastructure*, Eur. Phys. J. C **70** (2010) 823–874,
arXiv: 1005.4568 [physics.ins-det].

[56] W. Beenakker et al., *Squark and gluino production at hadron colliders*,
Nucl. Phys. B **492** (1997) 51–103, arXiv: hep-ph/9610490.

[57] A. Kulesza and L. Motyka,
Threshold resummation for squark-antisquark and gluino-pair production at the LHC,
Phys. Rev. Lett. **102** (2009) 111802, arXiv: 0807.2405 [hep-ph].

[58] A. Kulesza and L. Motyka, *Soft gluon resummation for the production of gluino-gluino and squark-antisquark pairs at the LHC*, Phys. Rev. D **80** (2009) 095004,
arXiv: 0905.4749 [hep-ph].

[59] W. Beenakker et al., *Soft-gluon resummation for squark and gluino hadroproduction*,
J. High Energy Phys. **12** (2009) 041, arXiv: 0909.4418 [hep-ph].

[60] W. Beenakker et al., *Squark and gluino hadroproduction*,
Int. J. Mod. Phys.A **26** (2011) 2637–2664, arXiv: 1105.1110 [hep-ph].

[61] M. Krämer et al., *Supersymmetry production cross sections in pp collisions at* $\sqrt{s} = 7$ *TeV* (2012),
arXiv: 1206.2892 [hep-ph].

[62] C. Brust et al., *Identifying boosted new physics with non-isolated leptons* (2014),
arXiv: 1410.0362 [hep-ph].

[63] J. Alwall et al., *MadGraph 5: Going beyond*, J. High Energy Phys. **06** (2011) 128,
arXiv: 1106.0522 [hep-ph].

[64] T. Sjöstrand, S. Mrenna and P. Z. Skands, *PYTHIA 6.4 physics and manual*,
J. High Energy Phys. **05** (2006) 026, arXiv: hep-ph/0603175.

[65] ATLAS Collaboration, *Search for direct top-squark pair production in final states with two leptons in pp collisions at* $\sqrt{s} = 8$ *TeV with the ATLAS detector*,
J. High Energy Phys. **06** (2014) 124, arXiv: 1403.4853 [hep-ex].

[66] M. Papucci, J. T. Ruderman and A. Weiler, *Natural SUSY endures*,
J. High Energy Phys. **09** (2012) 035, arXiv: 1110.6926 [hep-ph].

[67] R. Barbieri and G. Giudice, *Upper bounds on supersymmetric particle masses*,
Nucl. Phys. B **306** (1988) 63.

[68] B. de Carlos and J. Casas, *One loop analysis of the electroweak breaking in supersymmetric models and the fine tuning problem*, Phys. Lett. B **309** (1993) 320–328, arXiv: hep-ph/9303291.

[69] M. Diaz et al., *Solar neutrino masses and mixing from bilinear R parity broken supersymmetry: Analytical versus numerical results*, Phys. Rev. D **68** (2003) 013009, arXiv: hep-ph/0302021.

[70] W. Porod et al., *Testing neutrino mixing at future collider experiments*, Phys. Rev. D **63** (2001) 115004, arXiv: hep-ph/0011248.

[71] W. Porod, *SPheno, a program for calculating supersymmetric spectra, SUSY particle decays and SUSY particle production at e^+e^- colliders*, Comp. Phys. Comm. **153** (2003) 275–315, arXiv: hep-ph/0301101.

[72] W. Porod and F. Staub, *SPheno 3.1: Extensions including flavour, CP-phases and models beyond the MSSM*, Comp. Phys. Comm. **183** (2012) 2458–2469, arXiv: 1104.1573 [hep-ph].

[73] M. Hirsch and W. Porod, *Neutrino properties and the decay of the lightest supersymmetric particle*, Phys. Rev. D **68** (2003) 115007, arXiv: hep-ph/0307364.

[74] L. J. Hall, D. Pinner and J. T. Ruderman, *A natural SUSY Higgs near 126 GeV*, J. High Energy Phys. **04** (2012) 131, arXiv: 1112.2703 [hep-ph].

[75] H. Baer et al., *Radiative natural SUSY with a 125 GeV Higgs boson*, Phys. Rev. Lett. **109** (2012) 161802, arXiv: 1207.3343 [hep-ph].

[76] A. Delgado et al., *The light stop window*, Eur. Phys. J. C **73**.3 (2013) 2370, arXiv: 1212.6847 [hep-ph].

[77] A. Djouadi, *Implications of the Higgs discovery for the MSSM*, Eur. Phys. J. C **74** (2014) 2704, arXiv: 1311.0720 [hep-ph].

[78] W. Beenakker et al., *Stop production at hadron colliders*, Nucl. Phys. B **515** (1998) 3–14, arXiv: hep-ph/9710451.

[79] W. Beenakker et al., *Supersymmetric top and bottom squark production at hadron colliders*, J. High Energy Phys. **08** (2010) 098, arXiv: 1006.4771 [hep-ph].

[80] B. Fuks et al., *Gaugino production in proton-proton collisions at a center-of-mass energy of 8 TeV*, J. High Energy Phys. **10** (2012) 081, arXiv: 1207.2159 [hep-ph].

[81] B. Fuks et al., *Precision predictions for electroweak superpartner production at hadron colliders with Resummino*, Eur. Phys. J. C **73** (2013) 2480, arXiv: 1304.0790 [hep-ph].

[82] M. Hirsch et al., *Neutrino masses and mixings from supersymmetry with bilinear R-parity violation: A theory for solar and atmospheric neutrino oscillations*, Phys. Rev. D **62** (2000) 113008, Erratum: ibid. D65:119901 (2002), arXiv: hep-ph/0004115.

[83] T2K Collaboration, K. Abe et al., *Precise measurement of the neutrino mixing parameter θ_{23} from muon neutrino disappearance in an off-axis beam*, Phys. Rev. Lett. **112**.18 (2014) 181801, arXiv: 1403.1532 [hep-ex].

A. Further results relating to the combined $LL\bar{E}$ model results

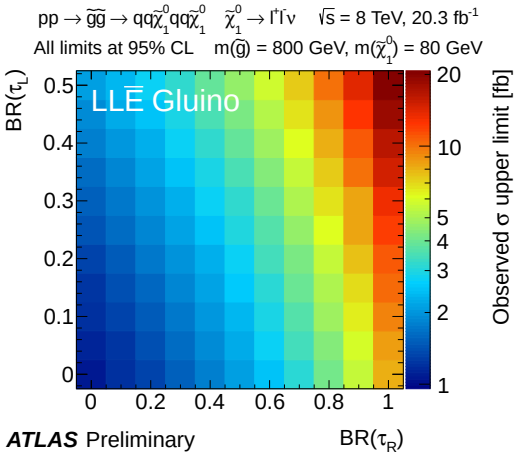

(a) Observed, $m(\tilde{g}) = 800$ GeV, $m(\tilde{\chi}_1^0) = 80$ GeV

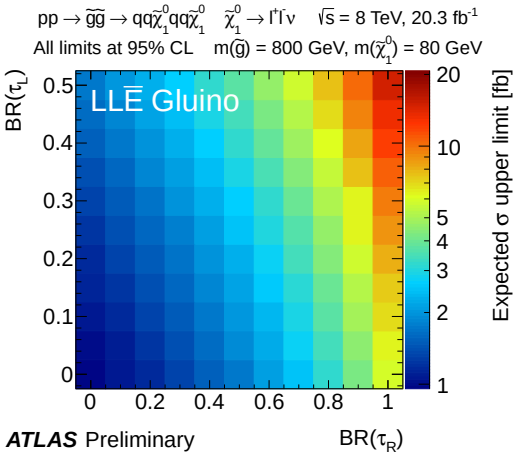

(b) Expected, $m(\tilde{g}) = 800$ GeV, $m(\tilde{\chi}_1^0) = 80$ GeV

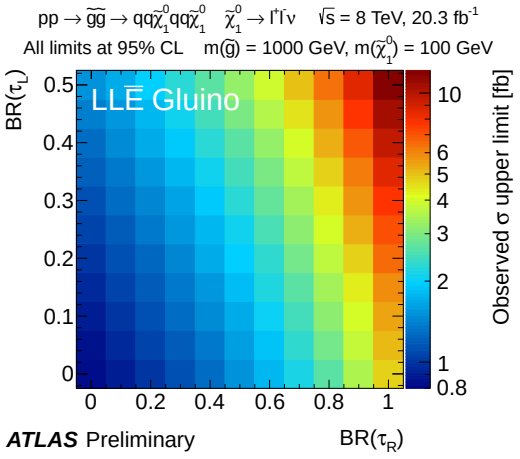

(c) Observed, $m(\tilde{g}) = 1000$ GeV, $m(\tilde{\chi}_1^0) = 100$ GeV

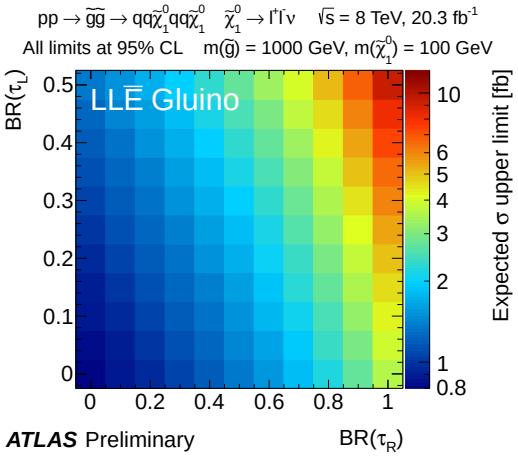

(d) Expected, $m(\tilde{g}) = 1000$ GeV, $m(\tilde{\chi}_1^0) = 100$ GeV

Figure 22: Observed and expected 95% CL upper cross-section limits for the $LL\bar{E}$ model points with $R = 0.1$ and $m(\tilde{g}) \leq 1000$ GeV. In all cases the constraints are taken from the SS/3L analysis.

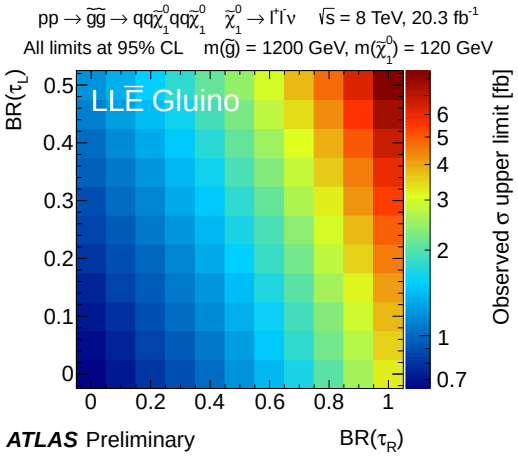

(a) Observed, $m(\tilde{g}) = 1200$ GeV, $m(\tilde{\chi}_1^0) = 120$ GeV

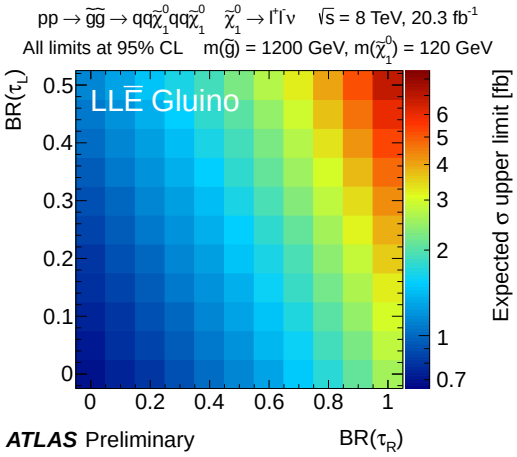

(b) Expected, $m(\tilde{g}) = 1200$ GeV, $m(\tilde{\chi}_1^0) = 120$ GeV

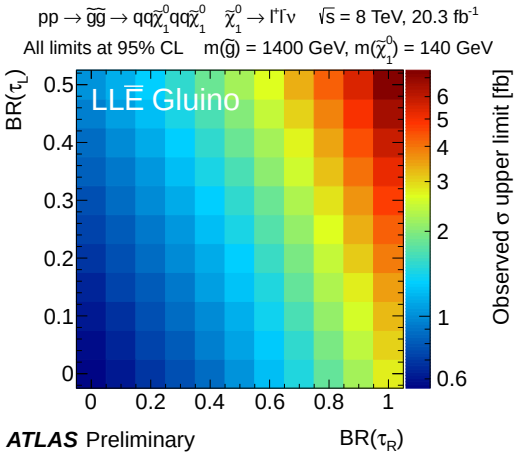

(c) Observed, $m(\tilde{g}) = 1400$ GeV, $m(\tilde{\chi}_1^0) = 140$ GeV

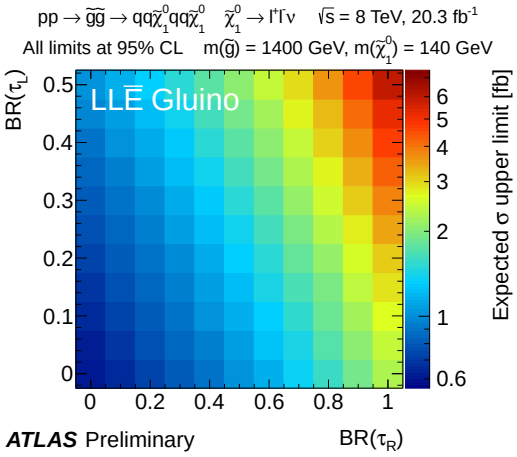

(d) Expected, $m(\tilde{g}) = 1400$ GeV, $m(\tilde{\chi}_1^0) = 140$ GeV

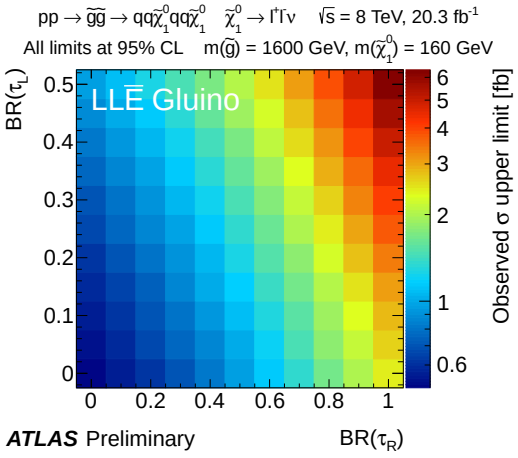

(e) Observed, $m(\tilde{g}) = 1600$ GeV, $m(\tilde{\chi}_1^0) = 160$ GeV

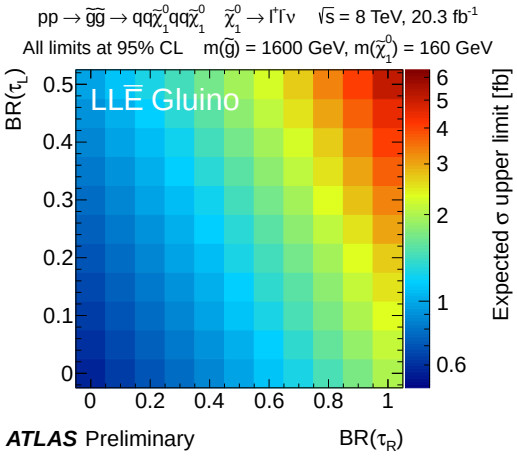

(f) Expected, $m(\tilde{g}) = 1600$ GeV, $m(\tilde{\chi}_1^0) = 160$ GeV

Figure 23: Observed and expected 95% CL upper cross-section limits for the $LL\bar{E}$ model points with $R = 0.1$ and $m(\tilde{g}) \geq 1200$ GeV. In all cases the constraints are taken from the SS/3L analysis.

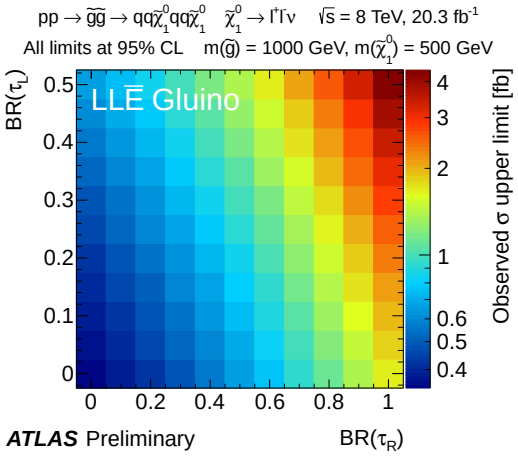

(a) Observed, $m(\tilde{g}) = 1000$ GeV, $m(\tilde{\chi}_1^0) = 500$ GeV

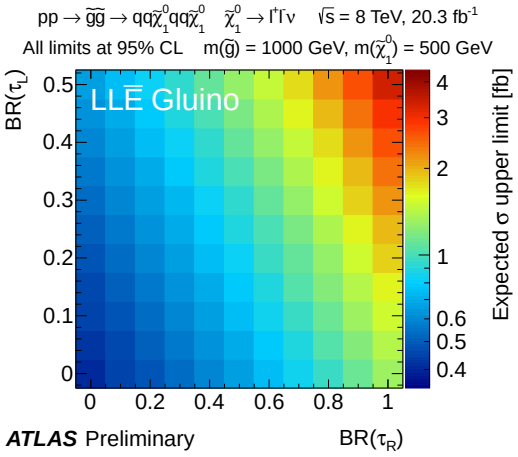

(b) Expected, $m(\tilde{g}) = 1000$ GeV, $m(\tilde{\chi}_1^0) = 500$ GeV

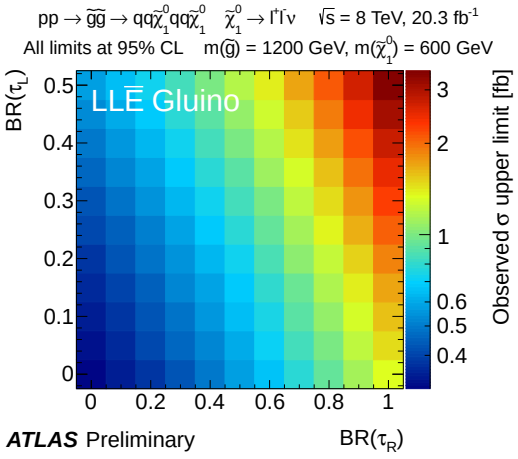

(c) Observed, $m(\tilde{g}) = 1200$ GeV, $m(\tilde{\chi}_1^0) = 600$ GeV

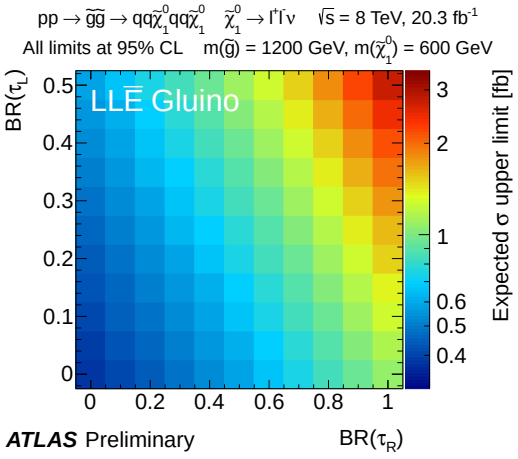

(d) Expected, $m(\tilde{g}) = 1200$ GeV, $m(\tilde{\chi}_1^0) = 600$ GeV

Figure 24: Observed and expected 95% CL upper cross-section limits for the $LL\bar{E}$ model points with $R = 0.5$ and $m(\tilde{g}) \leq 1200$ GeV. In all cases the constraints are taken from the SS/3L analysis.

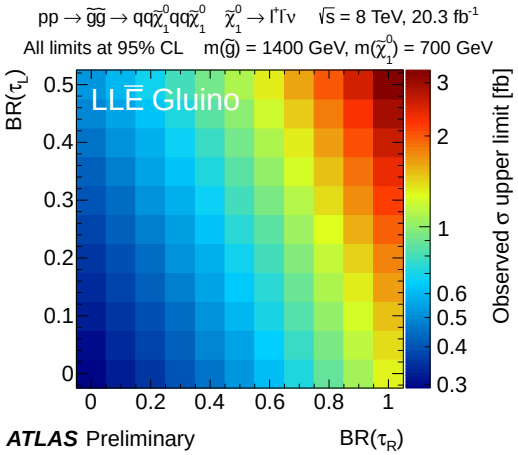

(a) Observed, $m(\tilde{g}) = 1400$ GeV, $m(\tilde{\chi}_1^0) = 700$ GeV

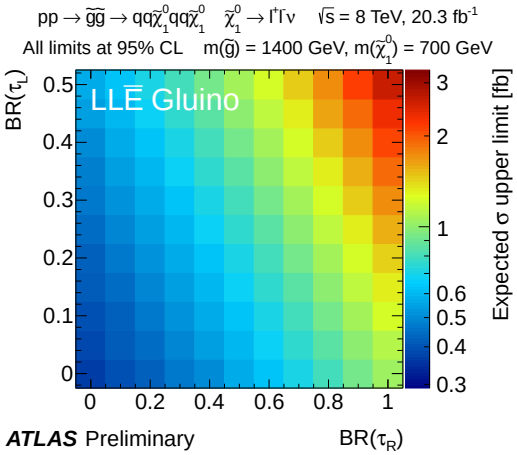

(b) Expected, $m(\tilde{g}) = 1400$ GeV, $m(\tilde{\chi}_1^0) = 700$ GeV

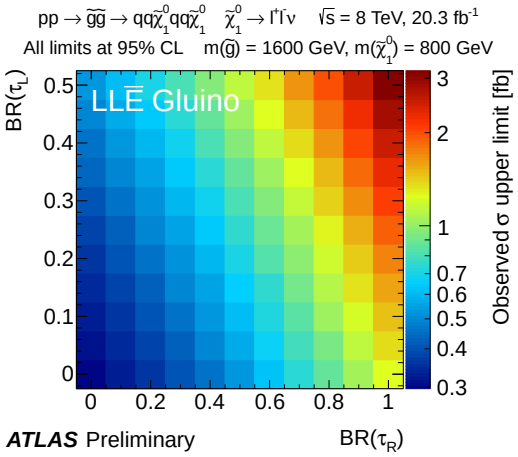

(c) Observed, $m(\tilde{g}) = 1600$ GeV, $m(\tilde{\chi}_1^0) = 800$ GeV

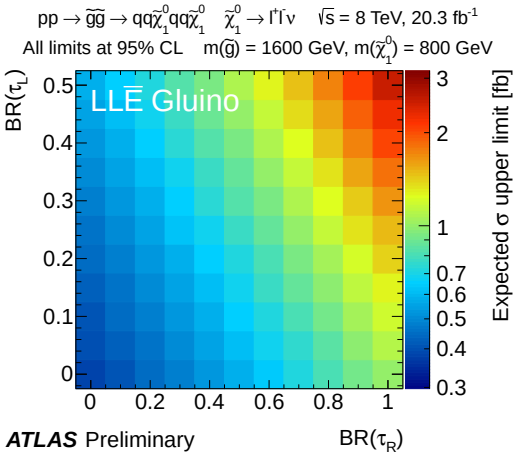

(d) Expected, $m(\tilde{g}) = 1600$ GeV, $m(\tilde{\chi}_1^0) = 800$ GeV

Figure 25: Observed and expected 95% CL upper cross-section limits for the $LL\bar{E}$ model points with $R = 0.5$ and $m(\tilde{g}) \geq 1400$ GeV. In all cases the constraints are taken from the SS/3L analysis.

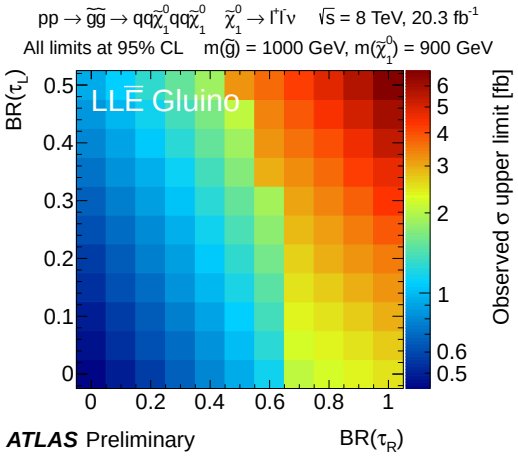

(a) Observed, $m(\tilde{g}) = 1000$ GeV, $m(\tilde{\chi}_1^0) = 900$ GeV

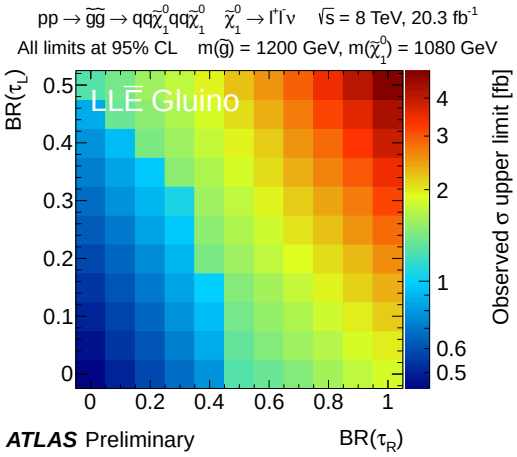

(b) Observed, $m(\tilde{g}) = 1200$ GeV, $m(\tilde{\chi}_1^0) = 1080$ GeV

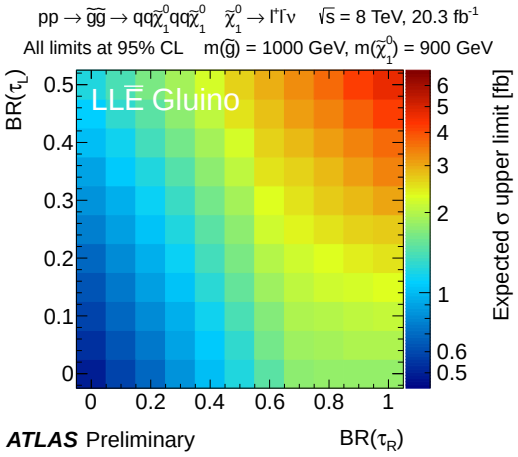

(c) Expected, $m(\tilde{g}) = 1000$ GeV, $m(\tilde{\chi}_1^0) = 900$ GeV

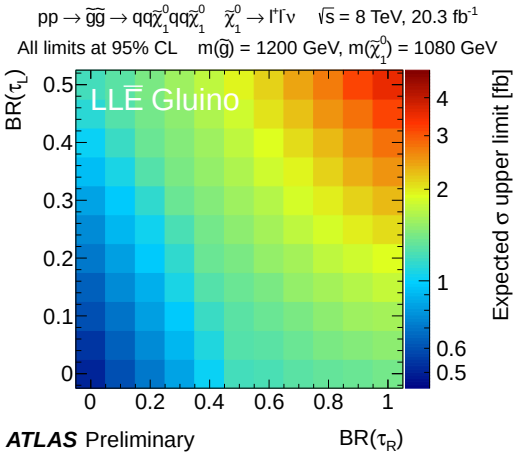

(d) Expected, $m(\tilde{g}) = 1200$ GeV, $m(\tilde{\chi}_1^0) = 1080$ GeV

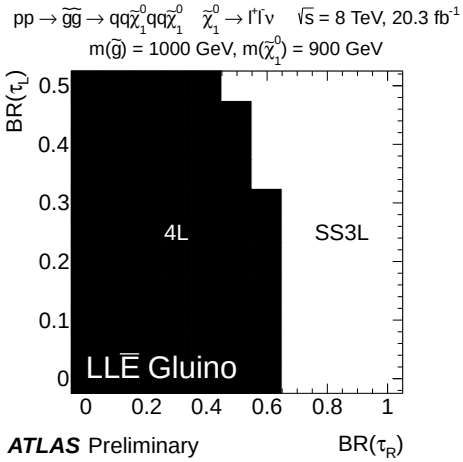

(e) Analysis, $m(\tilde{g}) = 1000$ GeV, $m(\tilde{\chi}_1^0) = 900$ GeV

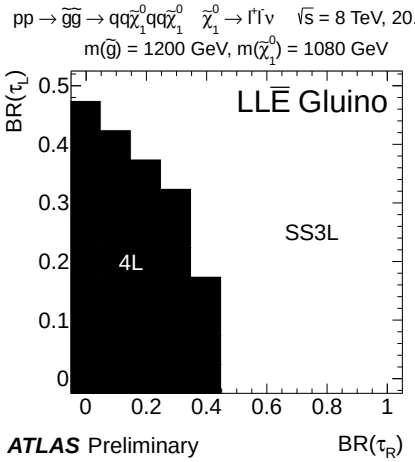

(f) Analysis, $m(\tilde{g}) = 1200$ GeV, $m(\tilde{\chi}_1^0) = 1080$ GeV

Figure 26: Observed and expected 95% CL upper cross-section limits and the best expected analysis for the $LL\bar{E}$ model points with $R = 0.9$ and $m(\tilde{g}) \leq 1200$ GeV.

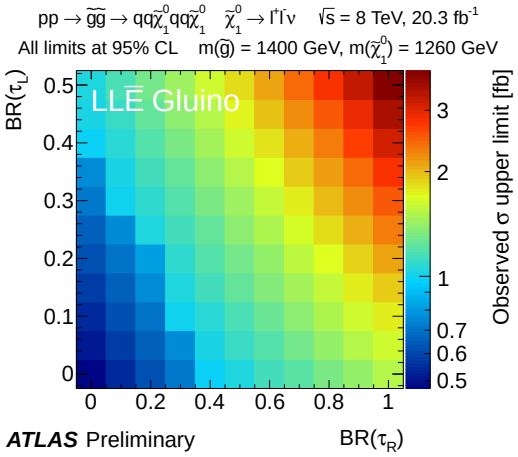

(a) Observed, $m(\tilde{g}) = 1400$ GeV, $m(\tilde{\chi}_1^0) = 1260$ GeV

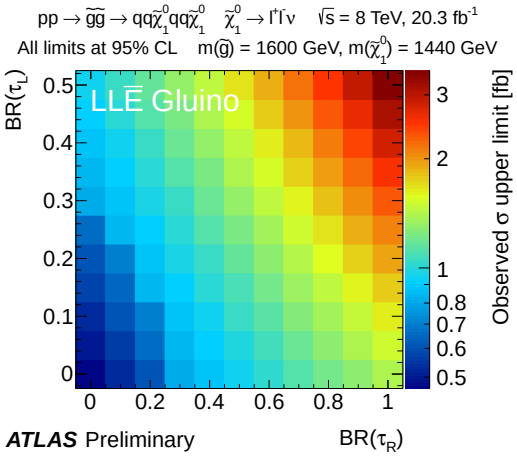

(b) Observed, $m(\tilde{g}) = 1600$ GeV, $m(\tilde{\chi}_1^0) = 1440$ GeV

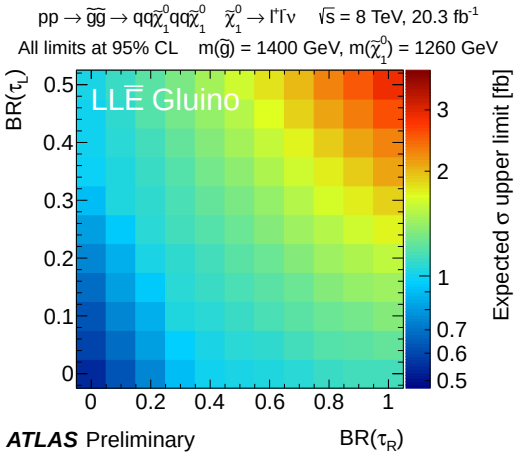

(c) Expected, $m(\tilde{g}) = 1400$ GeV, $m(\tilde{\chi}_1^0) = 1260$ GeV

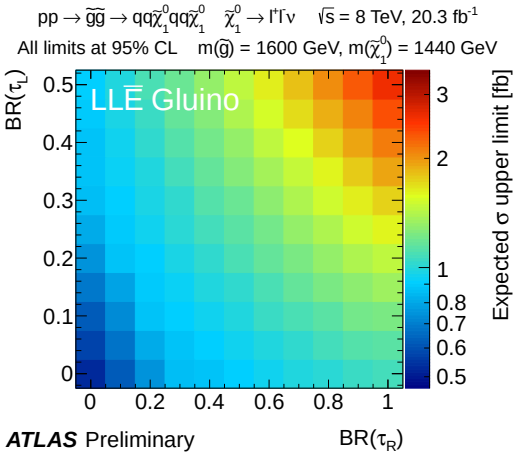

(d) Expected, $m(\tilde{g}) = 1600$ GeV, $m(\tilde{\chi}_1^0) = 1440$ GeV

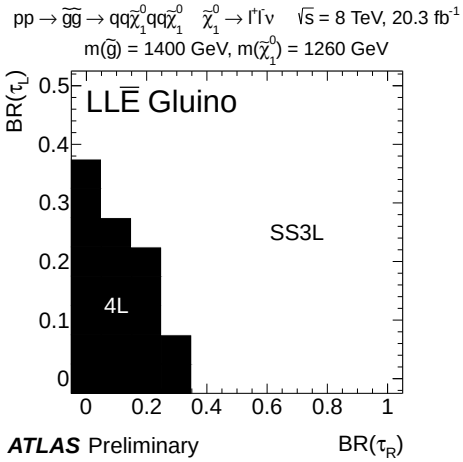

(e) Analysis, $m(\tilde{g}) = 1400$ GeV, $m(\tilde{\chi}_1^0) = 1260$ GeV

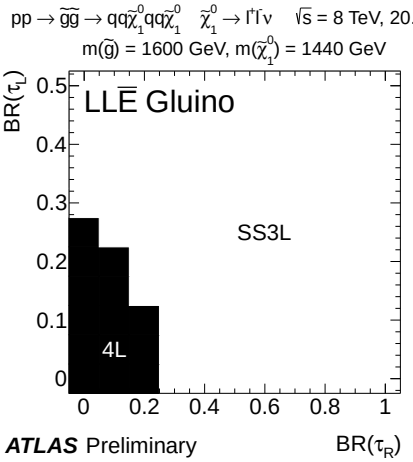

(f) Analysis, $m(\tilde{g}) = 1600$ GeV, $m(\tilde{\chi}_1^0) = 1440$ GeV

Figure 27: Observed and expected 95% CL upper cross-section limits and the best expected analysis for the $LL\bar{E}$ model points with $R = 0.9$ and $m(\tilde{g}) \geq 1400$ GeV.

B. Further results relating to the combined $LQ\bar{D}$ gluino model results

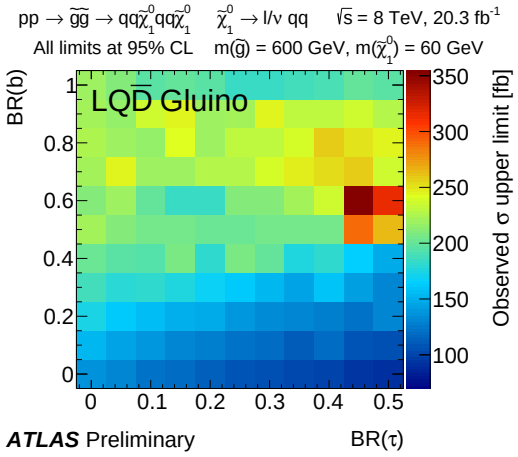

(a) Observed, $m(\tilde{g}) = 600$ GeV, $m(\tilde{\chi}_1^0) = 60$ GeV

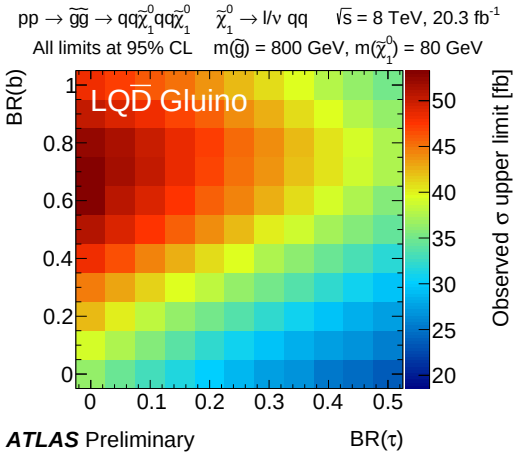

(b) Observed, $m(\tilde{g}) = 800$ GeV, $m(\tilde{\chi}_1^0) = 80$ GeV

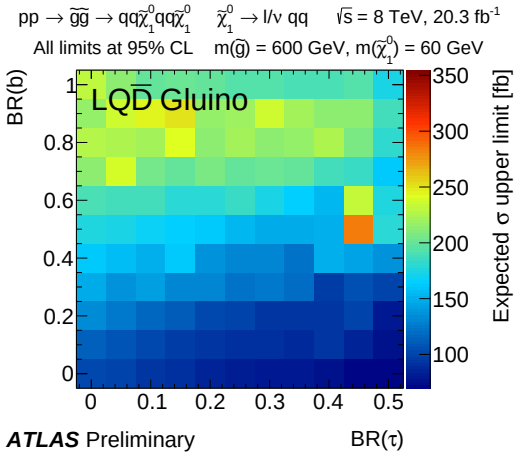

(c) Expected, $m(\tilde{g}) = 600$ GeV, $m(\tilde{\chi}_1^0) = 60$ GeV

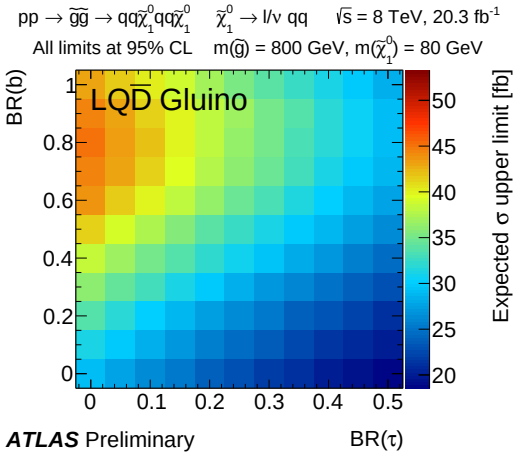

(d) Expected, $m(\tilde{g}) = 800$ GeV, $m(\tilde{\chi}_1^0) = 80$ GeV

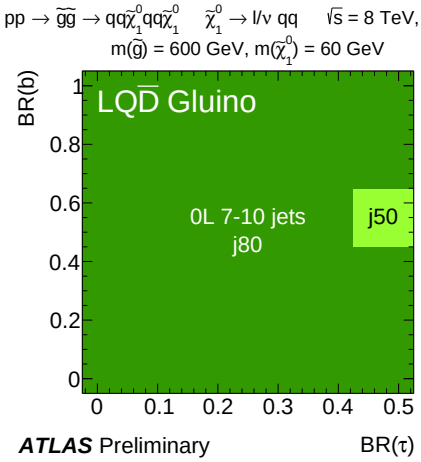

(e) Analysis, $m(\tilde{g}) = 600$ GeV, $m(\tilde{\chi}_1^0) = 60$ GeV

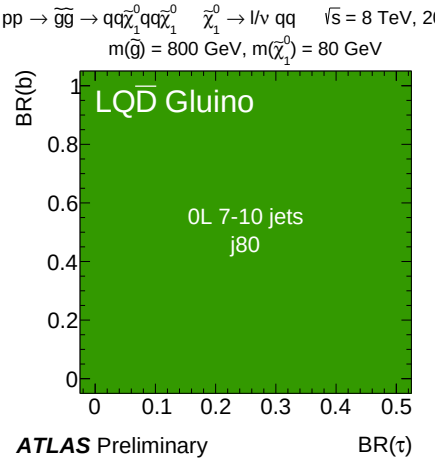

(f) Analysis, $m(\tilde{g}) = 800$ GeV, $m(\tilde{\chi}_1^0) = 80$ GeV

Figure 28: Observed and expected 95% CL upper cross-section limits and the best expected signal regions for the $LQ\bar{D}$ model points with gluino production, $R = 0.1$ and $m(\tilde{g}) \leq 800$ GeV. In (a), (c) and (e), conservative constraints from the $p_{\mathrm{T}} > 50$ GeV regions are quoted where reliable results for the $p_{\mathrm{T}} > 80$ GeV signal regions could not be obtained.

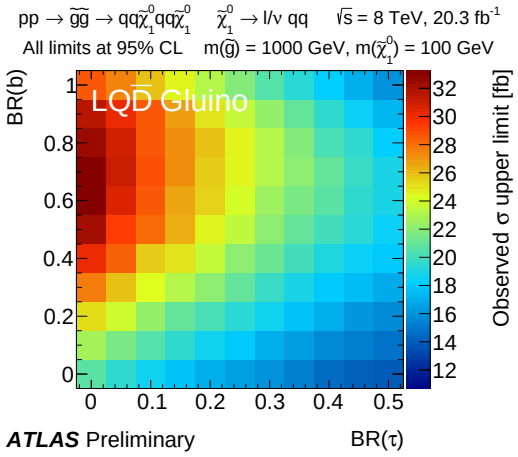

(a) Observed, $m(\tilde{g}) = 1000$ GeV, $m(\tilde{\chi}_1^0) = 100$ GeV

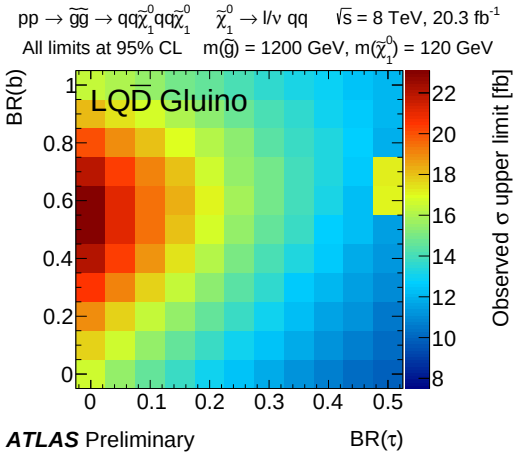

(b) Observed, $m(\tilde{g}) = 1200$ GeV, $m(\tilde{\chi}_1^0) = 120$ GeV

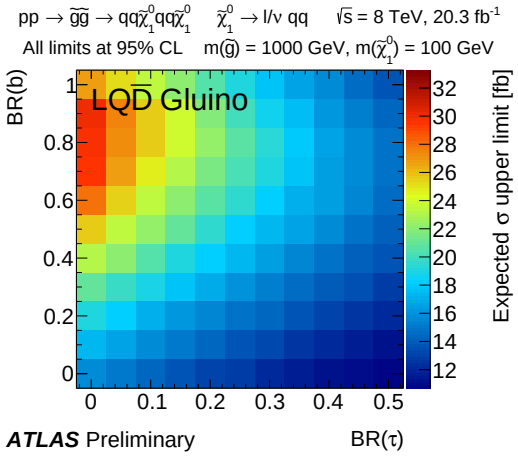

(c) Expected, $m(\tilde{g}) = 1000$ GeV, $m(\tilde{\chi}_1^0) = 100$ GeV

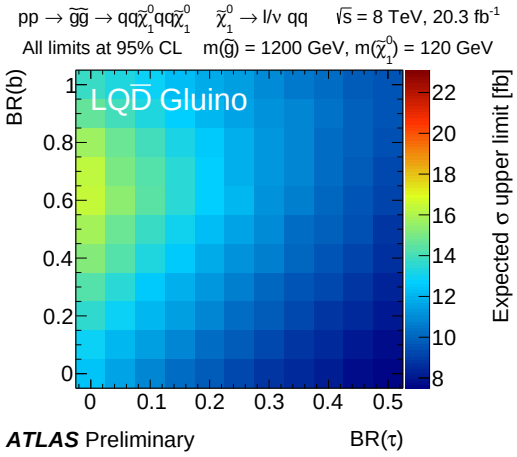

(d) Expected, $m(\tilde{g}) = 1200$ GeV, $m(\tilde{\chi}_1^0) = 120$ GeV

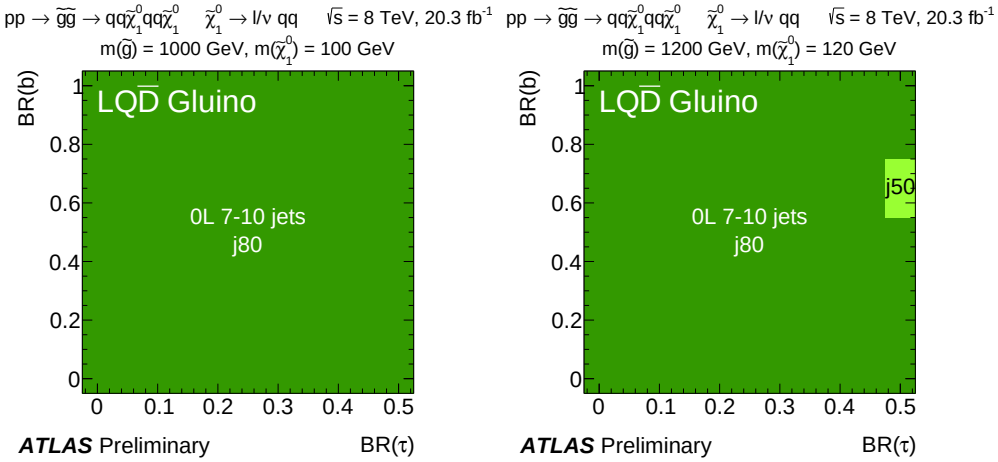

(e) Analysis, $m(\tilde{g}) = 1000$ GeV, $m(\tilde{\chi}_1^0) = 100$ GeV (f) Analysis, $m(\tilde{g}) = 1200$ GeV, $m(\tilde{\chi}_1^0) = 120$ GeV

Figure 29: Observed and expected 95% CL upper cross-section limits and the best expected signal regions for the $LQ\bar{D}$ model points with gluino production, $R = 0.1$ and $1000 \leq m(\tilde{g}) \leq 1200$ GeV.

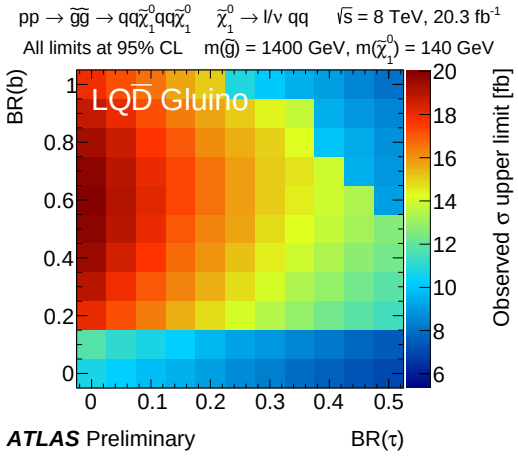

(a) Observed, $m(\tilde{g}) = 1400$ GeV, $m(\tilde{\chi}_1^0) = 140$ GeV

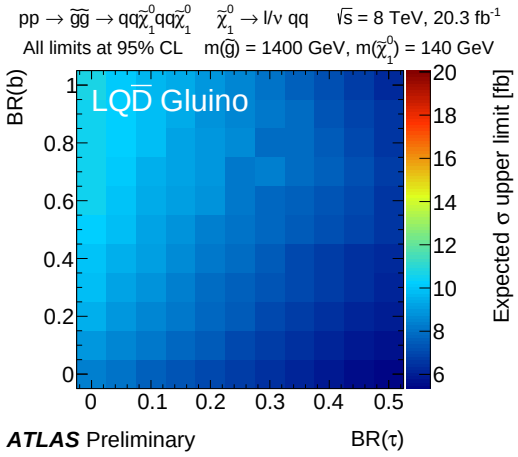

(b) Expected, $m(\tilde{g}) = 1400$ GeV, $m(\tilde{\chi}_1^0) = 140$ GeV

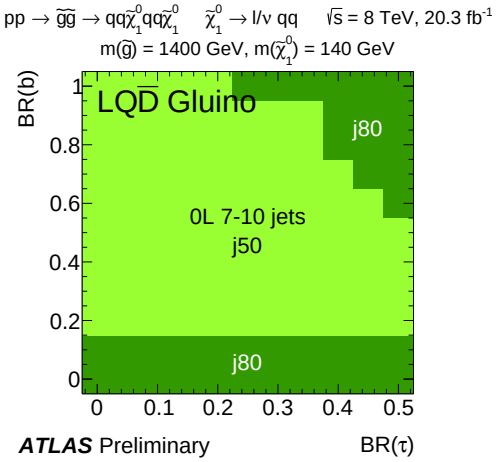

(c) Analysis, $m(\tilde{g}) = 1400$ GeV, $m(\tilde{\chi}_1^0) = 140$ GeV

Figure 30: Observed and expected 95% CL upper cross-section limits and the best expected signal regions for the $LQ\bar{D}$ model point with gluino production, $R = 0.1$ and $m(\tilde{g}) = 1400$ GeV.

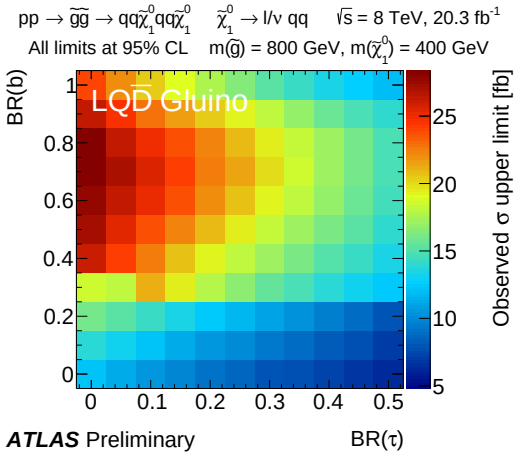

(a) Observed, $m(\tilde{g}) = 800$ GeV, $m(\tilde{\chi}_1^0) = 400$ GeV

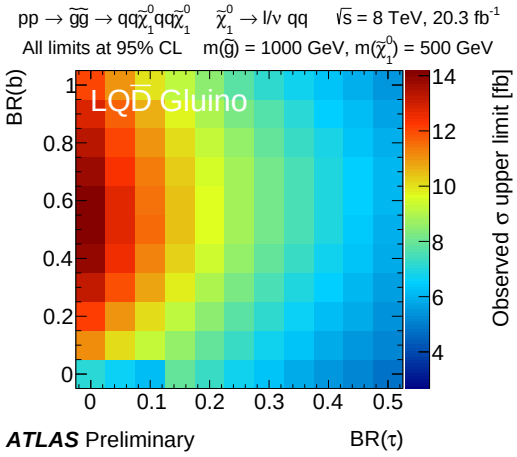

(b) Observed, $m(\tilde{g}) = 1000$ GeV, $m(\tilde{\chi}_1^0) = 500$ GeV

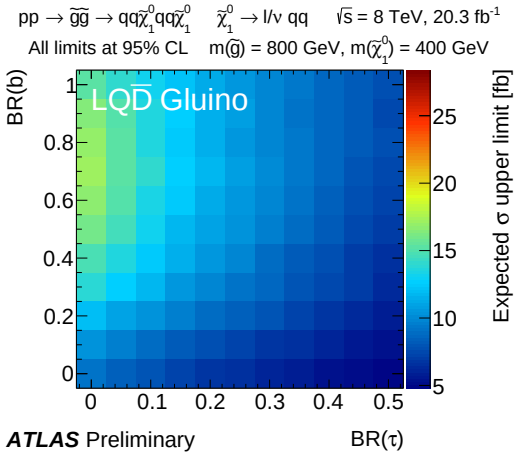

(c) Expected, $m(\tilde{g}) = 800$ GeV, $m(\tilde{\chi}_1^0) = 400$ GeV

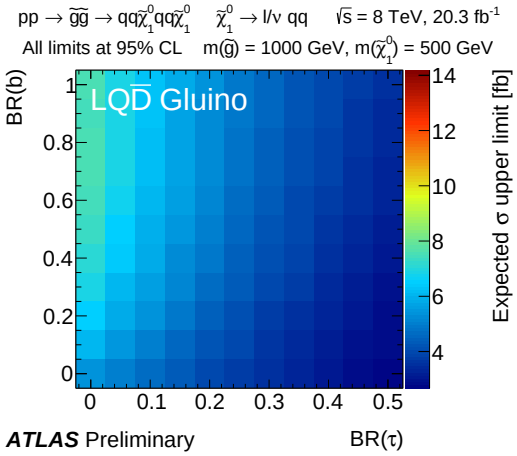

(d) Expected, $m(\tilde{g}) = 1000$ GeV, $m(\tilde{\chi}_1^0) = 500$ GeV

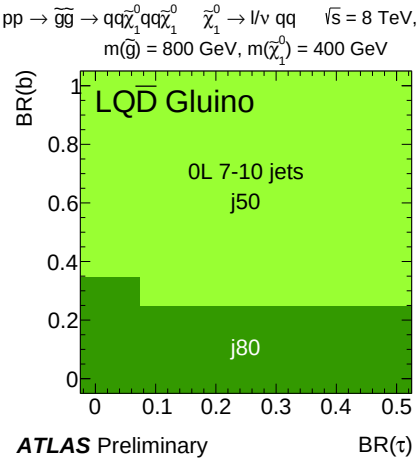

(e) Analysis, $m(\tilde{g}) = 800$ GeV, $m(\tilde{\chi}_1^0) = 400$ GeV

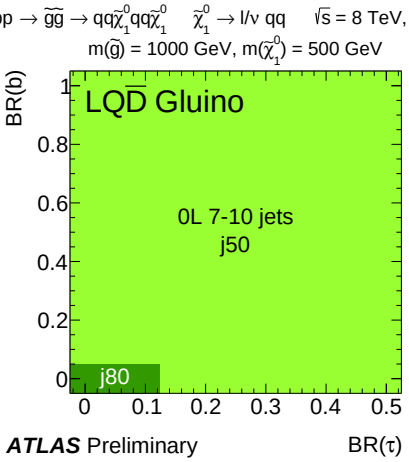

(f) Analysis, $m(\tilde{g}) = 1000$ GeV, $m(\tilde{\chi}_1^0) = 500$ GeV

Figure 31: Observed and expected 95% CL upper cross-section limits and the best expected signal regions for the $LQ\bar{D}$ model points with gluino production, $R = 0.5$ and $m(\tilde{g}) \leq 1000$ GeV.

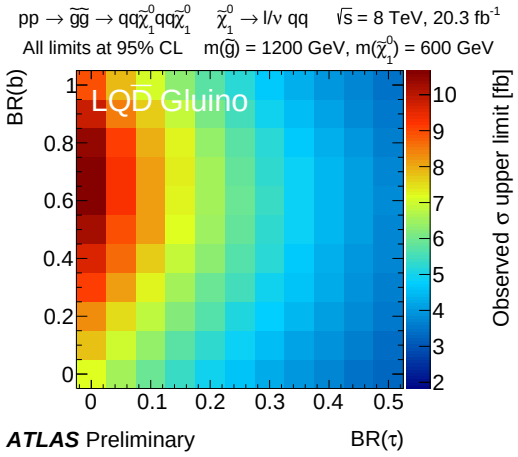

(a) Observed, $m(\tilde{g}) = 1200$ GeV, $m(\tilde{\chi}_1^0) = 600$ GeV

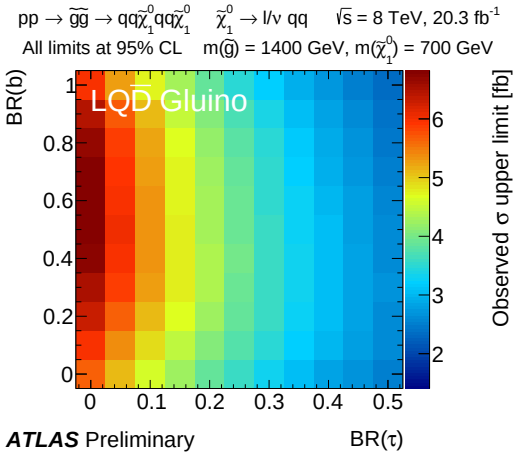

(b) Observed, $m(\tilde{g}) = 1400$ GeV, $m(\tilde{\chi}_1^0) = 700$ GeV

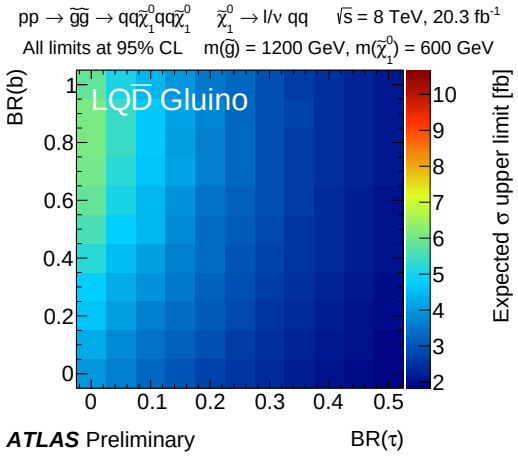

(c) Expected, $m(\tilde{g}) = 1200$ GeV, $m(\tilde{\chi}_1^0) = 600$ GeV

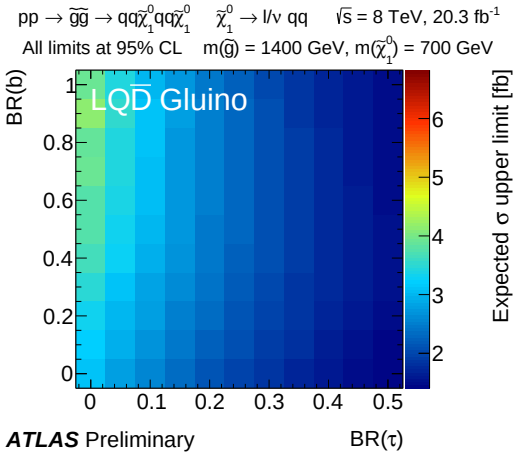

(d) Expected, $m(\tilde{g}) = 1400$ GeV, $m(\tilde{\chi}_1^0) = 700$ GeV

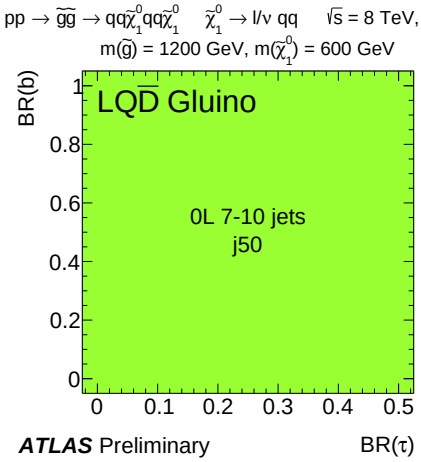

(e) Analysis, $m(\tilde{g}) = 1200$ GeV, $m(\tilde{\chi}_1^0) = 600$ GeV

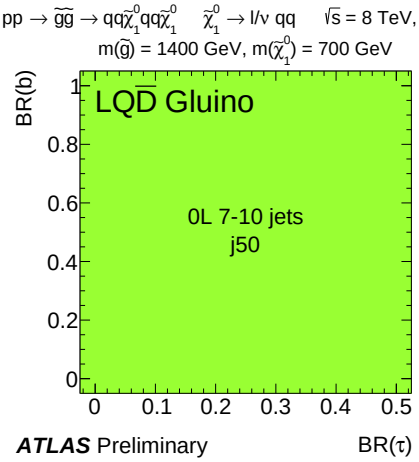

(f) Analysis, $m(\tilde{g}) = 1400$ GeV, $m(\tilde{\chi}_1^0) = 700$ GeV

Figure 32: Observed and expected 95% CL upper cross-section limits and the best expected signal regions for the $LQ\bar{D}$ model points with gluino production, $R = 0.5$ and $m(\tilde{g}) \geq 1200$ GeV.

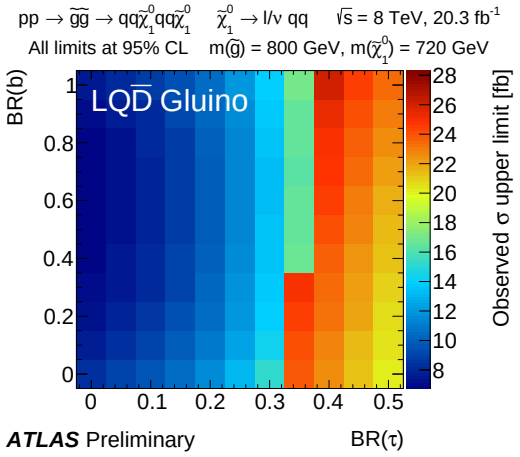

(a) Observed, $m(\tilde{g}) = 800$ GeV, $m(\tilde{\chi}_1^0) = 720$ GeV

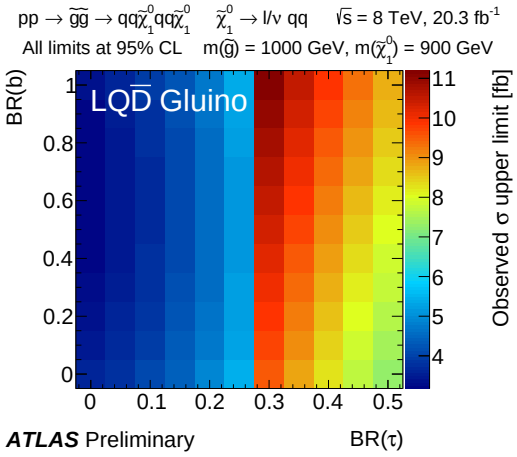

(b) Observed, $m(\tilde{g}) = 1000$ GeV, $m(\tilde{\chi}_1^0) = 900$ GeV

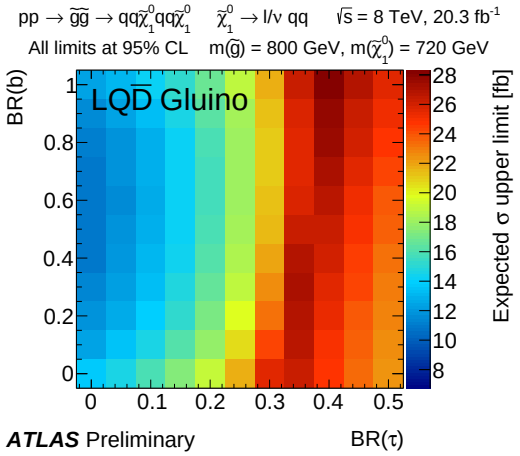

(c) Expected, $m(\tilde{g}) = 800$ GeV, $m(\tilde{\chi}_1^0) = 720$ GeV

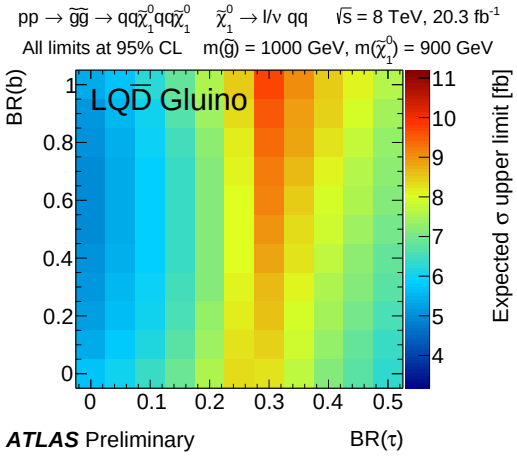

(d) Expected, $m(\tilde{g}) = 1000$ GeV, $m(\tilde{\chi}_1^0) = 900$ GeV

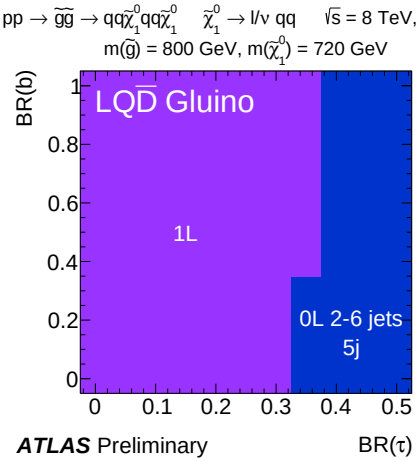

(e) Analysis, $m(\tilde{g}) = 800$ GeV, $m(\tilde{\chi}_1^0) = 720$ GeV

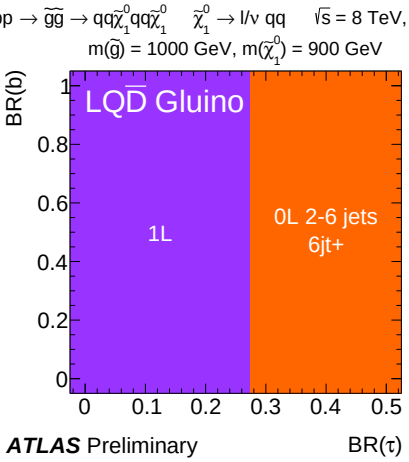

(f) Analysis, $m(\tilde{g}) = 1000$ GeV, $m(\tilde{\chi}_1^0) = 900$ GeV

Figure 33: Observed and expected 95% CL upper cross-section limits and the best expected signal regions for the $LQ\bar{D}$ model points with gluino production, $R = 0.9$ and $m(\tilde{g}) \leq 1000$ GeV.

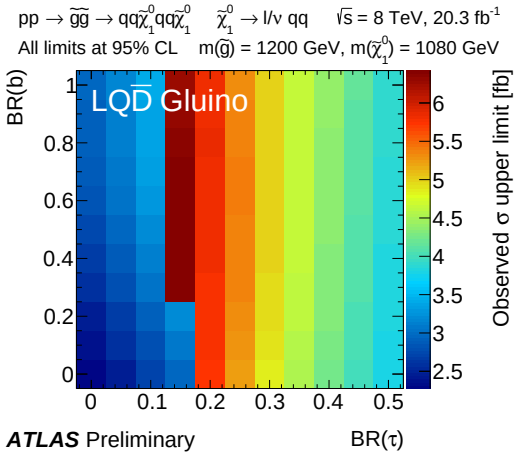

(a) Observed, $m(\tilde{g}) = 1200$ GeV, $m(\tilde{\chi}_1^0) = 1080$ GeV

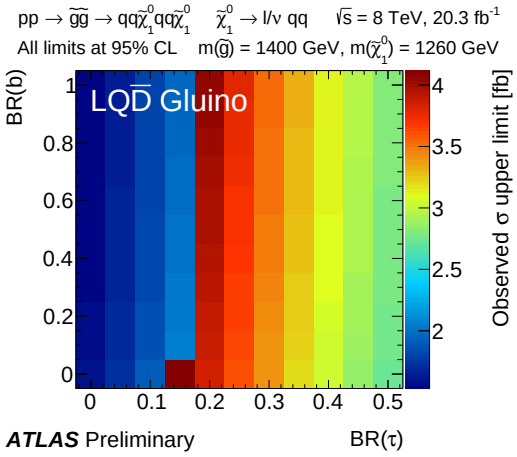

(b) Observed, $m(\tilde{g}) = 1400$ GeV, $m(\tilde{\chi}_1^0) = 1260$ GeV

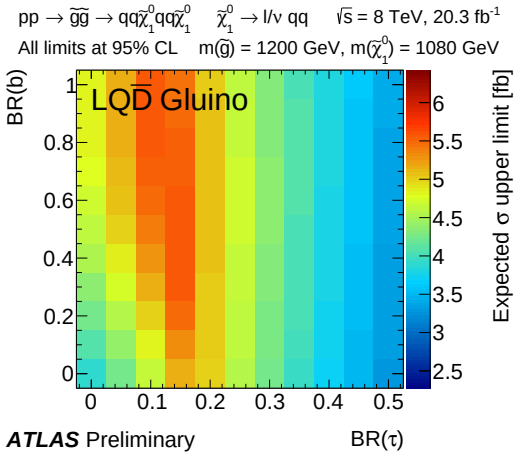

(c) Expected, $m(\tilde{g}) = 1200$ GeV, $m(\tilde{\chi}_1^0) = 1080$ GeV

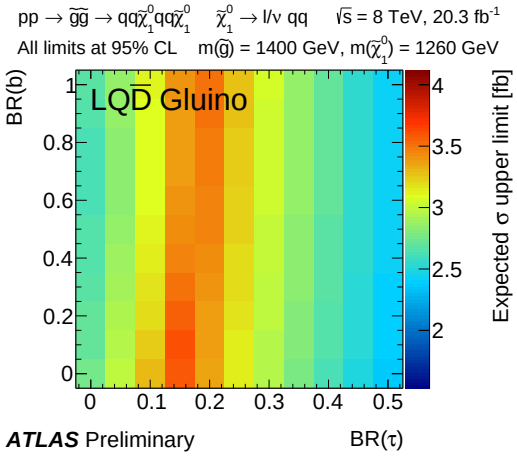

(d) Expected, $m(\tilde{g}) = 1400$ GeV, $m(\tilde{\chi}_1^0) = 1260$ GeV

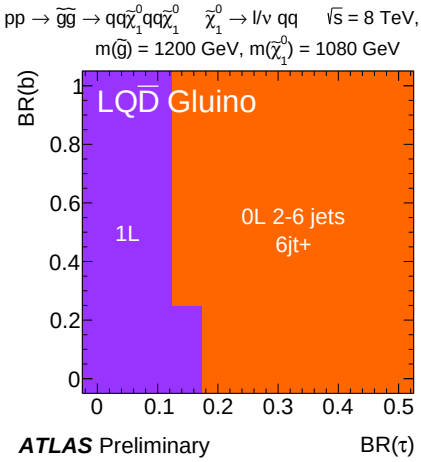

(e) Analysis, $m(\tilde{g}) = 1200$ GeV, $m(\tilde{\chi}_1^0) = 1080$ GeV

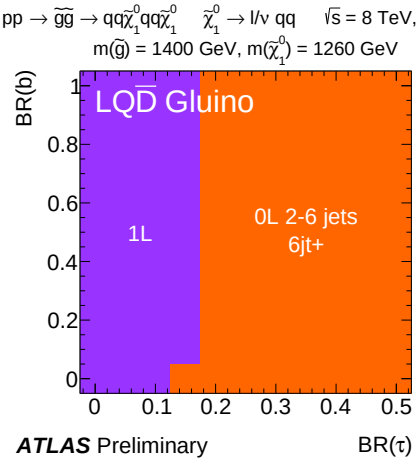

(f) Analysis, $m(\tilde{g}) = 1400$ GeV, $m(\tilde{\chi}_1^0) = 1260$ GeV

Figure 34: Observed and expected 95% CL upper cross-section limits and the best expected signal regions for the $LQ\bar{D}$ model points with gluino production, $R = 0.9$ and $m(\tilde{g}) \geq 1200$ GeV.

C. Further results relating to the combined $LQ\bar{D}$ squark model results

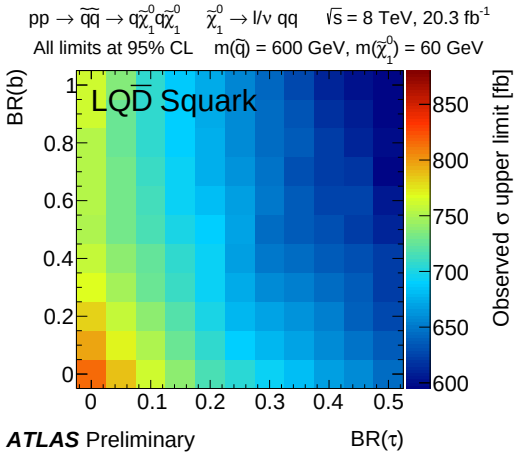

(a) Observed, $m(\tilde{q}) = 600$ GeV, $m(\tilde{\chi}_1^0) = 60$ GeV

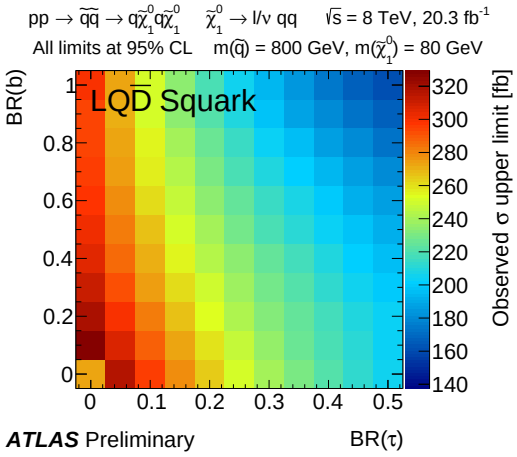

(b) Observed, $m(\tilde{q}) = 800$ GeV, $m(\tilde{\chi}_1^0) = 80$ GeV

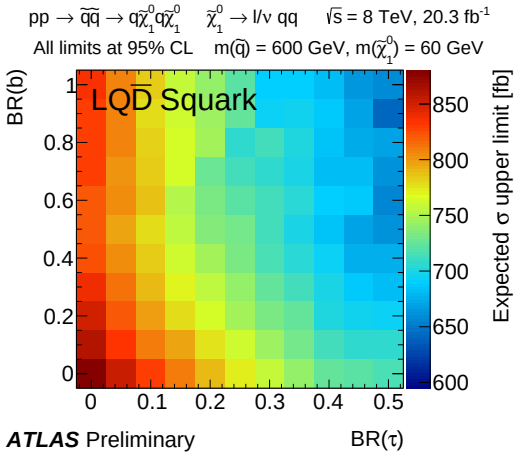

(c) Expected, $m(\tilde{q}) = 600$ GeV, $m(\tilde{\chi}_1^0) = 60$ GeV

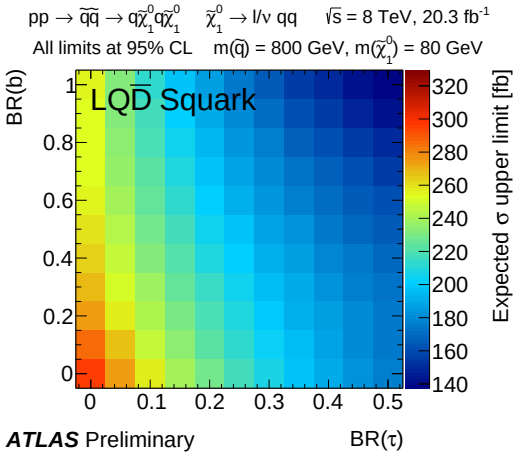

(d) Expected, $m(\tilde{q}) = 800$ GeV, $m(\tilde{\chi}_1^0) = 80$ GeV

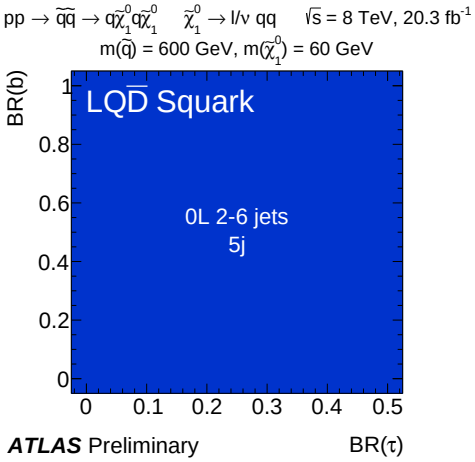

(e) Analysis, $m(\tilde{q}) = 600$ GeV, $m(\tilde{\chi}_1^0) = 60$ GeV

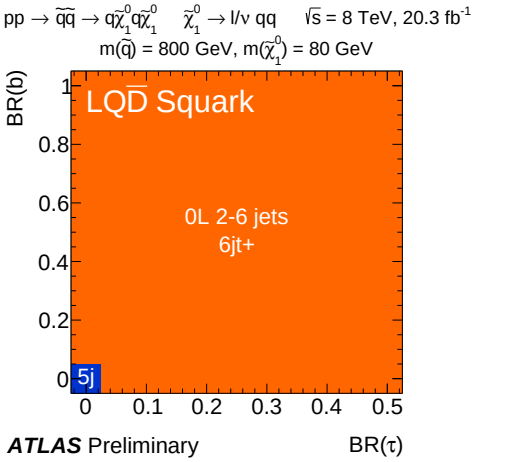

(f) Analysis, $m(\tilde{q}) = 800$ GeV, $m(\tilde{\chi}_1^0) = 80$ GeV

Figure 35: Observed and expected 95% CL upper cross-section limits and the best expected signal regions for the $LQ\bar{D}$ model points with squark production, $R = 0.1$ and $m(\tilde{q}) \leq 800$ GeV. The 1L search is not considered for these squark masses, as described in Sect. 3.3.

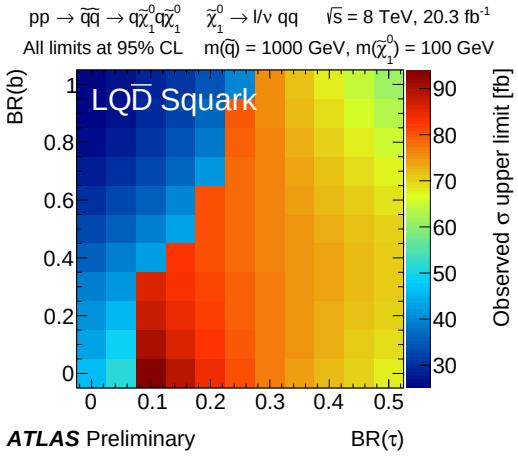

(a) Observed, $m(\tilde{q}) = 1000$ GeV, $m(\tilde{\chi}_1^0) = 100$ GeV

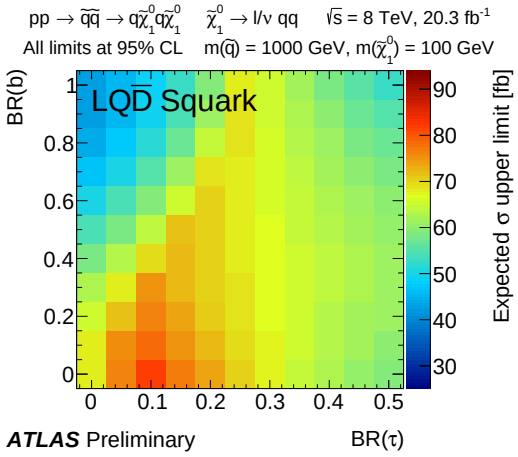

(b) Expected, $m(\tilde{q}) = 1000$ GeV, $m(\tilde{\chi}_1^0) = 100$ GeV

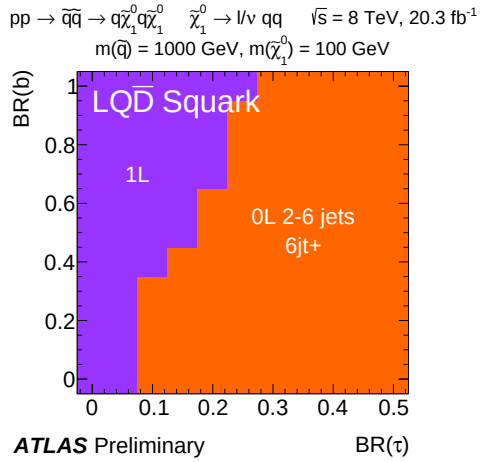

(c) Analysis, $m(\tilde{q}) = 1000$ GeV, $m(\tilde{\chi}_1^0) = 100$ GeV

Figure 36: Observed and expected 95% CL upper cross-section limits and the best expected signal regions for the $LQ\bar{D}$ model points with squark production, $R = 0.1$ and $m(\tilde{q}) = 1000$ GeV.

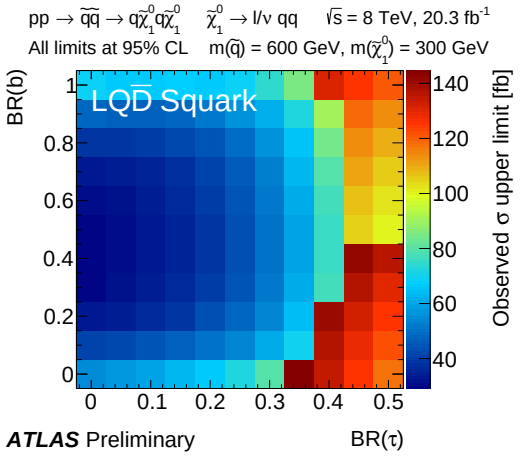

(a) Observed, $m(\tilde{q}) = 600$ GeV, $m(\tilde{\chi}_1^0) = 300$ GeV

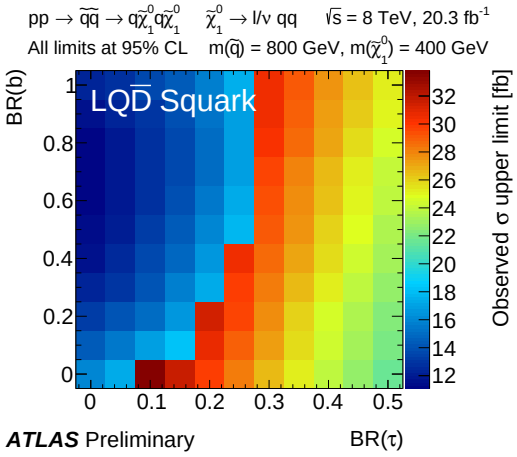

(b) Observed, $m(\tilde{q}) = 800$ GeV, $m(\tilde{\chi}_1^0) = 400$ GeV

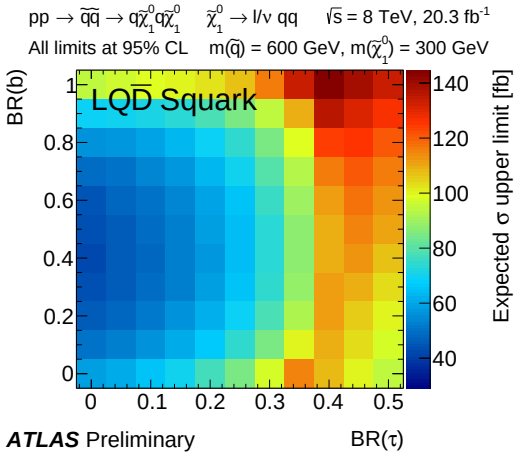

(c) Expected, $m(\tilde{q}) = 600$ GeV, $m(\tilde{\chi}_1^0) = 300$ GeV

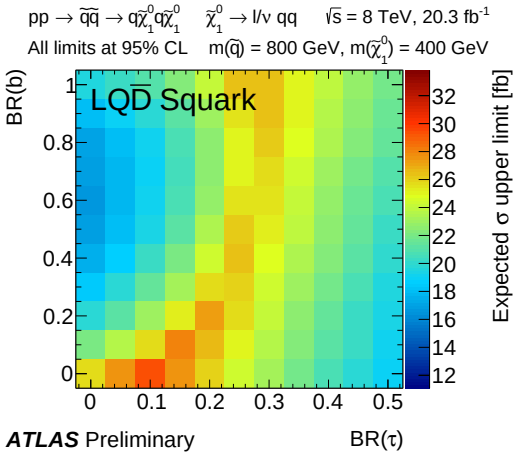

(d) Expected, $m(\tilde{q}) = 800$ GeV, $m(\tilde{\chi}_1^0) = 400$ GeV

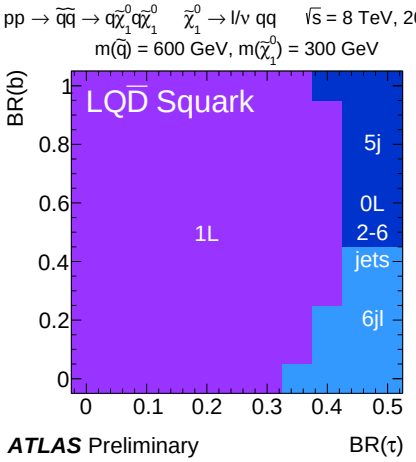

(e) Analysis, $m(\tilde{q}) = 600$ GeV, $m(\tilde{\chi}_1^0) = 300$ GeV

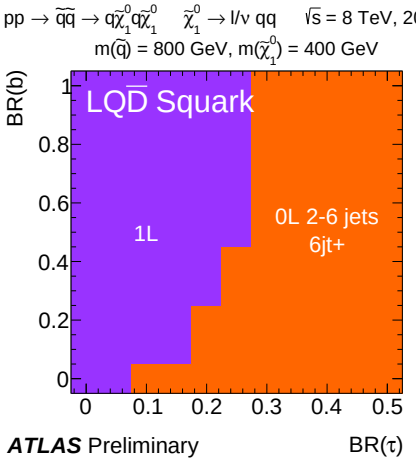

(f) Analysis, $m(\tilde{q}) = 800$ GeV, $m(\tilde{\chi}_1^0) = 400$ GeV

Figure 37: Observed and expected 95% CL upper cross-section limits and the best expected signal regions for the $LQ\bar{D}$ model points with squark production, $R = 0.5$ and $m(\tilde{q}) \leq 800$ GeV.

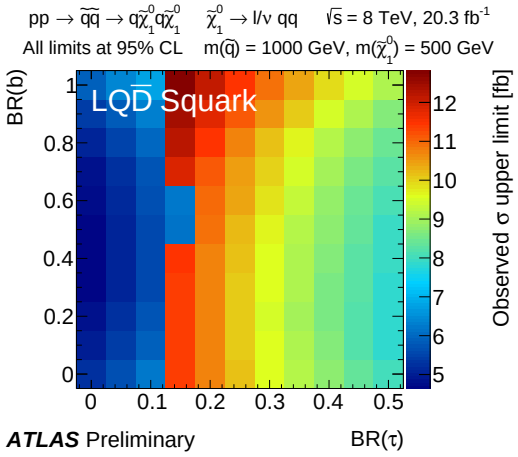

(a) Observed, $m(\tilde{q}) = 1000$ GeV, $m(\tilde{\chi}_1^0) = 500$ GeV

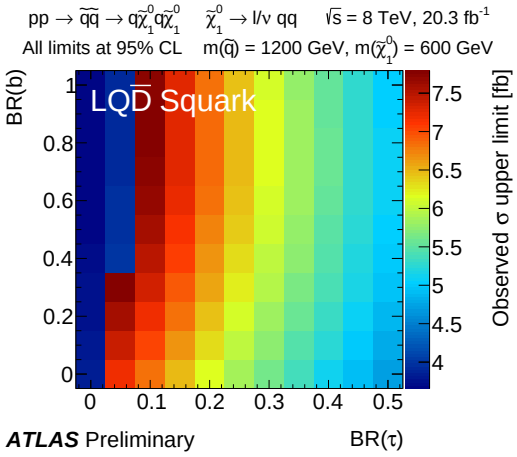

(b) Observed, $m(\tilde{q}) = 1200$ GeV, $m(\tilde{\chi}_1^0) = 600$ GeV

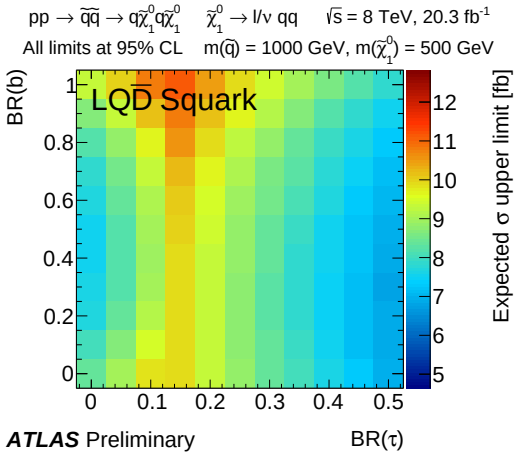

(c) Expected, $m(\tilde{q}) = 1000$ GeV, $m(\tilde{\chi}_1^0) = 500$ GeV

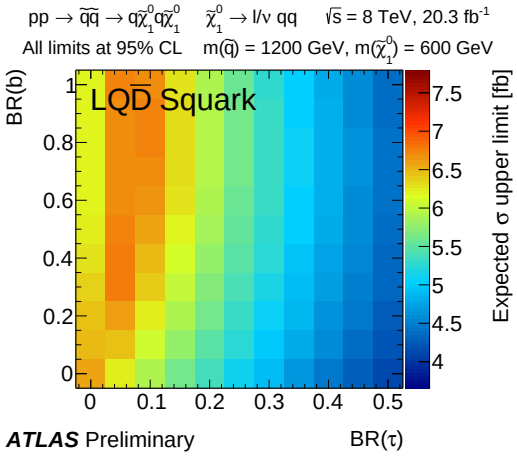

(d) Expected, $m(\tilde{q}) = 1200$ GeV, $m(\tilde{\chi}_1^0) = 600$ GeV

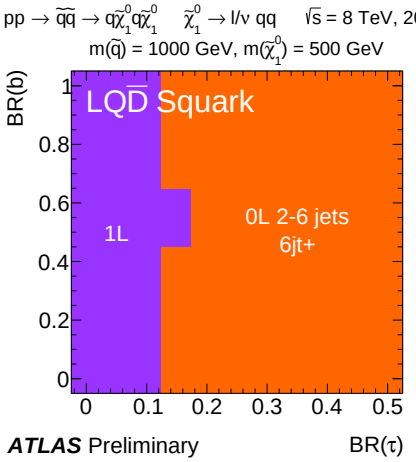

(e) Analysis, $m(\tilde{q}) = 1000$ GeV, $m(\tilde{\chi}_1^0) = 500$ GeV

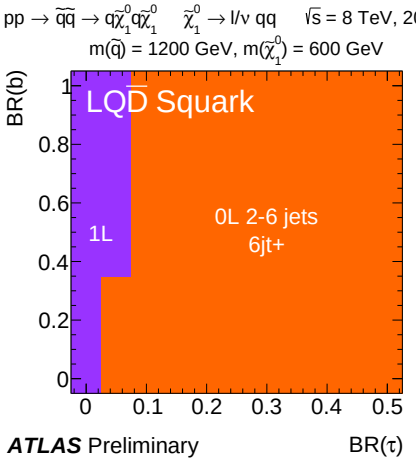

(f) Analysis, $m(\tilde{q}) = 1200$ GeV, $m(\tilde{\chi}_1^0) = 600$ GeV

Figure 38: Observed and expected 95% CL upper cross-section limits and the best expected signal regions for the $LQ\bar{D}$ model points with squark production, $R = 0.5$ and $m(\tilde{q}) \geq 1000$ GeV.

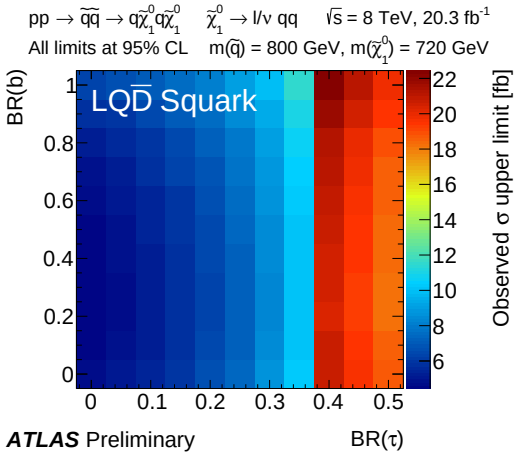

(a) Observed, $m(\tilde{q}) = 800$ GeV, $m(\tilde{\chi}_1^0) = 720$ GeV

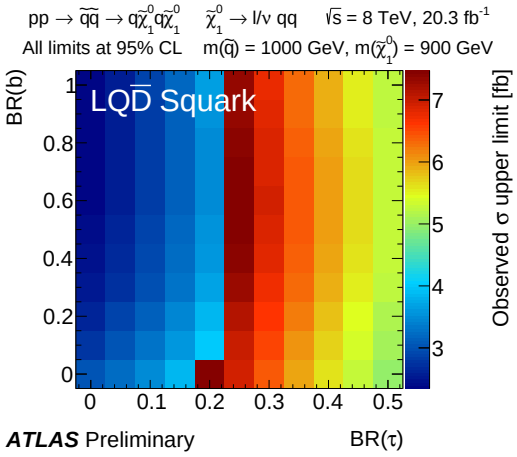

(b) Observed, $m(\tilde{q}) = 1000$ GeV, $m(\tilde{\chi}_1^0) = 900$ GeV

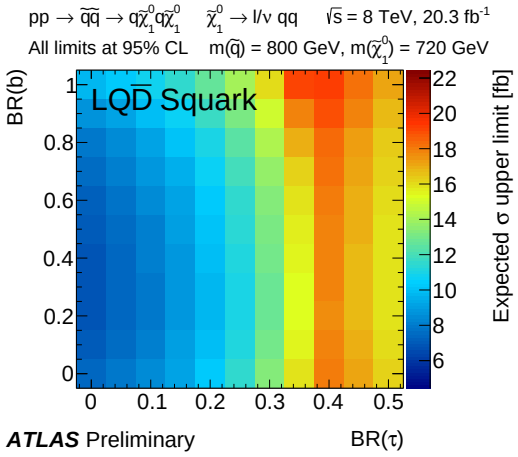

(c) Expected, $m(\tilde{q}) = 800$ GeV, $m(\tilde{\chi}_1^0) = 720$ GeV

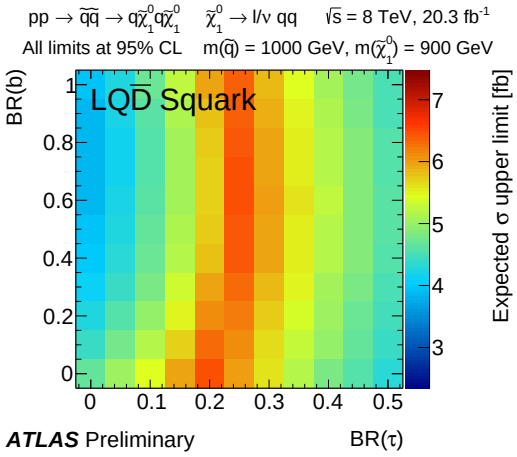

(d) Expected, $m(\tilde{q}) = 1000$ GeV, $m(\tilde{\chi}_1^0) = 900$ GeV

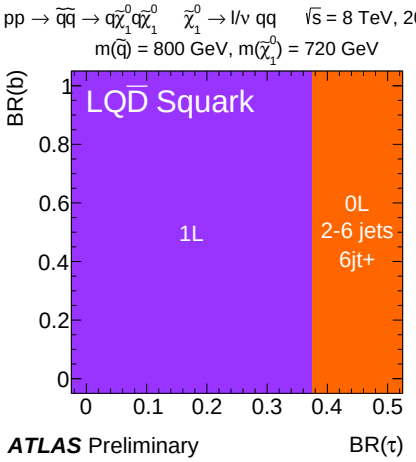

(e) Analysis, $m(\tilde{q}) = 800$ GeV, $m(\tilde{\chi}_1^0) = 720$ GeV

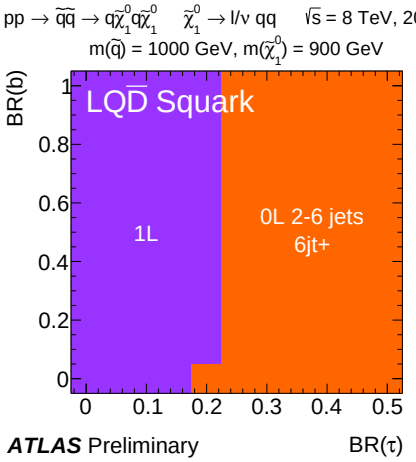

(f) Analysis, $m(\tilde{q}) = 1000$ GeV, $m(\tilde{\chi}_1^0) = 900$ GeV

Figure 39: Observed and expected 95% CL upper cross-section limits and the best expected signal regions for the $LQ\bar{D}$ model points with squark production, $R = 0.9$ and $m(\tilde{q}) \leq 1000$ GeV.

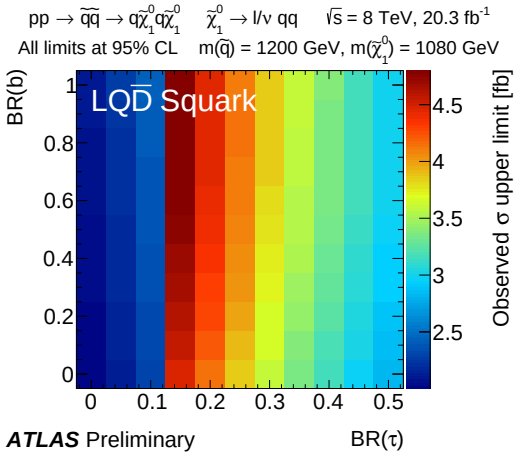

(a) Observed, $m(\tilde{q}) = 1200$ GeV, $m(\tilde{\chi}_1^0) = 1080$ GeV

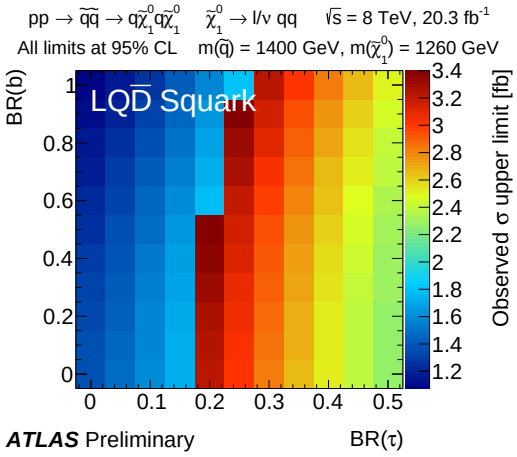

(b) Observed, $m(\tilde{q}) = 1400$ GeV, $m(\tilde{\chi}_1^0) = 1260$ GeV

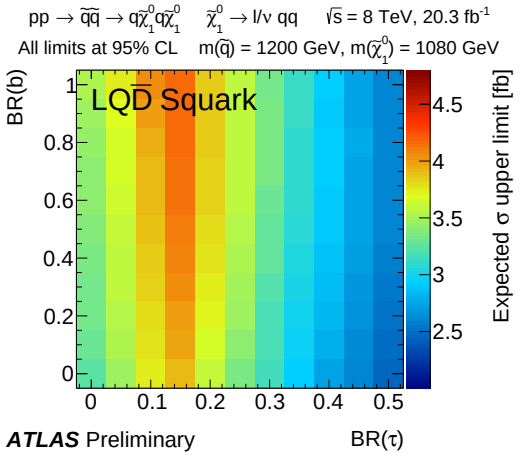

(c) Expected, $m(\tilde{q}) = 1200$ GeV, $m(\tilde{\chi}_1^0) = 1080$ GeV

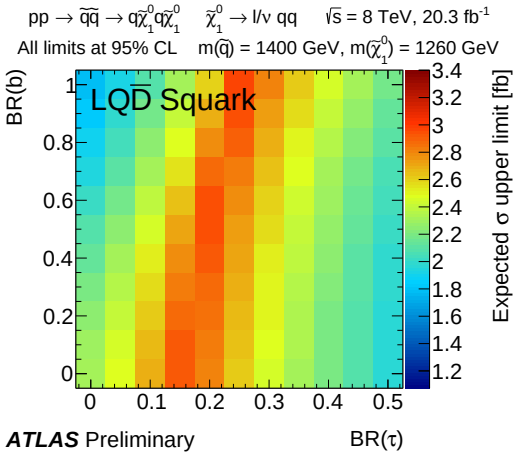

(d) Expected, $m(\tilde{q}) = 1400$ GeV, $m(\tilde{\chi}_1^0) = 1260$ GeV

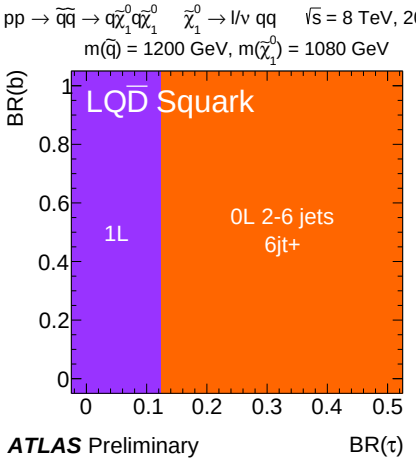

(e) Analysis, $m(\tilde{q}) = 1200$ GeV, $m(\tilde{\chi}_1^0) = 1080$ GeV

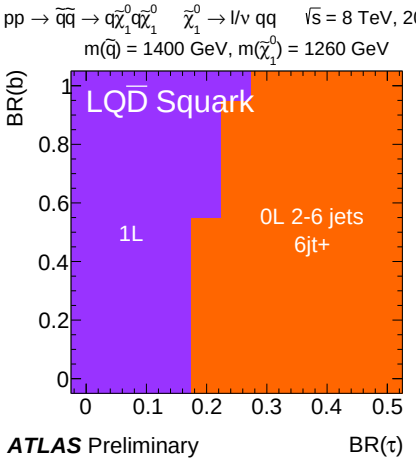

(f) Analysis, $m(\tilde{q}) = 1400$ GeV, $m(\tilde{\chi}_1^0) = 1260$ GeV

Figure 40: Observed and expected 95% CL upper cross-section limits and the best expected signal regions for the $LQ\bar{D}$ model points with squark production, $R = 0.9$ and $m(\tilde{q}) \geq 1200$ GeV.

D. Further results relating to the *b*RPV model results

μ	$m_{\tilde{q}_{\mathrm{L},3}}$	$m(\tilde{\chi}_1^0)$	$m(\tilde{\chi}_1^\pm)$	$m(\tilde{t}_1)$	σ_{3rd} [pb]	σ_{EWK} [pb]
160	350	156	160	355	1.304	1.036
160	650	154	158	534	0.073	1.094
160	950	154	158	533	0.057	1.095
210	950	207	210	535	0.056	0.347
310	450	311	313	415	0.447	0.063
310	650	311	313	541	0.067	0.063
310	950	311	313	539	0.052	0.063
460	650	464	465	540	0.067	0.009
460	800	464	465	582	0.034	0.009
460	850	464	465	579	0.034	0.009
460	950	464	465	545	0.049	0.009
510	850	515	516	580	0.034	0.005
510	900	515	516	567	0.038	0.005
510	950	515	516	549	0.046	0.005
560	800	565	566	584	0.034	0.003
560	850	565	566	580	0.034	0.003

Table 8: Overview of *b*RPV signal points with input parameters μ and $m_{\tilde{q}_{\mathrm{L},3}}$. These parameters and all sparticle masses are quoted in GeV. Cross-sections corresponding to production of lightest stop or sbottom pairs σ_{3rd} and electroweak production σ_{EWK} are also displayed.

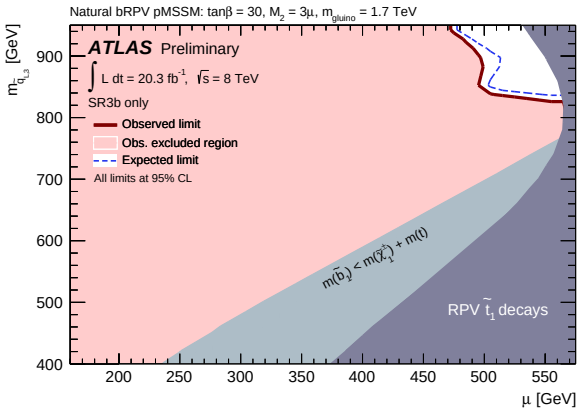

(a) Limit in SR3b.

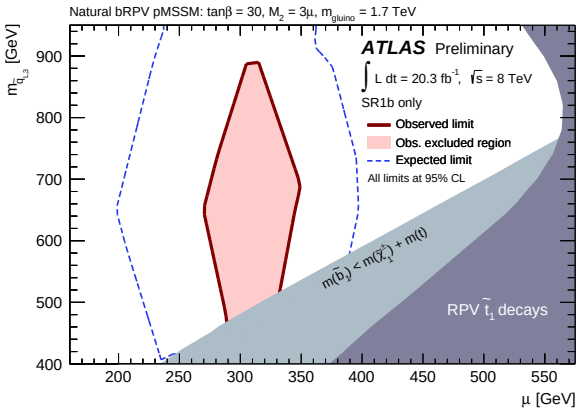

(b) Limit in SR1b.

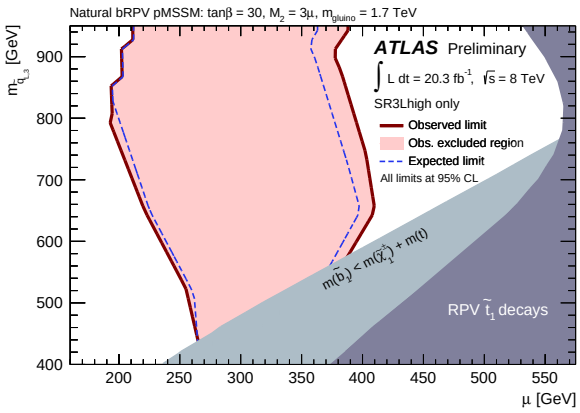

(c) Limit in SR3Lhigh.

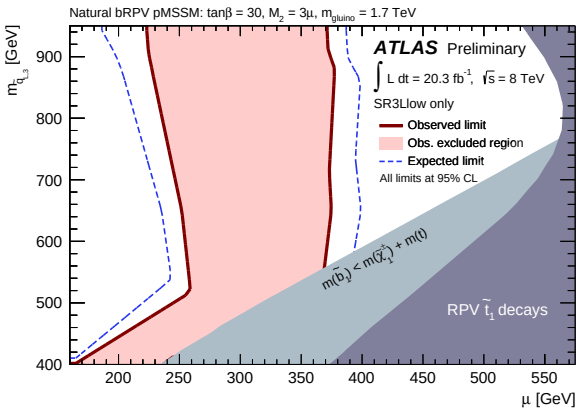

(d) Limit in SR3Llow.

Figure 41: Observed (solid) and expected (dashed) 95% CL exclusion limit contours for the natural *b*RPV model, obtained using individual signal regions of the SS/3L analysis [40].